Layer Stripping the Response from Sedimentary Basins in Teleseismic Data Using Transfer Functions

by

Reid Charles Campbell

A thesis submitted to the Faculty of Graduate Studies of

The University of Manitoba

in partial fulfilment of the requirements of the degree of

MASTER OF SCIENCE

Department of Geological Sciences

University of Manitoba

Winnipeg

Abstract

Receiver functions generated from distant earthquakes have long been used to determine deep crustal and mantle structure beneath seismic stations. Teleseismic research over sedimentary basins often has to contend with cluttering of the seismic response by basin reverberations. A sedimentary basin typically exhibits a sharp velocity contrast at their base, which acts as a strong reflector for downgoing seismic waves, leading to reverberations within the basin between the basement interface and free-surface. These reverberations obscure important P to S converted arrivals and Moho reverberations in receiver functions. This research tests whether it is possible to remove the effects caused by a sedimentary basin (layer-strip) using imperfect velocity models. A filter is generated using the propagator method, as the spectral ratio of two model responses: one containing the basin and one without. The transfer function, generated as the ratio between the two responses, acts as an acausal filter. Tests on synthetic data were used to evaluate the level of model accuracy required for effective filtering. The method was then tested on real data from Canadian National Seismograph Network station EDM (Edmonton, Alberta, in the Western Canada Sedimentary basin) as well as a line of EarthScope Transportable Array stations over the Williston Basin. Results indicate that the effectiveness of the filter is correlated with the quality of the model, and that the method significantly improves the recovery of Moho reverberations (and thus the quality of an H-k stack) on real teleseismic data collected over sedimentary basins. As a quality basin model is required to achieve trustworthy filtering, the layer-strip methodology is particularly useful in areas where a velocity model is produced with two or more lines of evidence.

Acknowledgements

Thank you to my advisor Dr. Andrew Frederiksen for sparking my love for geophysics and seismology in an intro to geophysics course, and for continuing to teach me through my undergraduate and graduate career. Thank you for giving me the opportunity to continue into graduate school and for providing me with a truly fascinating research topic. All of the support and patience you have shown has not gone unnoticed.

I would also like to thank Dr. Ian Ferguson for his excellent instruction and guidance through both my undergrad and graduate degrees. I have enjoyed my geophysics courses and projects beyond all others. Thank you to Mulu Serzu for your instruction and help. I would also like to thank Dr. Kristopher Innanen for agreeing to be my external examiner.

Funding for this project was provided by Canadians, through NSERC and the Federal Government of Canada.

Thank you to my family who supported me throughout this process. Thank you to my friends, especially to CKT and those in geophysics who pushed me to excel in my undergrad with somewhat healthy competition.

Finally, thank you to my wife Mandy who has pushed me onwards towards completing this research and who has agreed to read the entirety of my thesis.

Table of Contents

List of Tables

List of Figures

Chapter 1. Introduction

1.1 Overview

Strong earthquakes generate seismic waves that travel through the earth's crust, mantle and core. These seismic waves act as an invaluable source of data to study the earth's structure. Earthquakes are considered teleseismic when recorded at seismic stations sourced from a great distance from the source and the main body-wave phases arrive nearly vertically. Receiver functions generated from three-component teleseismic data have long been used to determine deep crustal and mantle structure beneath seismic stations (Langston, 1979; Owens *et al.*, 1984; Ammon, 1991; Zandt and Ammon, 1995; Zhu and Kanamori, 2000; Yu *et al*., 2015).

During teleseismic research, it is often necessary to use data collected at seismic stations above seismically slow sedimentary layers or basins. A slow sedimentary basin is any sedimentary basin with a significantly lower P wave velocity than the underlying basement. This situation produces a strong impedance contrast between the basin and basement. Analyzing receiver functions generated from data collected over these sedimentary basins can be challenging, as the seismic energy often reverberates inside the basin (Boore *et al.,* 1971; Julià *et. al.,* 2008; Yu *et al*., 2015). The basin reverberations or basin multiples often obscure important phase arrivals in the receiver function, such as the Ps conversion from the Moho, or the Moho multiple PpPs (Cassidy, 1992; Juliá *et al.,* 2008; Yu *et al*., 2015).

Reverberations are caused by P and S waves reflecting off the free surface, becoming partially trapped in the sedimentary basin (Figure 1). Low velocity sedimentary basins are associated with strong impedance contrast between the base of the sediment and crystalline basement. At the top of the sediment is the free surface, where all of the energy is reflected back into the basin. With high impedance contrasts at both surfaces, the energy is reflected and reverberates (Figure 1.1), appearing multiple times in the resulting trace and receiver function (Juliá *et al.,* 2008; Yu *et al.*, 2015). The multiple reverberations throughout the receiver function acts as noise when they are not the focus of study, obscuring other arrivals.

Figure 1.1. Representation of Ps phases and their corresponding reverberations. Black lines are P wave traces and red represents S wave. Note that a PbS reverberation could arrive at a similar time to the PPmS phase.

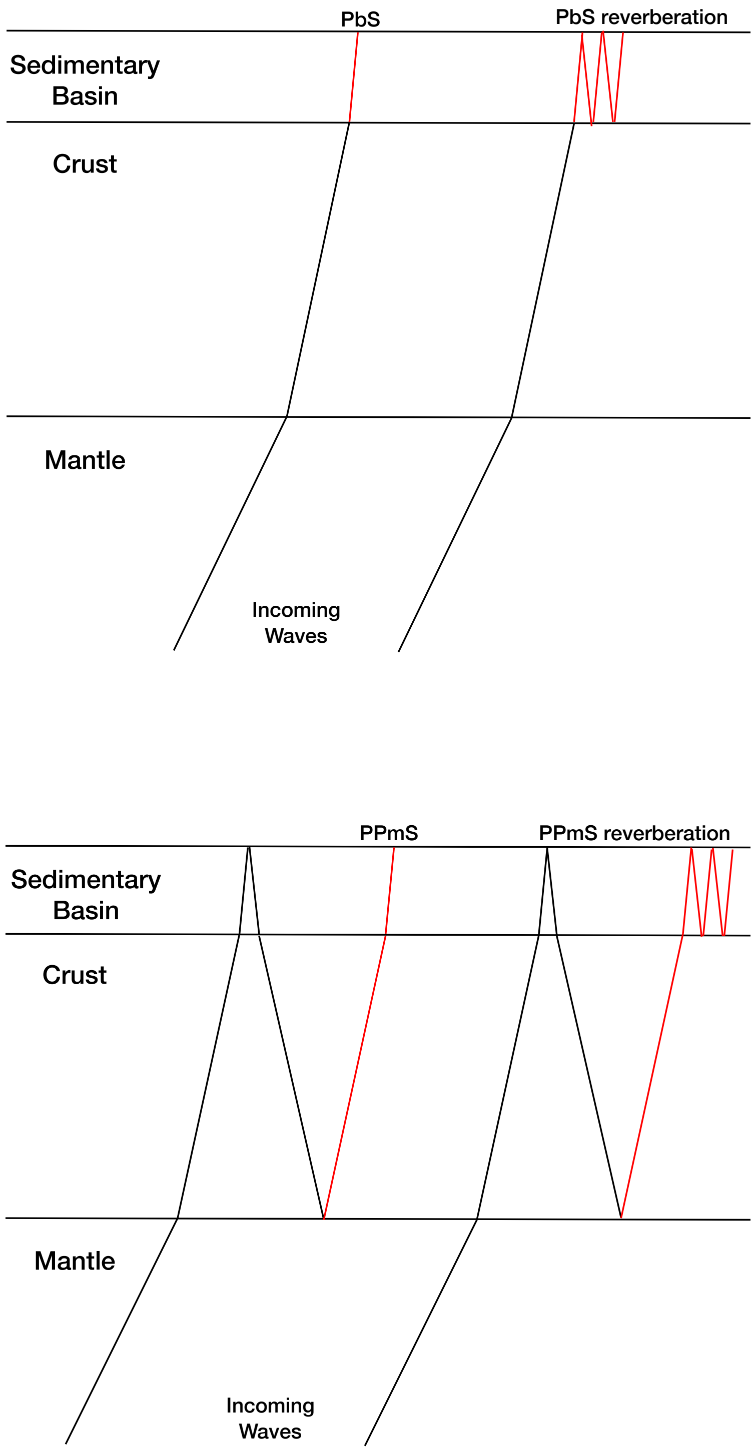

As well as generating strong reverberations, slow sedimentary basins often have other effects on the seismic data. Compared with stations on bedrock, receiver functions recorded over sediment have lower frequency first P arrivals with decreased amplitude (Yu *et al.,* 2015). The contrast between sediment and crystalline basement also generates strong upgoing P to S conversions from the shallow interface. These conversions take place as teleseismic waves travel through interfaces with non-vertical incidences. This conversion can completely mask the original P wave or combine with the original P wave arrival, widening and delaying it (Figure 1.2) (Langston, 2011; Yu *et al*., 2015).

Figure 1.2. (Top) Synthetic receiver function, where the first peak is delayed by about 1 s due to the basin Ps conversion. (Bottom) The same receiver function with the basin effects filtered out (Modified from Yu et al., 2015).

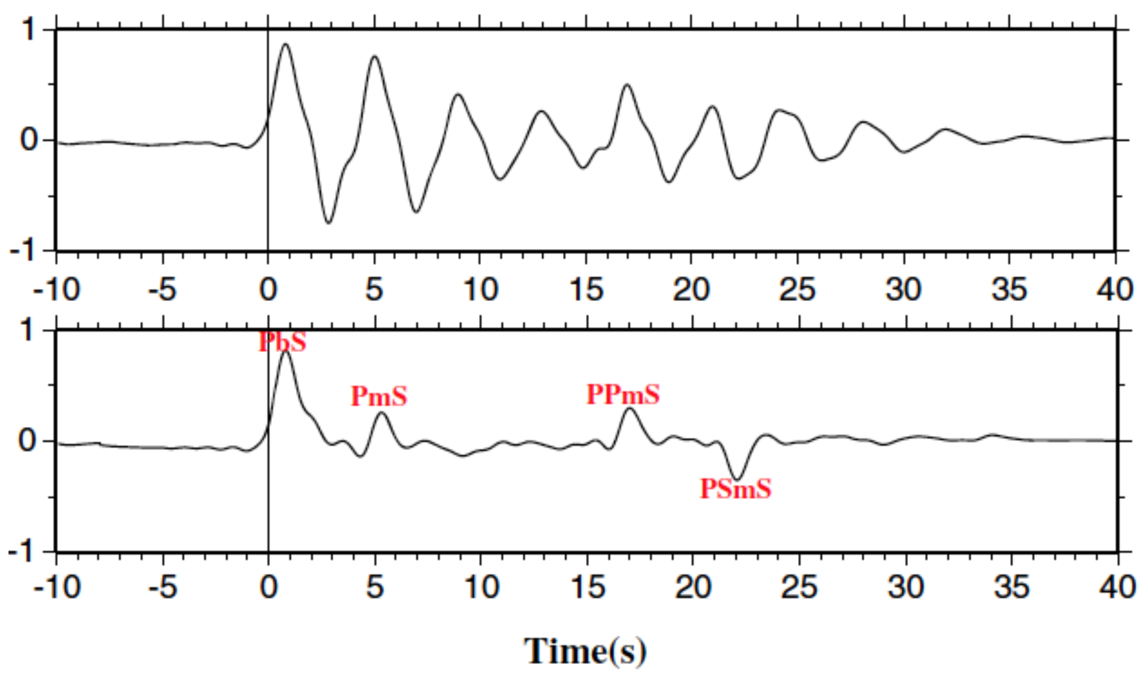

Current methods exist to remove or mitigate the effects of sedimentary derived reverberations in teleseismic data, but these methods are imperfect, and it is worthwhile to continue to search for more effective methods. Existing mitigation methods that do not require *a priori* data include standard filtering such as bandpass, sequential H-K stacking, and resonance removal filtering (Yeck *et al.*, 2013; Yu *et al*., 2015). Other techniques are more similar to this research, and use *a priori* data such as forward modelling and wavefield continuation (Zelt and Ellis, 1999; Langston, 2011; Tao *et al.,* 2014). The existing mitigation techniques and evidence for basin reverberations in teleseismic data are discussed in the second chapter.

1.2 Objectives

This study aims to develop and test a technique to filter reverberations from teleseismic data using a layer-stripping approach. Transfer functions are applied to the teleseismic response and act as an acausal filter, removing the effect of the sedimentary layer. The transfer functions are created from synthetic impulse responses, generated from crustal velocity models, using the propagator method. This research aims to determine if, using data collected over sedimentary basins and imperfect regional crustal models, the layer stripping approach can improve the quality of receiver functions and our ability to analyze it.

After a literature review was completed on the current state of geophysical techniques related to basin reverberations, a modelling technique was developed. As a starting point for research in this topic, a suite of MATLAB codes was created that calculates the theoretical response (surface displacement) from an incoming wave passing through a many-layered model using the propagator technique. Next, the transfer functions were built using this synthetic response. Chapter 3 outlines the theory of these techniques in detail.

Before the method was applied to real-world data, a synthetic test was completed to determine the effects of sedimentary basins under noise-free conditions. A test was also completed on the effectiveness of the layer-strip method with and without model imperfections.

Data for this research were obtained through the Canadian National Seismic Network, operated by Natural Resources Canada, and the EarthScope Transportable Array (Williams *et al.,* 2010; Natural Resources Canada, 2016). The first station to be used is EDM, located in Edmonton, Alberta. This station is an ideal starting place as it is located on the Western Canadian Sedimentary Basin, which has a well-researched basin velocity structure. After layer-stripping the data, analysis begins with comparing the stacked receiver functions with and without the layer-strip filter applied. Teleseismic data taken from this station are also used in an H-K stack, where the effect of the layer stripping approach is examined. A comparison of the two results will help determine the usefulness of this method.

A second data set is analyzed to further test the effectiveness of the layer-strip methodology. The data were collected at stations displayed in Figure 1.3. This larger data set with less well-known basinal velocities, for which the velocity model is based on teleseismic data, will test the limits of the method's effectiveness. The second data set was collected in North and South Dakota, Minnesota and Iowa where thick sedimentary rock are present in the Williston Basin. This stations are underlain by thicknesses of sedimentary rock varying from 100 m to 2 km (Frederiksen and Delaney, 2015).

Figure 1.3. Locations of Earthscope Transportable Array stations used in this research that transect the Williston Basin in North and South Dakota, Minnesota and Iowa.

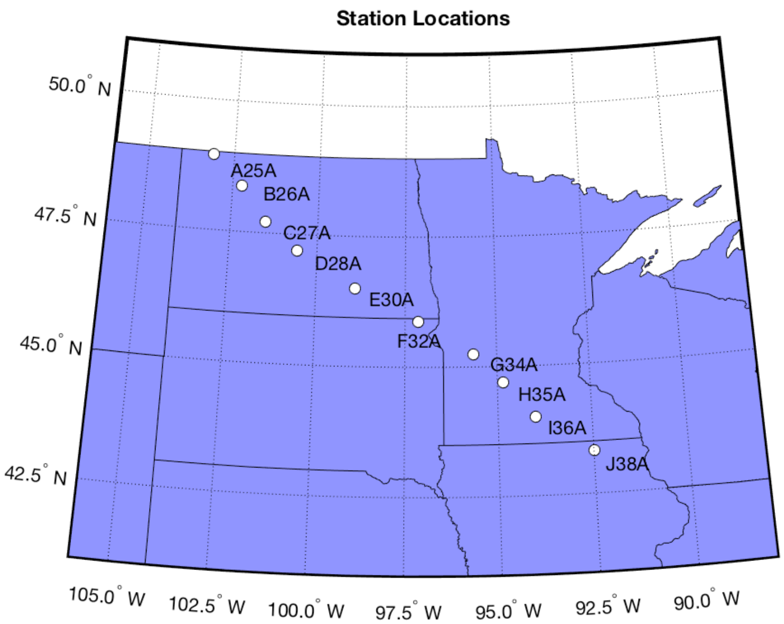

The purpose of this research is to test the layer-stripping methodology and determine if this is a viable tool to improve our ability to analyze teleseismic data over sedimentary basins. Areas of tectonic and structural interest, such as parts of the North American Mid Continental Rift and the East African Rift, are overlain by sedimentary basins. This situation provides a challenge in studying these deep structures teleseismically. If the effects of the basin can be removed more effectively, new opportunities to accurately study the seismic structure of these areas would arise.

While outside the scope of this research, the layer stripping method may also prove useful in other areas with reverberations, such as seismic studies done over thick ice sheets or in the ocean. In marine environments, seismic energy reverberates strongly in the water column, appearing in the data and obscuring crustal structure in receiver functions (Audet, 2016). This was found significantly at water column depths of 1000-2000 m (Audet, 2016). Thinner sediment layers in the marine environment can also produce strong reverberations that appear near the beginning of the waveform (Audet, 2016).

Chapter 2. The Basin Reverberation Problem

2.1 Teleseismic receiver functions

Teleseismic data may be used to constrain crust and upper mantle structure through receiver function analysis (Langston, 1979). By generating and analyzing receiver functions from three-component seismic data, we can study interface depths such as crustal thickness and seismic properties such as Vp/Vs.

As seismic waves travel through the Earth, they are altered by the structure that is encountered. For events recorded at teleseismic distances on digital three component seismometers, it is possible to deconvolve the source function from the recorded data, leaving an approximation of the Green's function on the receiver side called a receiver function (Langston, 1977; Owens *et al.,* 1984) (Figure 2.1). A receiver function approximates the receiver side portion of the Green's function, which contains the structural information on the path travelled by seismic waves. Once the receiver function is generated, it can be used to study the receiver side structure of the Earth (Zhu and Kanamori, 2000).

Figure 2.1. The path of a teleseismic ray, where the resulting data collected d(t) is a convolution of the source time function s(t), the Green's function g(t) containing the propagation effects due to structures encountered and the receiver response r(t).

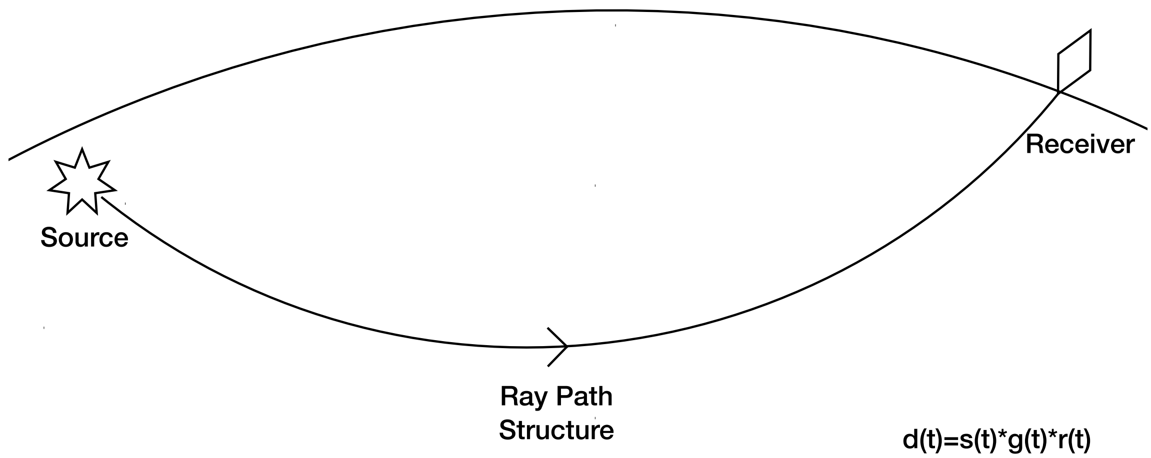

With teleseismic ray paths, the source side portion of the Green's function arrives later in time than the receiver side due to the large distance between source and receiver in teleseismic events and the velocity gap between P and S waves. Crustal heterogeneities on the source side produce new wave phases, but these arrive outside of the P coda time window. S waves, and source-side P to S conversions travel long distances as S waves, and will therefore separate in time from the P pulse between the source and receiver. A source-side P multiple will not separate in the same way, but instead arrives with the P pulse, complicating it. P to S conversions close to the P arrival must be receiver-side.

The large distance in teleseismic ray paths also means that the incoming rays arrive nearly vertically. This geometry ensures that the vertical response is dominated by P wave energy, as the motion of P waves is parallel to travel (Aki and Richards, 2002). The vertical component is an effective approximation of the source function (Owens *et al.,* 1984; Zhu and Kanamori, 2000). The radial component will include important P to S conversions, convolved with the source time function and the effects of the seismometer (Figure 2.1). The vertical component will also include impacts from the receiver/seismometer. Removing the seismometer response is done automatically and is generally trivial (Zhu and Kanamori, 2000). By deconvolving the vertical component of the seismograph from the radial component, the radial receiver function is obtained. It is most efficient to deconvolve the vertical from the radial component through spectral division, as deconvolution in the frequency domain is done simply through division (Owens *et al.,* 1984). To ensure higher frequencies are not dominated with noise, a small value is added to the denominator (vertical component) (Owens *et al.,*1984; Ammon, 1991; Cassidy, 1992).

Teleseismic data are recorded between 30 and 100° arc distance away from the source. The lower limit ensures that the incoming direct P wave is near vertical and for sources between these distances enough travel time has occurred to separate the vertical P arrival from other phases such as PcP and PP. Before 30°, the P wave triplications are observed from the upper-mantle discontinuities. Beyond 100° the core's shadow zone is observed, where seismic waves are refracted to beyond 140°. The data collected during expected arrival times at stations between 100 and 140° will not contain direct P arrivals, but instead later arrivals reflected off the inner core boundaries and core interacting arrivals such as PKiKP.

2.2 Effect of reverberations on teleseismic receiver functions

In areas with slow velocity sedimentary layers, teleseismic receiver functions contain basin P to S conversions and their multiples, as the seismic energy tends to reverberate inside the basin due to the strong impedance contrast at its upper and lower surface (Boore *et al.,* 1971; Zelt and Ellis, 1999; Julià *et. al.,* 2008; Yu *et al*., 2015). The basin reverberations (multiples) often obscure important phase arrivals in the receiver function, such as the Ps conversion from the Moho (Cassidy, 1992; Zelt and Ellis, 1999; Juliá *et al.,* 2008; Yu *et al*., 2015). The geometry of the reverberation problem is illustrated in Figure 1.1 and the effect of the basin on data is illustrated in Figure 2.2, where it is clear that the energy and number of multiples generated from the slow sedimentary basin dominate the receiver function. This synthetic data is produced using a simple model with no added noise. Figure 2.2 is produced by modelling a near-vertical incoming wave travelling through a two layer and three-layer model. Zero-time represents the starting condition of a wave plane leaving the mantle. The events are represented as displacement in time in two directions, the vertical Recorded receiver functions will produce an even greater challenge.

Figure 2.2. Synthetic Green's functions generated from models with and without a slow sedimentary basin. The upper two plots are of vertical and radial components respectively and were generated from a model that lacks a soft sedimentary basin. The lower two plots are vertical and radial components generated with a sedimentary basin.

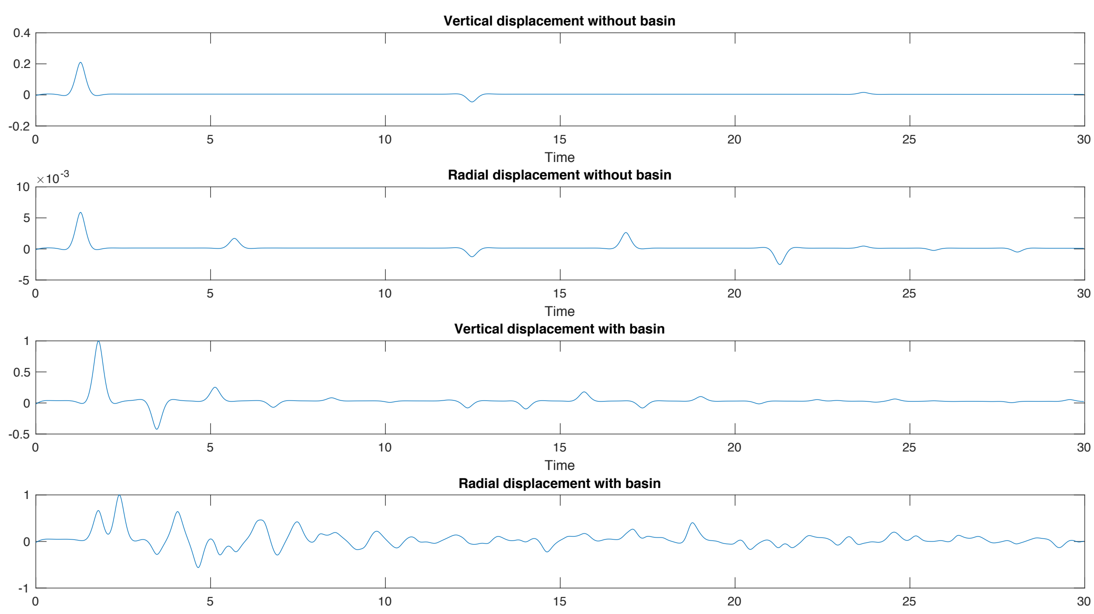

Figure 2.2 illustrates the effects of the strong impedance contrast with multiple phases producing reverberations in the basin (see bottom panel). The reflection coefficient for a downgoing P wave in the basin model used to produce Figure 2.2 is 0.48. The high coefficient indicates that a large amount of the energy will be reflected into the basin producing strong reverberations. Additionally, when compared to stations on bedrock, receiver functions recorded over sediment have wide first P arrivals with decreased amplitude as well as noisy responses at later times (Clitheroe *et al.,* 2000; Yu *et al.,* 2015). Contrast between sedimentary rocks and crystalline basement creates strong P to S conversions, often with the converted phase combining with an original arrival (if it is close in time) in the radial direction, widening and delaying it (Figure 2.2) (Zelt and Ellis, 1999; Langston, 2011; Yu *et al*., 2015). A second example of the effects of sedimentary layer reverberations is illustrated in Figure 1.2, where strong sedimentary multiples are generated by a sedimentary rock layer within the synthetic model.

The cluttering of receiver functions often leads to inaccurate estimations of layer thickness and Vp/Vs ratios. Yeck et al. (2013) calculated that the existence of a deep, slow velocity basin can skew crustal thickness estimates more than 10 km when using the H- K stacking technique. Because sedimentary basins are found throughout the world, techniques to mitigate the effects of these basins on receiver functions have been investigated in the past.

2.3 Areas prone to basin reverberations

A large fraction of the Earth's surface is covered in soft sedimentary layers that vary greatly in thickness. The thickness and the impedance contrast between these sedimentary layers and the underlying rock will determine the frequency and strength of resulting reverberations as well as the early time effects on the receiver function (Zelt and Ellis, 1999; Langston, 2011; Yu *et al.,* 2015). Sheehan *et al.* (1995) found that the Denver Basin (<5 km) introduced a phase lag into the 0 s arrival, along with apparent higher Vp/Vs and uncertainty in results in the thickest part of the basin. Langston (2011) studied deep sediments along the Gulf of Mexico and Atlantic Coastal Plains which attain thicknesses of 10 km or more. It was found that the sediments mask deeper crustal phases through reverberations that caused late large-amplitude arrivals. The thick sediments of the southeastern United States also amplify ambient noise levels, which reduces signal-to-noise ratios (Langston, 2011).

Tao *et al.* (2014) completed wave-field continuation and decomposition on a station located on the Songliao Basin in Northeast China. The basin thickness was determined to be 0.31 km, which agrees with active source data. At this relatively low thickness, the radial components of all the events still contain strong sediment reverberations that mask important weaker Ps conversions from deeper interfaces. Mandal (2006) determined that in India the Kachchh Basin receiver functions are characterized by strong distinct Ps conversions from both the Moho and basement-sediment transition while the basin Ps conversions are weak or absent in the Saurashtra Basin. The Kachchh Basin is 1–3 km thick with a relatively low velocity compared with the Saurashtra Basin which varies from 0-1 km thick and has a moderate velocity. These observations indicate that with a thicker sediment layer, and stronger impedance contrast, more energy will be converted to a Ps phase at the base of the sediment layer, and basin reverberations will be stronger.

The previous studies indicate that sedimentary basins between 0.3 and 5 km may produce basin reverberations. The two basins used to test the layer-strip methodology in this research are the Western Canadian Sedimentary Basin and the Williston Basin, both located in North America. These basins are in this prescribed thickness range and should act as effective test areas. The geology of these basins will be detailed in Chapters 6 and 7.

2.4 Current basin reverberation mitigation techniques

Techniques have been developed to both filter out the effects of the sedimentary basins and to determine crustal structure in the presence of the basin reverberations. Some of these methods are more effective than others, but each have disadvantages. One of the first techniques developed was forward modelling, where synthetic waveforms are fit to observed receiver functions and a velocity model is built by adding deeper interfaces to fit progressively later phases. This technique was originally used in areas without basin reverberation problems (Ammon *et al.,* 1990; Baker *et al.,* 1996). The technique was also used in areas with thick sedimentary basins, where forward modelling was used to estimate the basin structure and the deeper crust (Sheehan *et al.,* 1995; Zelt and Ellis, 1999, Clitheroe *et al.,* 2000; Mandal, 2006). This technique was used with the anticipation that it would work despite the basinal noise. Zelt and Ellis (1999) reported difficulties with forward modelling in areas with sedimentary basins, as the reverberations reduce the level of detail that can be resolved. Clitheroe *et al.* (2000) also demonstrated that fitting the receiver functions can be unreliable due to the later reverberations.

Band pass and band rejection filters are useful in mitigating basin reverberations. They work by filtering bands of frequency in data either exclusively or inclusively. Ideally the data that are removed correspond with basin reverberations and other noise, and not with the signal of interest. Choosing ideal frequency bands is problematic and can lead to incomplete filtering of basin reverberations as frequencies containing basin reverberations will overlap with those containing important arrivals (Leahy *et al.,* 2012; Reed *et al.,* 2014).

Another technique, wave-field continuation and decomposition, is at least moderately effective at estimating crustal parameters beneath sedimentary basins and mitigating the reverberation problem (Langston, 2011, Tao *et al*., 2014). This technique is similar to the one used in this research, as it uses the propagator matrix method to generate synthetic waveforms, and the effectiveness of the filter is based on the quality of the input model. Langston (2011) uses a station outside of the thick sedimentary basin to estimate the source time function for each event. Sediment models are derived from a grid search for the best fit between the original data and synthetic data generated with a grid of models. The sedimentary thickness is estimated and used as *a priori* data, and the velocity structure of the sedimentary basin is used as the parameters for the grid search. Searching for maximum fit between the sedimentary model and the recorded data is possible as the earthquake data are dominated by the response of the sedimentary structure, so the fit will depend strongly on the sedimentary structure. The original data are subsequently downward continued (i.e. calculated as if they were below the sedimentary basin) using the propagator matrix technique (Figure 2.3).

Figure 2.3. S conversions downward continued to 10 km from various events and their stacked combination. Grey shaded area shows non-causal S arrival and top panel is the synthetic response of the model without sedimentary layers. Stacked downward continued waveforms preserve main features of the converted S waves in the expected result of the synthetic produced top panel (taken from Langston, 2011).

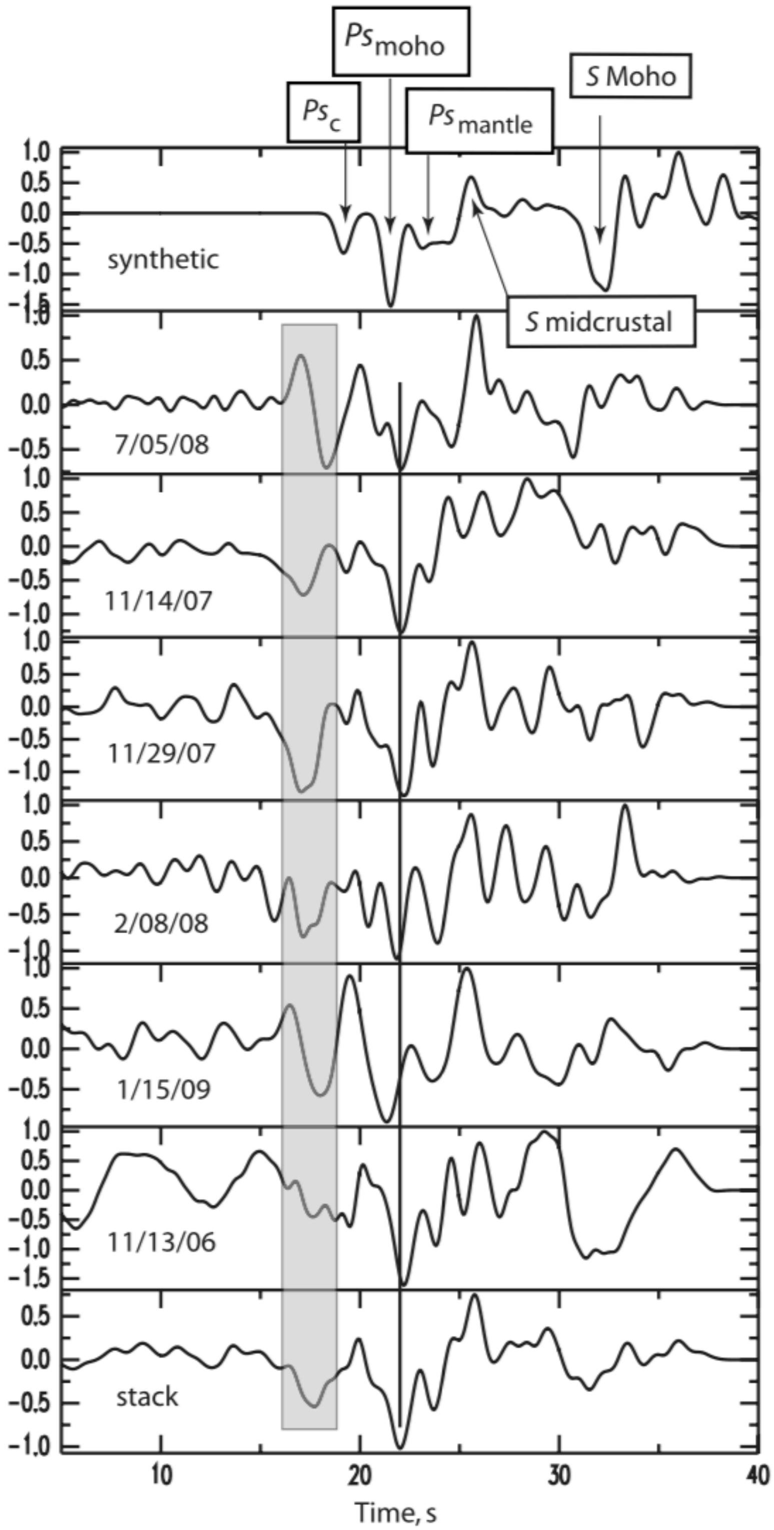

Langston (2011) found that the assumed sedimentary basin model was a very important factor in obtaining effective results, which means the quality of the results is highly dependent on the chosen model. Therefore, the method only works under conditions in which the layer thicknesses are known, as the grid search is designed to obtain velocities and not thicknesses. The main difference between the methodology in Langston (2011) and in this research is that Langston (2011) uses a reference station for the source function, inverts for velocity structure, and wave field continues the data to determine the S wave field at 10 km depth. Instead, this research produces a filter from two synthetic Green's functions and generates a filtered receiver function for the surface location. Because the Langston (2011) technique does not produce filtered receiver functions, it is hard to compare with the results of this thesis.

Tao *et al.* (2014) derived an alternative to using *a priori* information for wavefield downward continuation. Upgoing S wave energy is presumed to be absent in the half-space (either the lower crust or mantle). A search is completed for the velocity and layer structure that minimizes S-wave energy flux upwards from the half-space. The sedimentary model is solved for based on the parameters for which the flux is minimized, such that a-priory model information is not needed. This method is computationally expensive, even today, as the inversion contains a high number of parameters (Langston, 2011; Tao *et al*., 2014, Yu *et al.,* 2015).

Another technique applied to produce useful responses despite basin reverberations uses a 2-layer H-K stack completed sequentially downward (Yeck *et al.,* 2013). An H-K stack is first performed to analyze basin properties using higher frequencies. It is presumed that the higher frequency component of the data is most sensitive to basin properties. Next a more conventional H-K stack is performed to determine crustal thickness, but a time adjustment is applied based on the first iteration. An H-K stack is a search for crustal thickness and P to S velocity ratio. H-K stacking is further defined in Chapter 3. The sequential H-K stacking method was used to determine sedimentary and crustal structures and is effective when the Ps phase masking is light (Yeck *et al.,* 2013).

Yu *et al*. (2015) use a resonance removal filter to mitigate the effects of basin reverberations in receiver functions. Near-surface reverberations are theoretically eliminated from the observed RF by designing a resonance removal filter:

$$1 + r_0 e^{-i\omega\Delta t} \qquad (2.1)$$

The filter uses the strength of the reverberations (r_0) and the two-way travel time of the sedimentary layer (Δt), which can be determined from the autocorrelation of the observed receiver function. After calculating the autocorrelation, the strength of the reverberations is calculated from the unit amplitude ratio of the first trough, and time to first peak is the two-way travel time (Yu *et al*., 2015). After the filter is applied, the Moho and PbS phases show up clearly in filtered receiver functions (Figure 1.2). To retrieve the full structure, an H-K stack is performed on the filtered and time corrected receiver function to obtain the subsedimentary Vp/Vs and depth to discontinuities. Finally, this information is used in another H-K stack to calculate the sedimentary thickness and Vp/Vs of the basin (Yu *et al*., 2015). This technique has been shown to be effective (Figure 2.4), and is useful for areas with clearly defined reverberations at a single frequency. Figure 2.4 demonstrates the 10 km difference in calculated crustal thickness between unfiltered data and filtered data. This technique works best with a single resonant frequency due to the frequency dependence of the removal filter (Yu *et al*., 2015).

Figure 2.4 Data recorded at the Songliao Basin, northeast China. (a) Synthetic receiver functions (RFs) with 15% added noise. The red trace is the stacked summation without moveout correction. (b) Autocorrelations of each RF in Figure 2.3.a. (c) Contour from H-k stacking grid search using the RFs shown in Figure 3a. (d) Resulting RFs after the application of resonance removal filters. (e) Contour grid search from H−k stacking using the filtered RFs shown in Figure 3d. (f) Contour of H-K stacking grid search for sediment thickness and Vp/Vs (Yu *et al*., 2015).

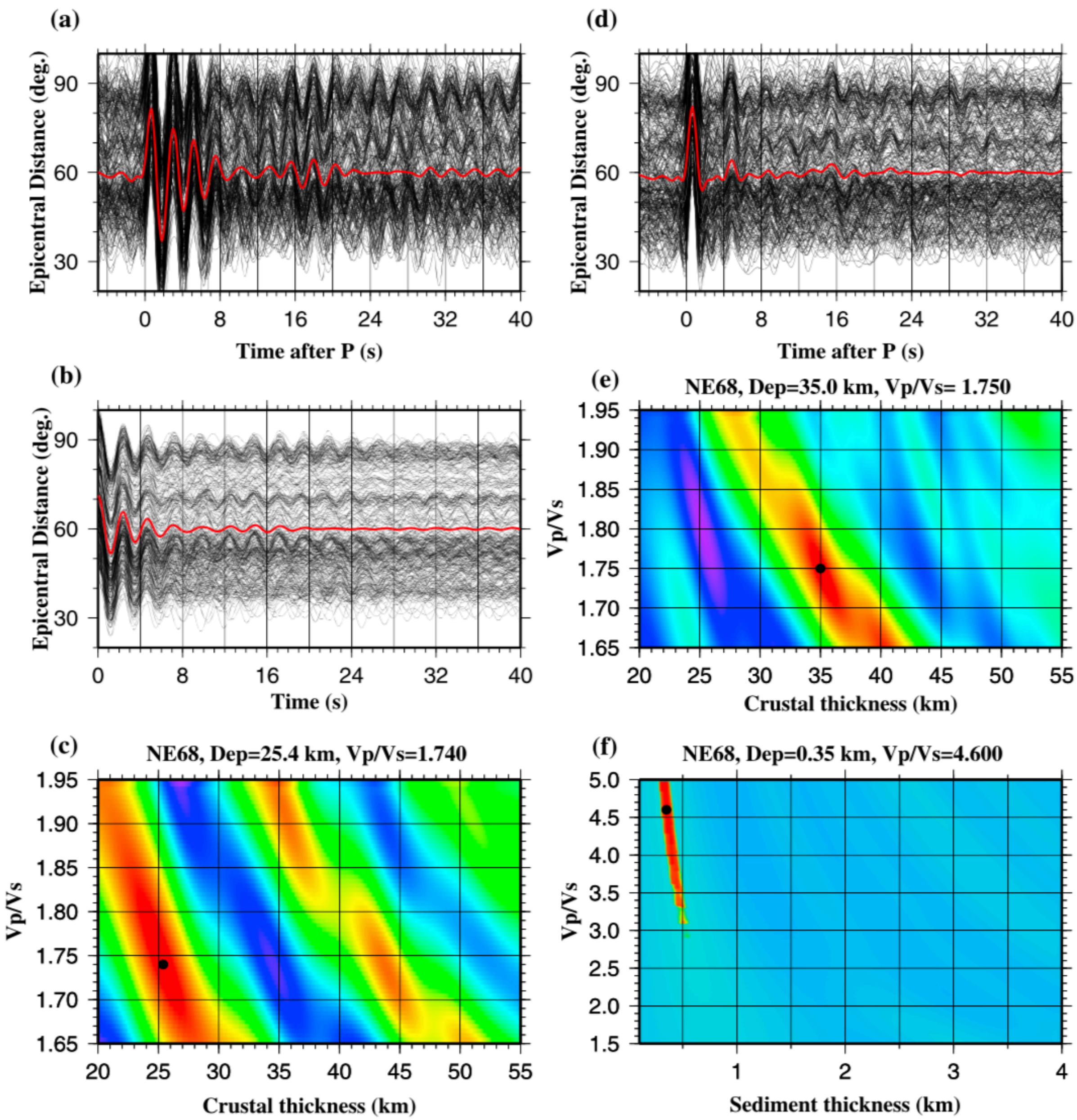

As outlined, techniques exist to mitigate the basin reverberation problem. None of these methods are effective in all circumstances. To continue to improve our ability to perform teleseismic research over areas of thick sedimentary rock, new methods must be developed and tested. This research project explores a new methodology for filtering teleseismic basin noise based on inter-model transfer functions.

Chapter 3. Theory

3.1 The propagator method

In order to filter out sedimentary basin effects with transfer functions, synthetic Green's functions must be generated. The Green's function is the impulse response of a linear differential operator given a specific initial condition or Dirac source. The Green's function can be used to represent planar waves in cases where the source is distant, and waves appear planar. The synthetic Greens functions are used to generate the transfer function that is applied to the observed data. The transfer function is made by taking the ratio of two synthetic Green's functions and is applied to filter out basin reverberations. For each component of each recorded event at a station, two synthetic seismic responses are calculated using the propagator method to produce a transfer function. One response is generated from a model with the basin present and the second is modeled without the basin.

The propagator method was chosen to produce the synthetic data because it is a physically accurate representation of a plane wave interacting with homogeneous stacked elastic layers in 1-dimensional models (Thomson, 1950; Haskell, 1962; Aki and Richards, 2002; Tao *et al.*, 2014). This technique also has a historical basis for use in producing synthetic seismic data (Haskell, 1962; Aki and Richards, 2002; Yu *et al.,* 2015; Tao *et al.*, 2014). This method takes into consideration each subsurface layer and the full wave interactions between and inside the layers (Aki and Richards, 2002).

This description of the propagator method is summarized from Aki and Richards (2002). To calculate a synthetic trace, we start by formulating a problem where plane waves are travelling vertically through a layered medium. The *a priori* known values in this problem are the seismic properties of each layer and the initial wave amplitude travelling upwards from a half space. We can start with an equation that defines the physics of the problem in the frequency domain:

$$\mathbf{y} = \mathbf{F}\mathbf{w} \tag{3.1}$$

where **y** contains particle displacement and stress as a function of depth in the P-SV wave system, **w** represents the wavefield in a layer. **F** is the fundamental matrix, containing eigenvectors as columns, which propagates the wavefield to depth corresponding to **y**. As **w** is a vector of wave-mode amplitudes in a layer, it is continuous throughout a layer, while **y** is not. **y** is however continuous across interfaces within welded boundary conditions. Equation 3.1 allows us to convert between the two. This problem is defined in the P and SV energy system, for which only the z and x directions are of consequence. **y** is defined as a vector containing the vertical and horizontal displacement inside a uniform layer (v_x v_z) and the shear and normal stress as a function of depth (τ_{zx} τ_{zz}):

$$\mathbf{y} = \begin{pmatrix} v_x \\ v_z \\ \tau_{zx} \\ \tau_{zz} \end{pmatrix} = \begin{pmatrix} v_x \\ v_z \\ 0 \\ 0 \end{pmatrix}_{z=0} \tag{3.2}$$

At the free surface, the traction in both directions will be 0 (Haskell, 1962). v_x is effectively the radial response in the frequency-domain form, and v_z is the vertical response in frequency domain. The aim of this theory is to generate the surface displacement or velocity function, which is contained in vector **y** in Equation 3.2. It is sometimes called the motion stress vector (Tao *et al.*, 2014).

To continue, it is assumed that there is no slip between subsurface layers, and therefore a perfect elastic relationship exists at interfaces. This assumption is valid everywhere outside the rupture zone of the source earthquake. Under this assumption, stress and displacement are continuous across an interface between layers 1 and 2 and are equal to the fundamental matrix in one layer multiplied by the wave field in the same layer;

$$\mathbf{F}_1\mathbf{w}_1 = \mathbf{y}_{12} = \mathbf{F}_2\mathbf{w}_2 \qquad (3.3)$$

or

$$\mathbf{w}_1 = \mathbf{F}_1^{-1}\mathbf{F}_2\mathbf{w}_2 \qquad (3.4)$$

The wave corresponding to $\mathbf{F}_2$ will propagate to $\mathbf{F}_1$, thus at the boundary the waves are equal. Using Equation 3.3 and 3.4, any wavefield can be calculated if all of the fundamental matrices are known in all layers, given a known starting condition, $\mathbf{W}_{N+1}$. The equation to calculate the wave condition in the uppermost layer becomes

$$\mathbf{W}_0 = \mathbf{F}_1^{-1}(z_1)\mathbf{F}_2(z_1)\mathbf{F}_2^{-1}(z_2)\mathbf{F}_3(z_2)\ldots\mathbf{F}_N^{-1}(z_N)\mathbf{F}_{N+1}(z_N)\mathbf{W}_{N+1} \qquad (3.5)$$

Re-arranging a final time to derive an equation for the motion and stress at the surface ($\mathbf{y}$) instead of the uppermost wavefield ($\mathbf{W}_0$) produces an equation that calculates surface displacement based on a wavefield starting in a half space ($\mathbf{W}_{N+1}$) propagating through layers (Aki and Richards, 2002):

$$\mathbf{y} = \mathbf{F}_1(0)\mathbf{F}_1^{-1}(z_1)\mathbf{F}_2(z_1)\mathbf{F}_2^{-1}(z_2)\mathbf{F}_3(z_2)\ldots\mathbf{F}_N^{-1}(z_N)\mathbf{F}_{N+1}(z_N)\mathbf{W}_{N+1} \qquad (3.6)$$

The theoretical $\mathbf{y}$ is calculated by propagating the wavefield in the bottom layer, $\mathbf{W}_{N+1}$ in Equation 3.6, using matrices $\mathbf{F}_{N+1}(z_N)$ and $\mathbf{F}_N^{-1}(z_N)$, *etc.*, to the surface where z=0. Equation 3.6 describes an upgoing wave starting in a half space, its interactions with the layers of the model and the resulting surface displacement (Figure 3.1). Equation 3.6 represents displacement and stress and traction at the free surface, with displacement in the x and z direction and zero traction. Equation 3.7 defines the initial wave field in the half-space, with unknown variables for the reflected P and SV waves (R_P R_{SV}), and an upgoing P wave amplitude of 1 and upgoing SV wave amplitude of zero (U_P U_{SV}):

$$\mathbf{W}_{N+1} = \begin{pmatrix} U_P \\ U_{SV} \\ R_P \\ R_{SV} \end{pmatrix} = \begin{pmatrix} 1 \\ 0 \\ R_P \\ R_{SV} \end{pmatrix} \tag{3.7}$$

Figure 3.1. Representation of the layer geometry with the F_N calculated using values from the N[th] layer.

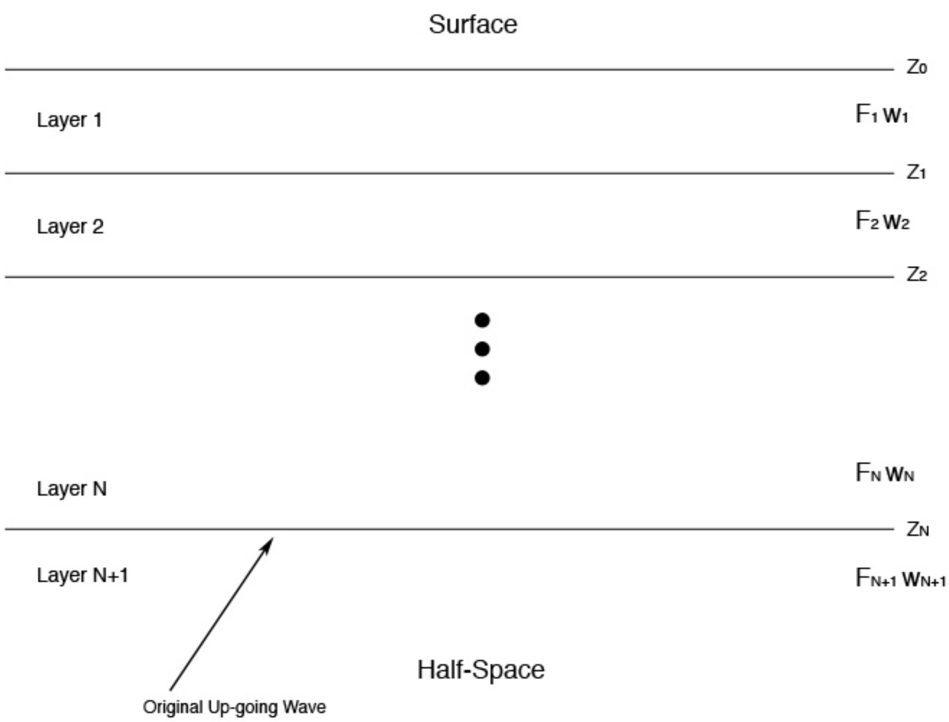

This method is often referred to as the propagator matrix method because the propagator function $\mathbf{F}_N^{-1}(z_N)\mathbf{F}_{N+1}(z_N)$ allows for a wavefield to be propagated through layers as the boundary conditions match across interfaces. The fundamental matrices, such as $\mathbf{F}_{N+1}(z_N)$, from Equation 3.5 and 3.6 are most effectively represented by a matrix multiplication of $\mathbf{E\Lambda}$ taken from Aki and Richards (2002), where $\mathbf{E}$ and $\mathbf{\Lambda}$ are defined as

$$\mathbf{E} = \begin{pmatrix} \alpha p & \beta\eta & \alpha p & \beta\eta \\ \alpha\xi & -\beta\eta & -\alpha\xi & \beta p \\ 2i\omega\rho\alpha\beta^2 p\xi & i\omega\rho\beta(1-2\beta^2p^2) & -2i\omega\rho\beta^2\rho\xi & -i\omega\rho\beta(1-2\beta^2p^2) \\ i\omega\rho\alpha(1-2\beta^2p^2) & -2i\omega\rho\beta^3 p\eta & i\omega\rho\alpha(1-2\beta^2p^2) & -2i\omega\rho\beta^3 p\eta \end{pmatrix} \tag{3.8}$$

and

$$\mathbf{\Lambda} = \begin{pmatrix} \exp\,[i\omega\xi(z - z_{ref})] & 0 & 0 & 0 \\ 0 & \exp\,[i\omega\xi(z - z_{ref})] & 0 & 0 \\ 0 & 0 & \exp\,[i\omega\xi(z - z_{ref})] & 0 \\ 0 & 0 & 0 & \exp\,[i\omega\xi(z - z_{ref})] \end{pmatrix} \tag{3.9}$$

Within **E** and **Λ,** the variables are defined in Table 3.1 and the following two equations:

$$\xi = \sqrt{\frac{1}{\alpha^2} - p^2} \tag{3.10}$$

$$\eta = \sqrt{\frac{1}{\beta^2} - p^2} \tag{3.11}$$

Table 3.1: List of variables used in propagator Equations 3.8 through 3.11

α	P velocity
β	S velocity
p	ray parameter
ρ	density
z	depth to interface (Figure 3.1)
z_{ref}	chosen as 0
ω	angular frequency (2π Hz)

As an example, $\mathbf{F}_{N+1}(z_N)$ refers to the fundamental matrix calculated using the physical properties of layer N+1 in Equation 3.8 and the depth to the "nth" interface as z in Equation 3.9 (Figure 3.1). After each fundamental matrix in Equation 3.6 is calculated, v_x and v_z can be determined by solving a 4x4 system of equations (Equation 3.12).

$$\begin{pmatrix} v_x \\ v_z \\ 0 \\ 0 \end{pmatrix} = \begin{pmatrix} M_{11} & M_{12} & M_{13} & M_{14} \\ M_{21} & M_{22} & M_{23} & M_{24} \\ M_{31} & M_{32} & M_{33} & M_{34} \\ M_{41} & M_{42} & M_{43} & M_{44} \end{pmatrix} \begin{pmatrix} 1 \\ 0 \\ R_P \\ R_{SV} \end{pmatrix} \tag{3.12}$$

In Equation 3.12, a matrix containing values M is calculated from the multiplication of all fundamental matrices. Up until this point, the solution has been a function of frequency (Equation 3.8). Once the two displacement spectra are calculated, they are converted to a time series using an inverse Fourier transform producing the synthetic response in time domain.

3.2 Layer-stripping with transfer functions

The transfer function approach to layer-stripping uses a transfer function generated from two synthetic Green's functions to filter out the reverberations/effect of the basin. The two synthetic responses used in the transfer function are generated from a model without the sedimentary layer and from a model with the sedimentary layer. Each transfer function is an operator that converts one trace (data that include the sedimentary layer effects) to another (that theoretically does not include the effects of the sedimentary layer).

The process of creating the synthetic traces is outlined in section 3.1 and is done using the propagator method. Transfer functions are calculated in the frequency domain to allow for spectral division. The transfer functions $T_{1,2}^{R}$ and $T_{1,2}^{Z}$ for the radial and vertical components are calculated from the corresponding components of responses from model 1 with the basin and model 2 without the basin (R_1 is the radial component generated from model 1, Z_2 is the vertical component derived from model 2):

$$T_{1,2}^{R} = \frac{R_2 R_1^*}{R_1 R_1^* + \delta} \tag{3.13}$$

$$T_{1,2}^{Z} = \frac{Z_2 Z_1^*}{Z_1 Z_1^* + \delta} \tag{3.14}$$

In these equations δ is a small number (defaulting to 1e-7) used to stabilize the equation. The complex conjugate is used to ensure the denominator is real. The vertical and radial responses will be filtered with $T_{1,2}^{R}$ and $T_{1,2}^{Z}$ before the receiver function is generated, this allows for an extra step of visualization of the direct effects of the transfer function before the receiver function is calculated. It is also predicted that applying it before the receiver function is produced is more stable, as the majority of the effect is in the radial domain.

To apply the filter a circular convolution is used. Transfer function $T_{1,2}^{R}$ is convolved with the radial component of the observed data and $T_{1,2}^{Z}$ is circularly convolved with the vertical component of the observed data in the time domain. This technique can lead to late time seismic signals wrapping around and entering into the start of the resulting time series. Zero padding inserted into the end of the functions prior to the circular convolution avoids this. Alternatively, the result is windowed and at later times, the values trend to zero. No wrap around effect was observed in the results. A receiver function is generated in this way with the newly filtered vertical and radial component.

3.3 Receiver function calculation

Receiver functions, which are estimates of the receiver side of the Green's function, are calculated through spectral division of the vertical and radial components of the observed data, where the vertical component is taken to approximate the source function (Chapter 2). In the simplest form this is achieved through spectral division to solve for the receiver function $G_R(\omega)$:

$$G_R(\omega) = \frac{R(\omega)}{Z(\omega)} \tag{3.15}$$

The simple spectral division is not robust. At higher frequencies, where $Z(\omega)$ is dominated by low values, the division produces high energy noise in the resulting receiver function (Clayton and Wiggins, 1976). Because there are frequencies where the signal is 0 or near 0, the deconvolution will require regularization to avoid dividing by 0. Regularization ensures that the receiver function is dominated by frequencies at which $Z(\omega)$ contains signal above noise levels. The equation for the Green's function becomes

$$G_R(\omega) = \frac{R(\omega)Z^*(\omega)}{Z^*(\omega)Z(\omega)+\delta^2} \tag{3.16}$$

The damping factor δ is added to regularize the equation, and to ensure a minimum value in the denominator, even when $Z(\omega)$ is near 0. The conjugate, $Z^*(\omega)$ multiplies by the numerator and denominator to convert the denominator to a real number. This ensures the phase remains unchanged by δ and that the result is a least squares estimate of the receiver function.

3.4 H-K stacking

The H-K stacking technique can be used to obtain estimates of crustal thickness (H) and Vp/Vs (K) from stacked receiver functions. Each receiver function provides a point measurement of crustal thickness that is less sensitive to crustal P velocities than other methods because it treats the direct P arrival as a reference for later Ps arrivals. This technique was chosen because it has a long history of use in receiver function analysis and will be an effective way to measure the changes in layer-stripped receiver functions (Zhu and Kanamori, 2000; Crotwell and Owens, 2005; Eaton *et al.,* 2006; Yuan *et al.,* 2010).

The H-K stacking technique does not require the user to select arrival times for each waveform. Instead, a range of crustal thicknesses and Vp/Vs values are used to calculate theoretical arrival times of Ps phases and the energy at the predicted times is stacked over all traces (Zhu and Kanamori, 2000; Eaton *et al.,* 2006). The thickness (H) and Vp/Vs (K) at which the highest stacked energy is located provides the estimate for these values. Events with different directions and distances are used, which averages over the effects of lateral structural heterogeneities (Zhu and Kanamori, 2000). The H-K stacking method works on the principle that P to S conversions are generated by the Moho, which is the strongest receiver side contrast seismic waves pass through (Zhu and Kanamori, 2000). The time separation between Ps and P waves can be used to estimate the depth to the Moho:

$$H = \frac{T_{Ps}}{\sqrt{\frac{1}{V_S^2}-p^2}-\sqrt{\frac{1}{V_P^2}-p^2}} \qquad (3.17)$$

In Equation 3.17, T_{Ps} is the time delay between P and Ps arrival. The time or P to S phase arrivals are defined by crustal thickness H and properties within equations 3.10 and 3.11. Using Equation 3.17 to invert for H and K proves ambiguous, and uncertainty in K leads to a non-unique answer (Zhu and Kanamori, 2000). Adding constraints that incorporate the PpPs and PpSs+PsPs phases into the calculations can reduce the ambiguity of the inversion results. The PpPs and PpSs+PsPs phases ray path is represented in Figure 3.2.

Figure 3.2. Ray-tracing diagram for PpPs, PpSs+PsPs and Ps teleseismic phase arrivals. The example shown has a 40 km thick crust (Salah *et al.*, 2009).

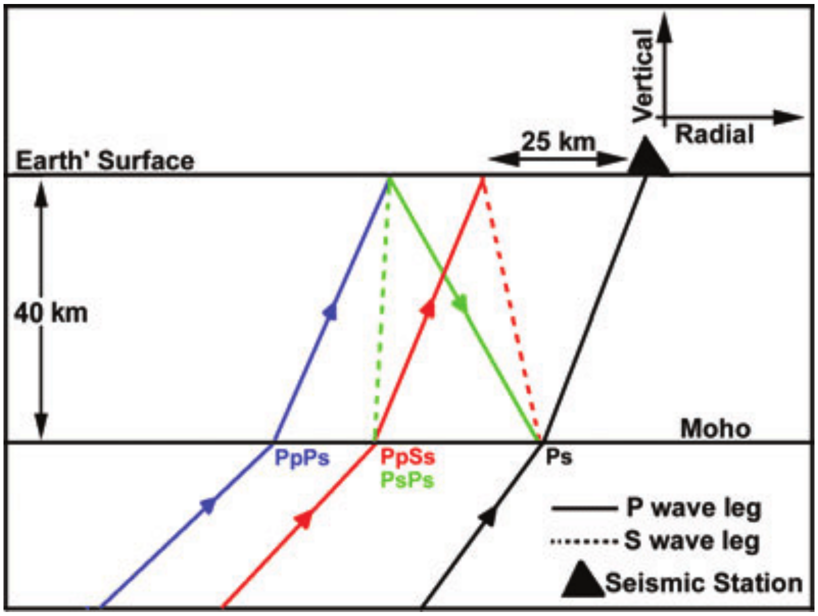

Using the time of the phase arrivals, H can be calculated in two additional ways:

$$H = \frac{T_{PpPs}}{\sqrt{\frac{1}{V_S^2}-p^2}+\sqrt{\frac{1}{V_P^2}-p^2}} \tag{3.18}$$

$$H = \frac{T_{PpSs+PsPs}}{2\sqrt{\frac{1}{V_S^2}-p^2}} \tag{3.19}$$

Identifying the converted P phases for a single receiver function trace can be very difficult because of background noise and basin reverberations. The signal to noise ratio can be increased by stacking multiple events and incorporating multiple phase arrivals, and for this study a N^{th} root stack was used (Equation 3.20) where M traces are stacked. This technique reduces the stack's tendency to give higher weight to larger amplitude arrivals when compared with a linear stack. This maximizes the effect of properly located but small amplitude arrivals of P to S phases.

$$S_{nth}(H,K) = \left[\sum_{i=1}^{3}\sum_{j=1}^{M} w_i \left|r_j(t_{ij})\right|^{\frac{1}{N}} \operatorname{sign}\left(r_j(t_{ij})\right)\right]^N \quad (3.20)$$

In Equation 3.20, $r_j(t_{ij})$ are receiver functions, t_{1j}, t_{2j}, t_{3j} are predicted Ps, PpPs and PpSs+PsPs arrival times, respectively, and w_i are weighting factors such that $\sum w_i = 1$. The $S_{nth}(H,K)$ is at maximum when all three phases are stacked coherently, resulting in the estimate of H and K. The algorithm uses a grid of H and K values to produce a range of predicted arrival times such that the predicted arrival times with highest stacked amplitude are used to obtain the best estimate for the H and K at that location (Figures 3.3 and 3.4). The Nth root stacking technique favours coherence over amplitude, leading to a signal-enhancement stack that is less sensitive to noise. MATLAB scripts were used to produce 4th root H-K stacks for this research. The scripts were provided by Dr. Andrew Frederiksen prior to the start of this research.

Figure 3.3. Synthetic representation of the H-K stacking method, where the result is located where the energy is the highest. This takes place where the contributions from all of the phases intersect for the predicted arrival times of each phase (Zhu and Kanamori, 2000).

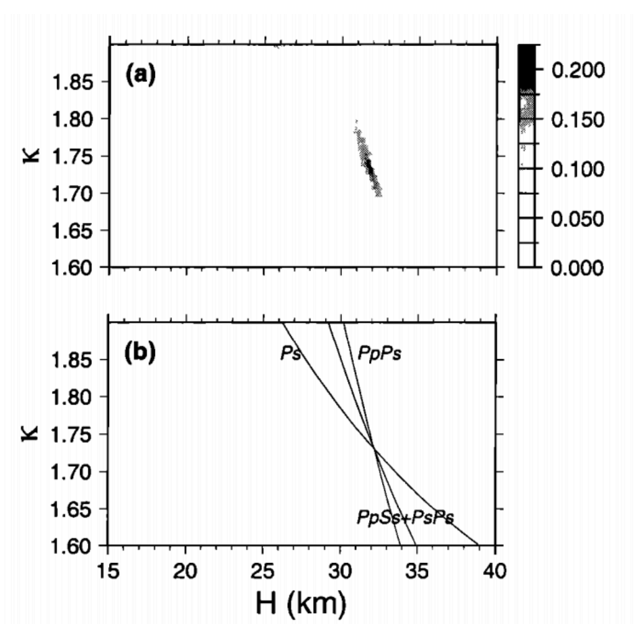

Figure 3.4. Representation of the stacking of receiver functions by ray parameter to produce the stacked value at each phase. The highest energy for each phase is denoted by the lines, which are the times used for Equations 3.17, 3.18 and 3.19 (Zhu and Kanamori, 2000).

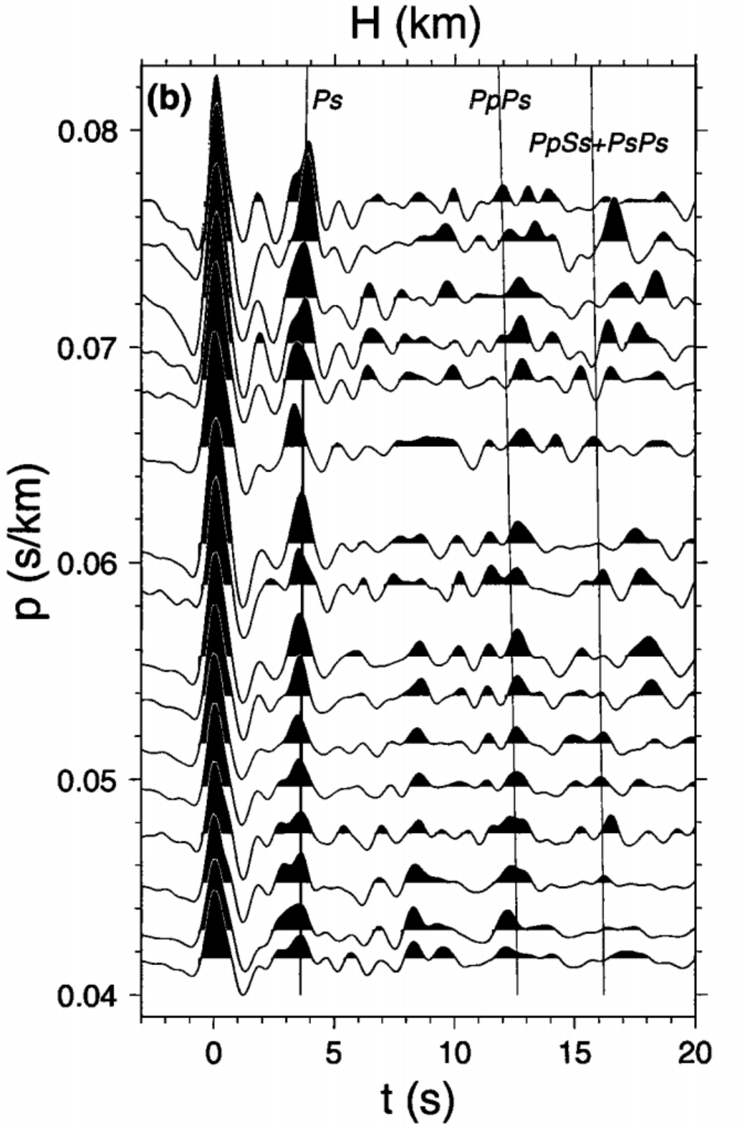

Chapter 4. Synthetic Tests

4.1 Basis for synthetic tests

This chapter will outline the two main research objectives related to the production of synthetic seismic data. First, synthetic seismic responses are produced to help outline the changes to seismic data travelling through sedimentary basins. Second, the chapter will cover tests where synthetic waves are filtered using transfer functions. This will test the transfer function methodology and its ability to filter out basinal noise with models of varying accuracy.

As a starting point, a MATLAB program was created that calculates the theoretical response (surface displacement) produced by an incoming wave entering a layered model. This was done using the propagator method for both the SH (horizontal shear) wave and the P-SV (propagation direction and the in-plane shear) wave. Seismic energy can be broken into these two wave domains as the SH waves do not interact or produce P or SV waves. This technique assumes no slip between interfaces, uses a 1-dimensional model and does not apply attenuation. It is used to determine the response in the frequency and time domains from various models, with sedimentary basins present and not present.

It is expected that under ideal conditions for the synthetic layer-strip test (with zero noise and a perfectly accurate model used to generate the filter), the layer-strip will completely remove the effects of the sedimentary layers, as the same velocity basin model and approach is used for both the synthetic response and the filter. Instead it is important to test how the layer-strip will perform if the model used to generate the filter is different from the model used to generate the synthetic data. This test will more accurately represent the real-world problem, as the model used to generate the transfer function will not perfectly represent the underlying structure.

4.2 The effect of sedimentary basins on teleseismic data

An examination of the responses from both simple and complicated models with and without low velocity sedimentary layers is necessary to determine the effects of the sedimentary layer, the relationship between the frequency response and the structure and the effectiveness of the propagator technique. For each structural model that is tested, two models are produced, one with a sedimentary basin, and one without the basin. To more accurately reflect the frequencies available in actual teleseismic analysis, the synthetic data in this section have also been low-pass filtered at 1.5 Hz as the last step prior to the production of plots. A ray parameter of 0.004 s/km was used – making the wave near vertical. A sampling interval of 0.025s was chosen to produce the synthetic data.

The first modelled structure is a simple 3-layer representation of the receiver side structure of the earth (Table 4.1). For this model, without basin means layer 1 is removed, and replaced with standard crust, i.e. the properties of layer 2. Model 1A is where the basin is removed and is a two-layer model, while Model 1B is with the basin present and is 3 layers.

Table 4.1 Parameters of Model 1B. The first layer is sedimentary, the second layer is the rest of the earth's crust and the third layer is the half space (mantle).

Layer	1 (sedimentary)	2	3
S Velocity (m/s)	1400	3500	4400
P Velocity (m/s)	2400	6250	8100
Density (kg/m^3)	2400	2600	3300
Depth to bottom of layer (m)	2000	35000	

The response calculated without the sedimentary layer (1A), with just the crust and the mantle present, produces the response displayed in Figure 4.1. Zero time represents the point at which the wavefront reaches the model base. The vertical response of the model 1A is the simplest; the original P arrival is prominent, with a Moho multiple (PpmP) the only significant other arrival. The radial response includes the P arrival, the Moho P multiples as well as a Moho P-Sv conversion (PmS) and Sv-polarized multiples (eg. PpmS and PsmS).

Figure 4.1. P-SV synthetic data produced using a simple 3-layer model 1B (Table 4.1) with a basin and 1A without the basin. Despite the simplicity of the model, the radial component with the sedimentary layer becomes relatively complicated. Low pass filtered at 1.5 Hz. The plot has been normalized such that the maximum value is 1.

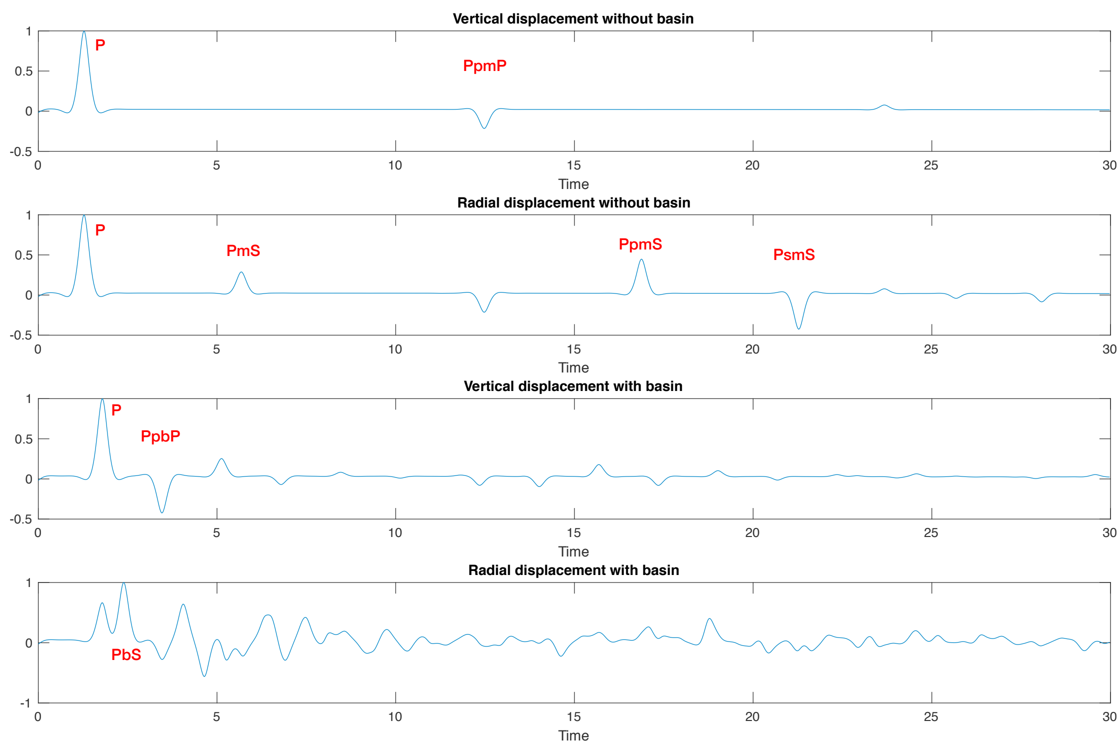

When a sedimentary layer is introduced, a new P-Sv phase is produced at the base of the sedimentary layer (Figure 4.1). The original P pulse is also delayed because of the slower material in the basin. The sedimentary layer generates new P multiples. The 3-layer model, with a sedimentary layer, produces a radial response that includes more arrivals than the other responses. The additional arrivals in the radial direction are generated from the P-Sv conversions at the Moho, and more significantly, at the base of the sedimentary layer. The response appears dominated by these P-Sv basin multiples or reverberations. Arrivals in the radial 2-layer response are also present in the radial 3-layer response (at 6, 12.5 and 17 s in the 2-layer response, slightly later in time with the sedimentary layer due to the lower velocities introduced), but sedimentary basin reverberations (14.8, 18.3 s) are much stronger. The PPmS and PSmS arrivals (which are in both radial functions) are important phase arrivals for calculating crustal properties. Standard methods, such as HK stacking, may have trouble picking these arrivals in an area with thick sediments as the response is dominated by basin reverberations (Yeck et al., 2013).

The frequency of the responses from models 1A and 1B (Figure 4.2 and 4.3) indicates a strong frequency dependence on the model, due to the large differences between them. These plots are not low-pass filtered unlike the time series. In Figure 4.2 the separation of the repeating peak frequency is dependent on the travel time for the Moho multiples. In Figure 4.3 the frequency content is impacted by the sedimentary layer. For the radial component, the frequency response peaks are separated by intervals of 0.37 Hz. With a velocity of 1400 m/s and a sedimentary thickness of 2000 m, a frequency of 0.7 Hz (twice the peak interval) is equivalent to the 2z reverberation within the basin. The oscillation amplitude also has a much larger range in Figure 4.3 than in 4.2. These relationships indicate that the response will be dominated by basin reverberations corresponding to the basin thickness.

The last panels in 4.2 and 4.3 indicate the ratio(radial/vertical) of the previous two panels. The ratio indicates what a receiver function will be, due to the R/Z deconvolution. The ratio shown in third panel of Figure 4.2 is relatively flat, while low value in the ratio shown in Figure 4.3 contains peaks where a maximum in the radial response value is by the low value in the vertical response.

Figure 4.2. The positive frequencies of the radial and vertical response and their spectral division, shown as the magnitude of the complex spectrum. Synthetic data were produced with Model 1A where no sedimentary basin is present. This data has not been low pass filtered.

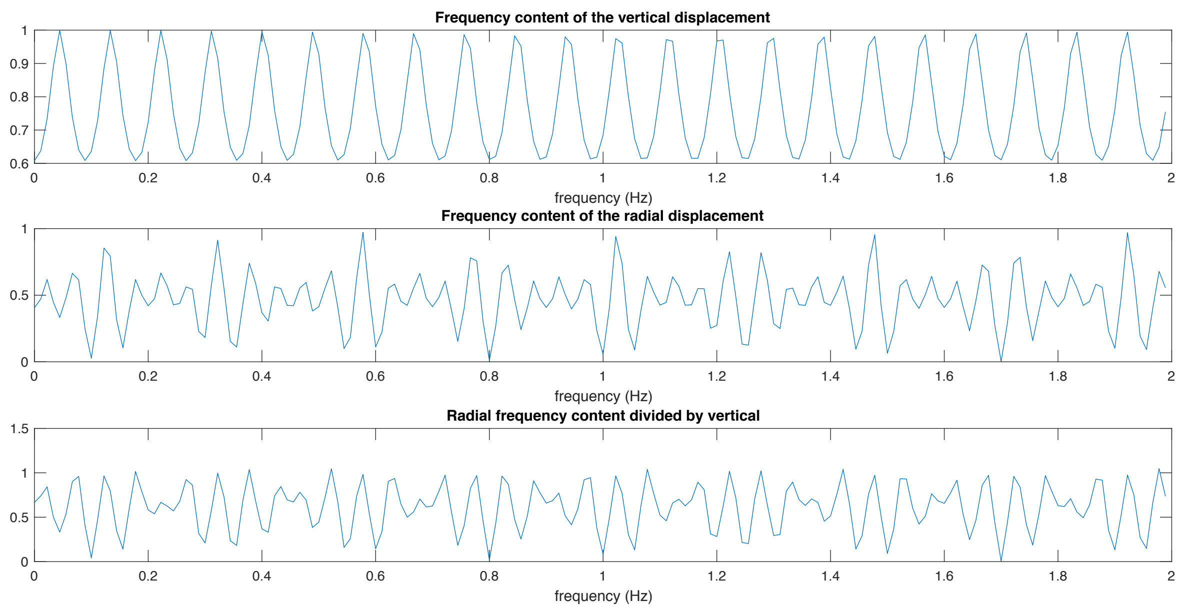

Figure 4.3. The positive frequency content of radial and vertical response and their spectral division, shown as the magnitude of the complex spectrum. Synthetic data were produced with Model 1B.

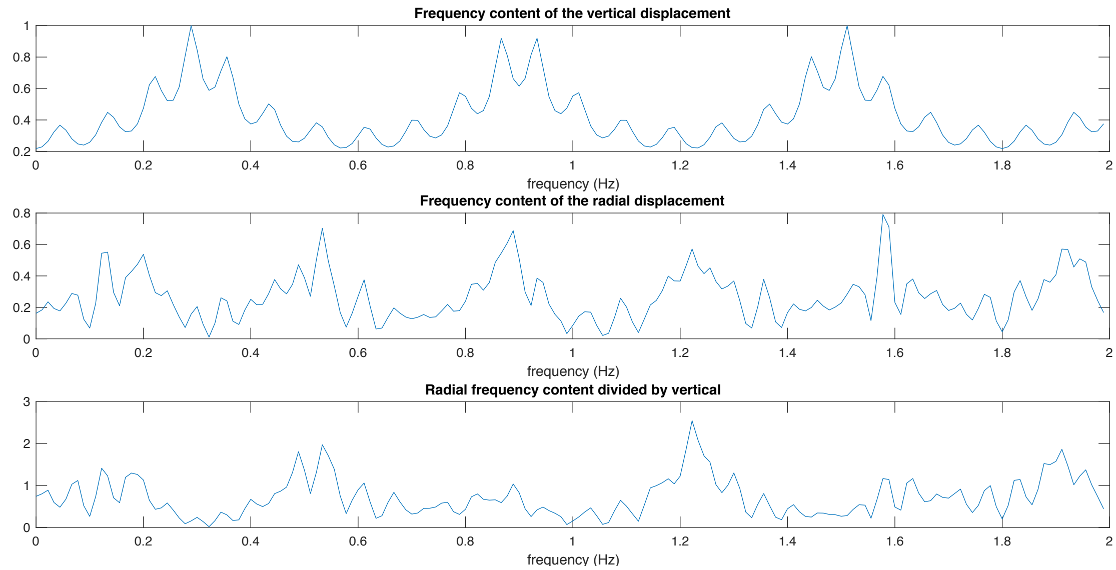

Model 2B (Table 4.2) represents a receiver side structure with 5 layers. The time series generated from this model is displayed in Figure 4.4. Comparing Figure 4.2 and 4.4, the response from the more complicated 5-layer model appears to be quite similar to the 3-layer model. Interestingly, in the 5-layer radial response the first arrival is now larger than the P-Sv basin conversion shortly after, unlike in Figure 4.2. Model 2 is more realistic than Model 1, as the sedimentary to basement contrast in Model 1 is unrealistically strong and was chosen to accentuate basinal effects. Once again, important phase arrivals that are clear in the radial component calculated without the basin are hard to discern in the radial component calculated with the basin. Arrivals are also delayed and response magnitude is lost (when compared to arrivals without the basin) as in the previous model response. Due to the increase in interfaces in the 5-layer model, there are more P-Sv conversions and thus the response is more cluttered. PpPs and PpSs+PsPs arrivals are no longer the strongest late phase arrivals, so accurately determining crustal properties using receiver function methods would be more challenging on this data than if there were no basin present (Yeck *et al*., 2013; Tao *et al.,* 2014; Zhu and Kanamori, 2000). The arrival visible in Figure 4.4 B at 24.8 s is completely masked by a basin reverberation at a similar time in the 5-layer model in Figure 4.4 D.

Table 4.2. Parameters of Model 2. The first two layers are sedimentary and relatively slow while the 3 remaining layers are a simple crustal model.

	Sedimentary Basin		Crystalline Basement		Mantle
Layer	1	2	3	4	5
S Velocity (m/s)	1400	1650	3000	3500	4400
P Velocity (m/s)	2400	2700	6250	7200	8100
Density (kg/m³)	2400	2450	2600	2800	3300
Depth to bottom of layer (m)	1000	2000	35000	45000	

Figure 4.4. P-SV response from the 5-layer Model 2 with the sedimentary layers and a 3-layer where the first two layers have been omitted. Low pass filtered at 1.5 Hz. Time begins with the plane wave entering the crust from the mantle, first arrivals in C & D are delayed by the sedimentary basin.

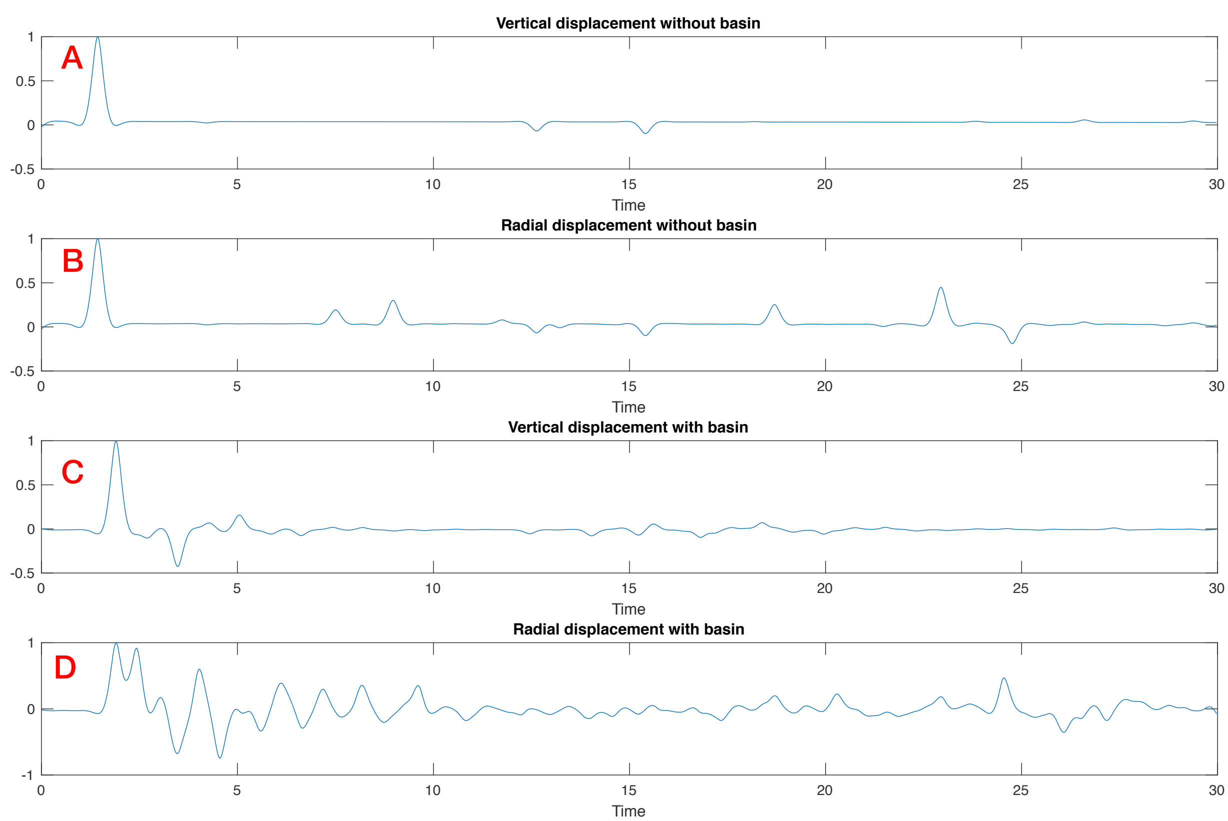

Although most analysis of teleseismic data is done using the radial and transverse components, it is worthwhile to determine if the layer-strip technique could be useful in removing reverberations in the horizontal component of the shear energy. The first step is to test the effects of sedimentary basins on the SH component of wave energy. This was done to determine if SH reverberations are expected to result from a shear modulus contrast associated with a sedimentary basin. The SH response of Model 3 in Table 4.3 (modified from Model 1) is shown in Figure 4.5. No substantial reverberations were detectable. This result indicates that basin reverberations are not going to be a problem when analyzing the transverse component of the response.

Table 4.3 Parameters of Model 3. This model is designed to generate synthetic SH surface displacement (horizontal shear movement). The first layer is sedimentary, the second layer is the rest of earth's crust and the third layer is the half space or mantle.

Layer	1 (sedimentary)	2	3
S Velocity (m/s)	1400	3500	3900
Shear Modulus (GPa)	22	44	75
Depth to bottom of layer (m)	2000	35000	

Figure 4.5. SH response from the 3-layer generated using Model 3. The resulting data was low pass filtered at 1.5 Hz.

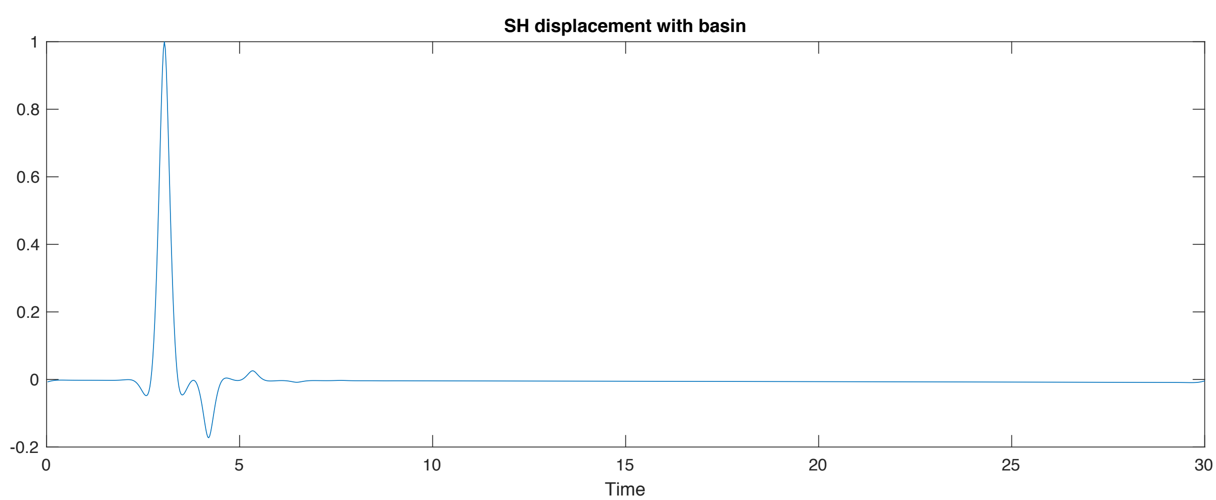

4.3 Testing the layer-strip filter

Using synthetic impulse responses, inter-model transfer functions may be generated (equations 3.13 and 3.14). The layer-stripping transfer function can first be applied to synthetic data to test the methodology. These transfer functions are convolved with synthetic data to act as an acausal layer-stripping filter. Acausal in this case means the output is the result of past as well as future inputs, which is possible in post processing. Testing the layer-strip filter will begin with synthetic data because we can compare the resulting layer-stripped output with the ideal output (the data produced in the absence of the sedimentary layer). This approach is used to examine the effectiveness of the layer-strip while varying the accuracy of the models used to produce the transfer functions. As this section will show, when imperfect layer-strip models are used, high frequency noise is mapped into the resulting layer-stripped function. This noise is dominantly at frequencies usually omitted from receiver function analysis (greater than 1.5 Hz). To more accurately reflect real world receiver function analysis, and to assess the effectiveness of the filter, the synthetic data have also been low pass filtered to 1.5 Hz. A δ of 0.0001 was used in layer-stripping.

The first test is produced using Model 1, where Model 1 is used to generate both the synthetic receiver side response data and the transfer function that is applied to it (Figure 4.6). As expected, with a perfect layer-strip model, the effects of the sedimentary basin are completely removed and the layer-stripped data are identical to the data produced with the sedimentary layer omitted. This indicates that the methodology works perfectly under ideal conditions, but the result is not indicative of the effectiveness of the method under realistic conditions. The δ appears to have had no effect on the result of the layer-strip.

Figure 4.6. A & B) P-SV response from the 3-layer Model 1 with the sedimentary layers. C & D) 2-layer response where the first layer (sedimentary) has been omitted. E & F) layer stripped components, filtered using the same Model 1 used to generate the data. All plots are low pass filtered at 1.5 Hz.

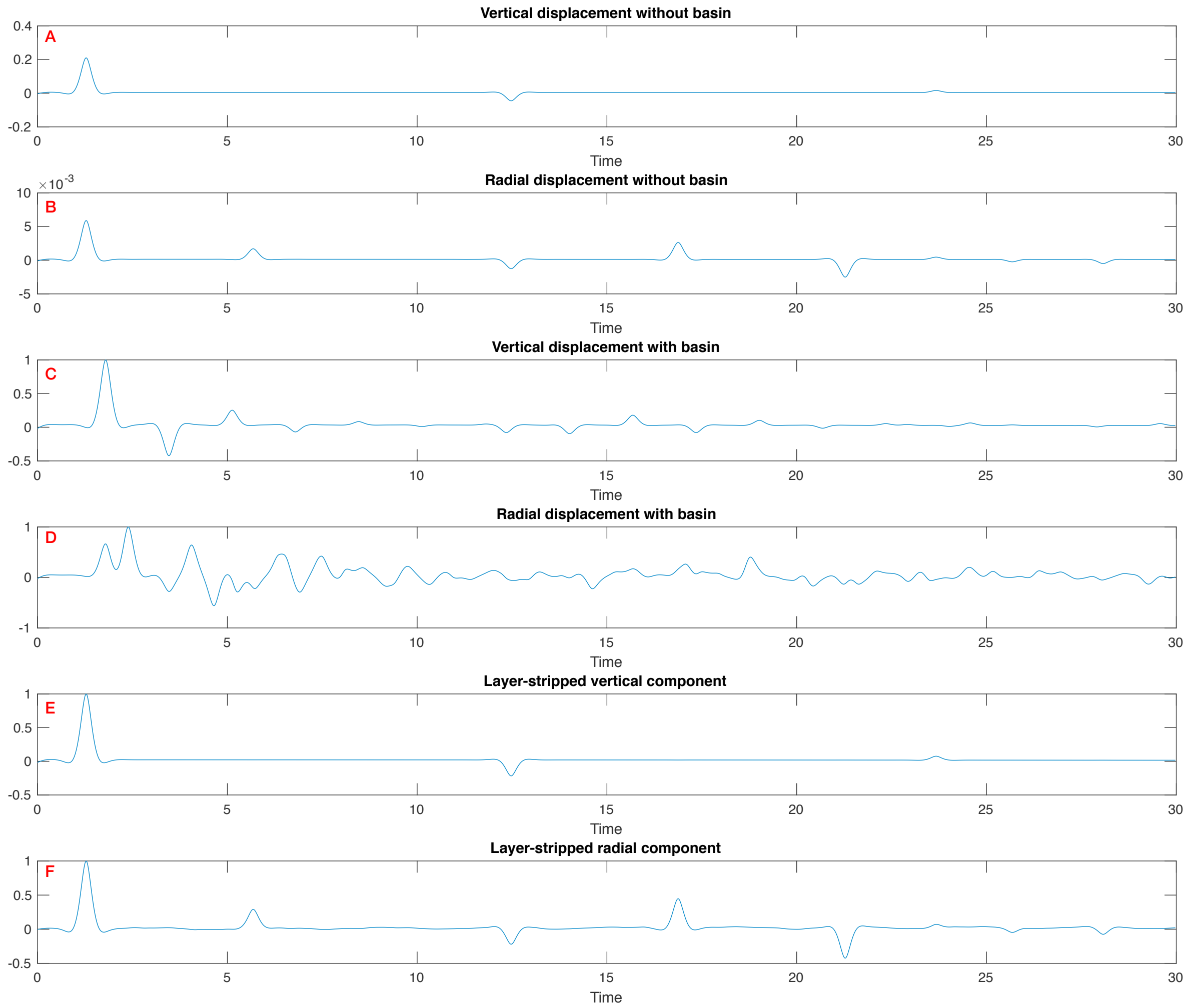

In order to test the effectiveness of the filter with progressively poorer models, a small change was made to the sedimentary thickness in the model used to calculate the transfer function. Instead of 2000 m used in Model 1, a 1990 m thick sedimentary layer was used to produce the layer-strip in Figure 4.7. The resulting layer-stripped data is nearly identical to the original basin omitted data. This indicates that the layer-strip is stable enough to effectively remove the basin reverberations and other basin effects when the model is close to perfect. The largest discrepancy between panels A,B and E,F in Figure 4.7

is the 0-time amplitude change in the layer-stripped radial component. Generally, there is a subtle linear trend added to the layer stripped radial component. This may be a wrap-around effect generated from inadequate zero padding in the circular convolution. It may also be generated from spectral leakage due to a non-zero DC component.

Figure 4.7. A & B) P-SV response from Model 1 with the sedimentary layers. C & D) 2-layer response where the first layer (sedimentary) has been omitted. E & F) layer-stripped components, filtered using the same Model 1 was used to generate the data, but with a layer 1 thickness of 1990 m. Results were low-pass filtered at 1.5 Hz. A through D are the same as in figure 4.6 and are included for reference.

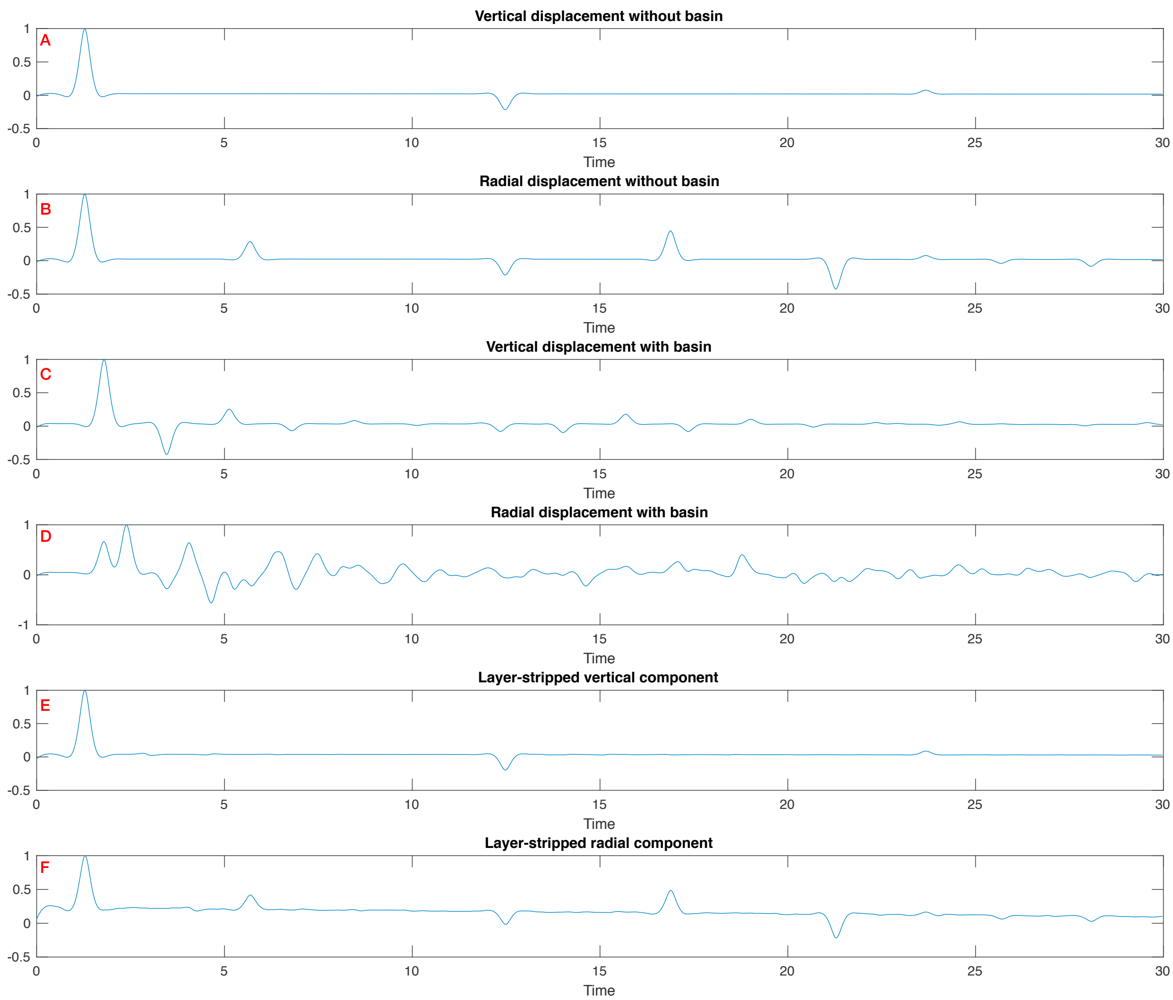

It is expected that a model of a sedimentary basin will not be accurate within 10 m unless the receiver location is completely resolved by drilling and core analysis, or that the basin is completely homogeneous laterally and drilling is completed elsewhere. Therefore, further offset between models is called for. Figure 4.8 is created using a layer-strip generated from Model 4 (table 4.4), where the sedimentary layer is reduced 100 m to 1900 m. The results indicate that the differences between the generating model and the filtering model produce an imperfect layer-strip. Noise is mapped into both layer-stripped functions, and the radial component has not been filtered as effectively as with better models. The layer-stripped vertical component is filtered fairly effectively, with the response dominated by the response with no basin present. Some reverberation signal remains, but all three of the arrivals in the first plot of Figure 4.8 are clear in the layer-stripped version. The layer-stripped radial component is not as similar to its ideal counterpart (the second plot in Figure 4.8). The early times of the layer-stripped radial component are effectively filtered, as the first arrival is no longer dominated by the basin reverberation, and it is moved backwards in time, indicating basin effects have been removed. Arrivals at 6, 12.5, 17 and 22 s in the layer-stripped radial function appear large in amplitude compared with the non-layer-stripped data. Arrivals beyond 22 s are dominated by reverberations and potentially noise mapped into the function from layer-stripping. Although the layer-strip is still effective, the noise mapped into the output of the radial component is substantial. Once again, a negative shift throughout the layer-stripped radial component indicates a DC component effect.

Figure 4.8. A & B) P-SV response from Model 1 with the sedimentary layers. C & D) 2-layer response where the first layer (sedimentary) has been omitted. E & F) layer-stripped components, filtered using the same Model 1 used to generate the data, but with a layer 1 thickness of 1900 m. Results are low pass filtered at 1.5 Hz. A through D are the same as in figure 4.6 and are included for reference.

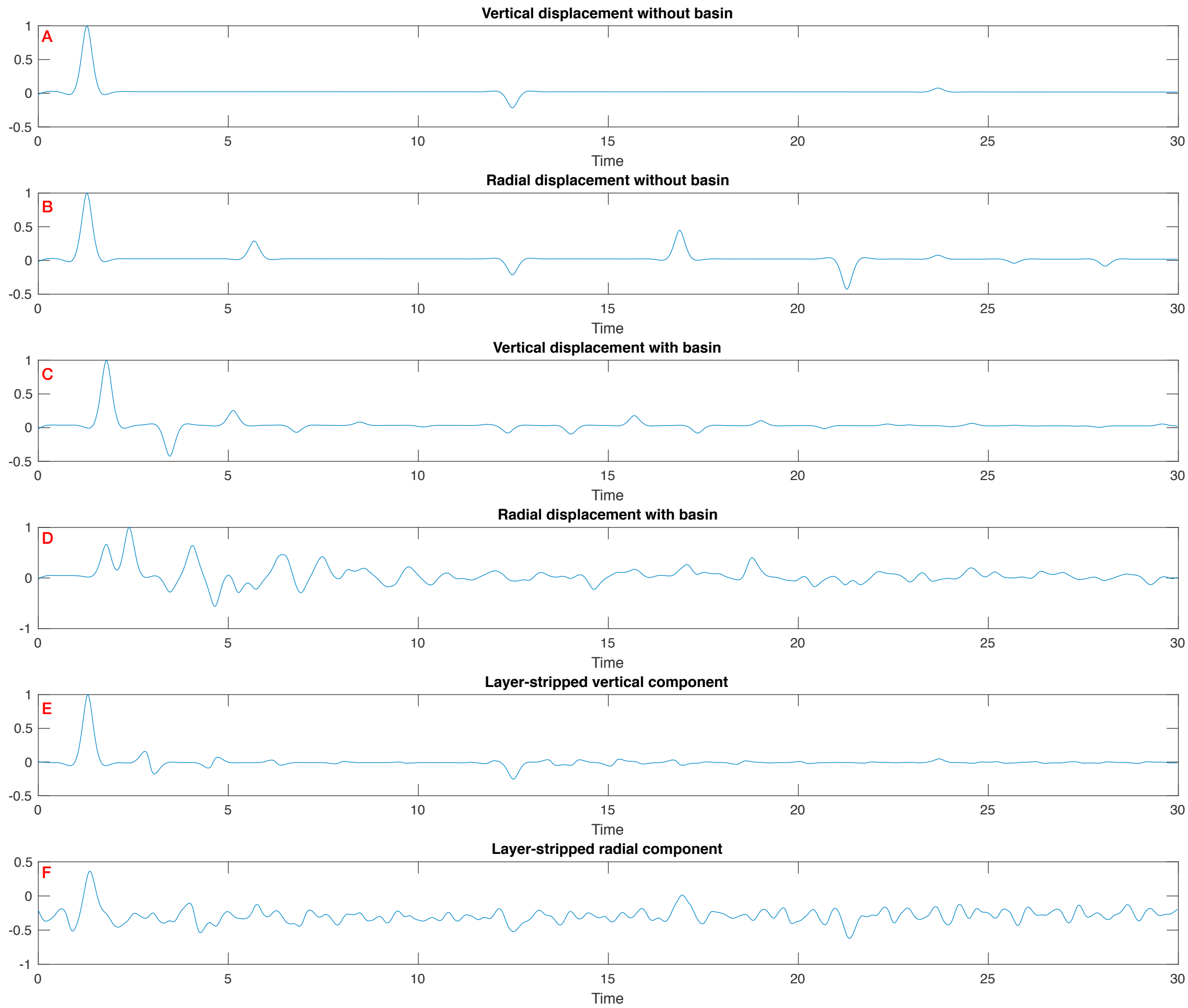

The next test is completed using a layer-strip model defined in Table 4.4 and the results are displayed in Figure 4.9. Once again, the data in panels A through D of Figure 4.9 are generated using Model 1. Each crustal parameter is changed to determine the effects of a thoroughly imperfect model. The changes to Model 1 are determined by a random number generator combined with rounding in a range of 50-300 (for velocity, density and depth). Because the randomization led to a slower sedimentary layer, combined with the reduced thickness of the sedimentary layer, the effects of the model offset may have been partially cancelled as arrival times will change less than if one parameter only was increased. Regardless of this effect, the results indicate that the layer-strip is stable enough to effectively filter the data with a more imperfect model, at least with respect to the deeper crust. The results of this test indicate that the sedimentary layer parameters are most important in determining the effectiveness of the filter. When the thickness of the sedimentary layer is only changed by 100 m, the results shown in Figure 4.8 are poorer than those shown in Figure 4.9 when the values of the deeper crust were altered by a greater amount. The impact to the layer-strip in Figure 4.9 is likely due to the slower sedimentary layer used for, but the results indicate that the filter is moderately stable to changes in deeper layers. Once again, arrivals later than 22 s are obscured by basin reverberations.

Table 4.4. Parameters of Model 4. The first layer is sedimentary, the second layer represents the rest of earth's crust and the third layer is the half space or mantle.

Layer	1 (sedimentary)	2	3
S Velocity (m/s)	1350	3600	4400
P Velocity (m/s)	2300	6450	8100
Density (kg/m^3)	2500	2650	3400
Depth to bottom of layer (m)	1900	35300	

Figure 4.9. A & B) P-SV response from the 3-layer Model 1 with the sedimentary layers. C & D) 2-layer response where the first layer (sedimentary) has been omitted. E & F) layer stripped components, filtered using Model 4 to generate the filter. Low pass filtered at 1.5 Hz. Panels A through D are the same as in figure 4.6 and are included for reference.

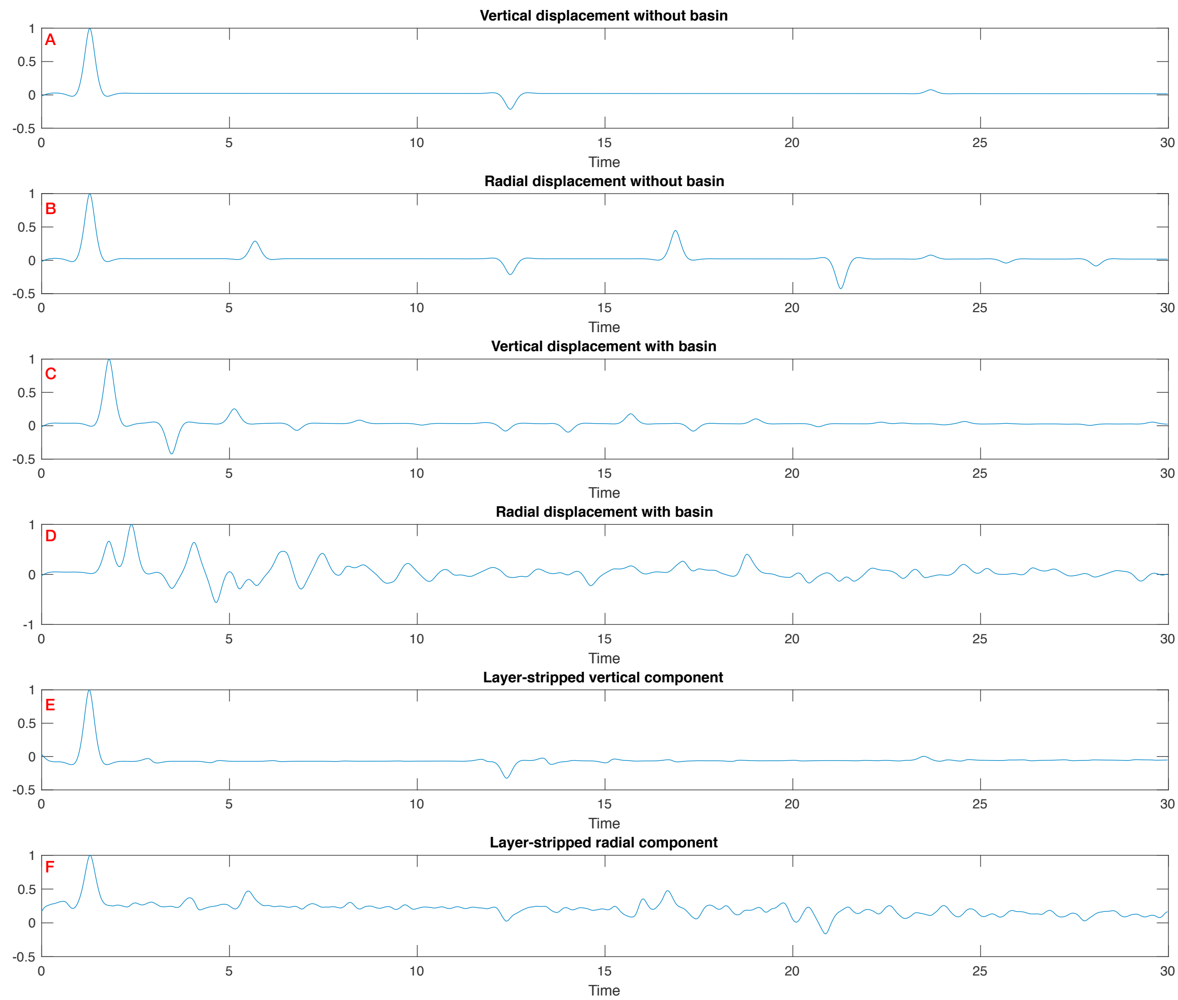

The next layer-strip test is completed on data generated with Model 5 from Table 4.5 and the transfer function/layer-strip filter was generated using Model 4. The test assesses the ability of a filter generated with a 1-layer sedimentary basin model to correct data produced with a 2-layer sedimentary basin. The results are displayed in Figure 4.10. The layer-strip is effective on the vertical component, as the reverberation noise is reduced moderately and the arrival at 23 s is improved when compared with the third plot in Figure

4.10. The radial component, however, has not been filtered effectively. The early time response is still dominated by noise and the 22 s arrival appears to be weaker or misplaced in the filtered data. Arrivals at 12.5 and 17 s located in the "without basin" data do appear in the filtered data, indicating that this layer-strip has made some improvement. This result indicates that a simplified model performing the layer-strip can be ineffective when there is a strong impedance contrast within the basin. In cases where the sedimentary basin is known to be multi-layered, this layering must be included in the model.

A second layer-strip was completed on data from Model 5 using Model 6 from Table 4.6. This was done to compare the earlier results in Figure 4.10 to a model with a 2-layer sedimentary basin. Model 6 was designed to have a similar value offsets compared with Model 5 as in the previous test. This layer-strip is displayed in Figure 4.11. The 2-layer basin model filter produces a substantially improved output compared to a 1-layered sedimentary model. Both the vertical and radial components were improved over the earlier test. The layer-strip was particularly effective at earlier times, with the 6 s arrival in Figure 4.11 F greatly improved compared to Figure 4.10 F. This result indicates that the internal structure of the sedimentary basin is important in generating an effective layer-strip filter, not just the average parameters and thickness of the basin. The later time arrivals are once again masked by noise. The layer-stripped radial component in Figure 4.11 is negative throughout an artifact that is seen in earlier layer-stripped radial responses.

Table 4.5. Parameters of Model 5. The first two layers are sedimentary and relatively slow while the 2 remaining layers are basement and uppermost mantle.

Layer	1	2	3	4
S Velocity (m/s)	1400	1700	3500	4400
P Velocity (m/s)	2400	2800	6250	8100
Density (kg/m^3)	2400	2450	2600	3300
Depth to bottom of layer (m)	1000	2000	35000	

Figure 4.10. A & B) P-SV response from Model 5 with the sedimentary layers. B & C) 2-layer response where the first two layers (sedimentary) have been omitted. E & F) layer stripped components, filtered using Model 4 to generate the filter. Low pass filtered at 1.5 Hz.

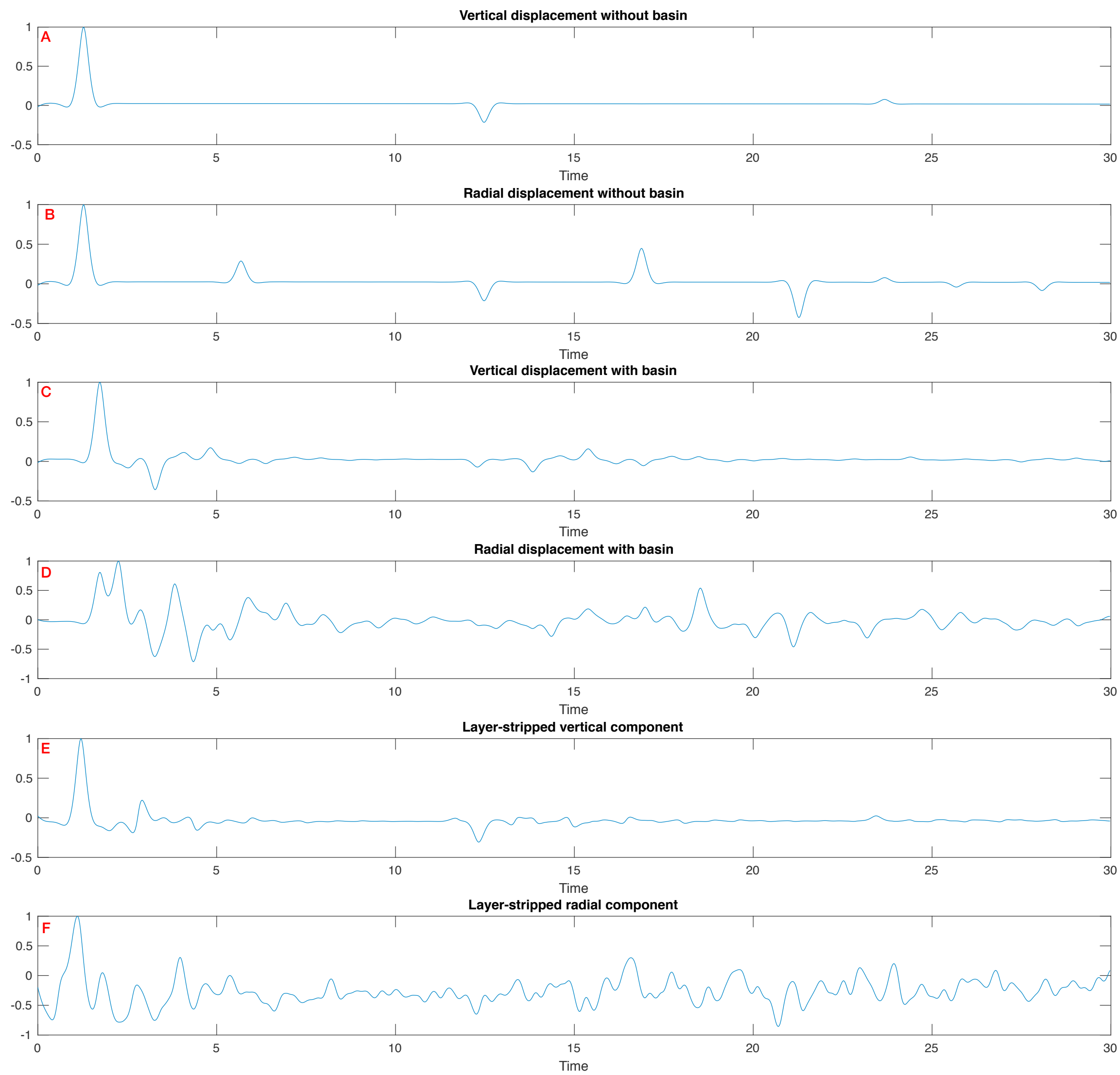

Table 4.6. Parameters of Model 6. The first two layers are sedimentary and relatively slow while the 2 remaining layers are basement and uppermost mantle. Model 6 was used to layer-strip Model 5 (Table 4.5).

Layer	1	2	3	4
S Velocity (m/s)	1350	1750	3600	4400
P Velocity (m/s)	2300	2650	6350	8100
Density (kg/m³)	2350	2500	2650	3400
Depth to bottom of layer (m)	900	1900	35300	

Figure 4.11. A & B) 2-layer response where the first two layers (sedimentary) have been omitted. C & D) P-SV response from the 4-layer Model 5 with the sedimentary layers. E & F) Layer stripped components, filtered using Model 6 to generate the filter. Low pass filtered at 1.5 Hz.

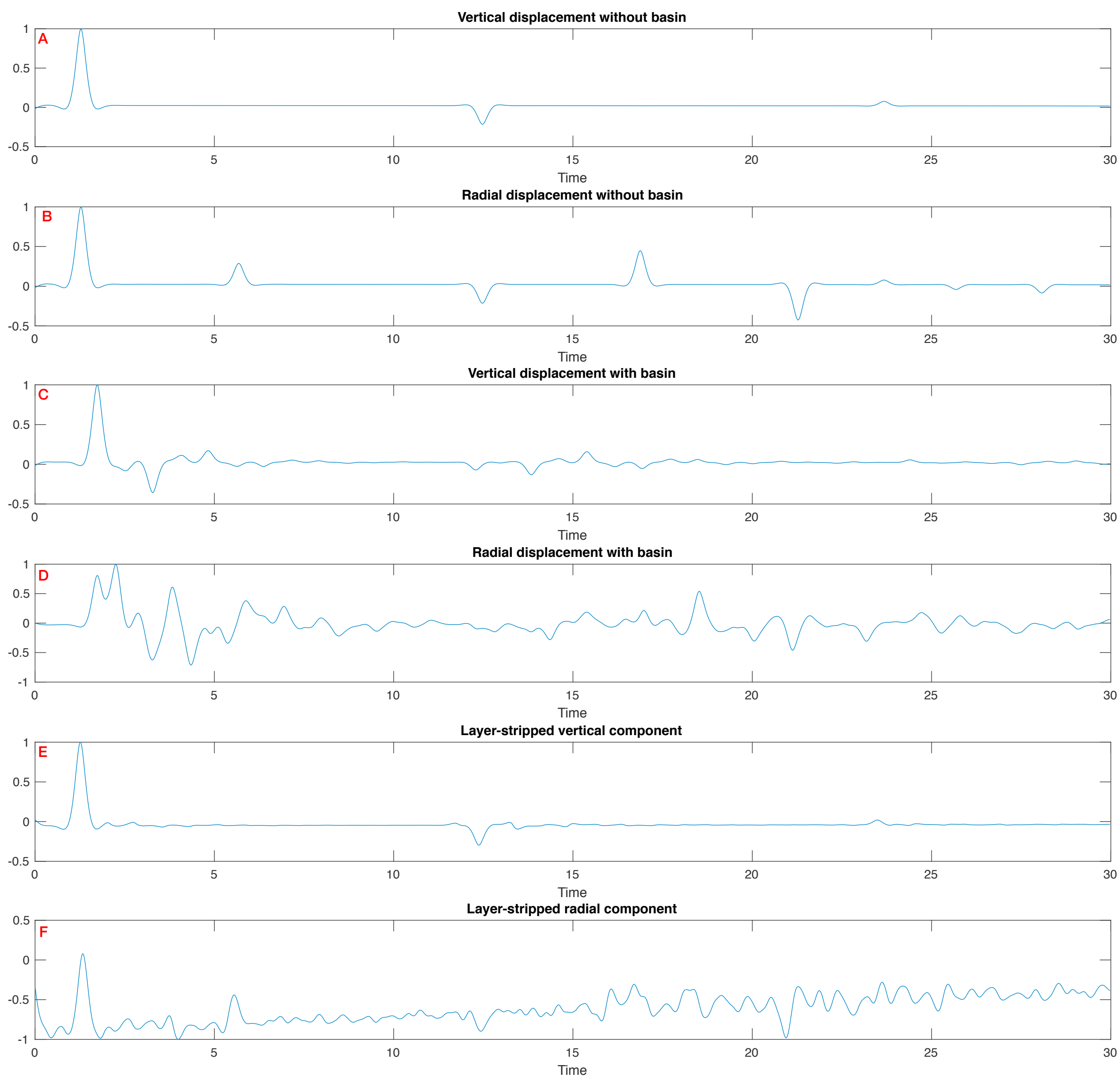

Analysing the transfer function that acts as the layer-strip filter indicates why noise is being mapped into the radial layer-stripped component (Figure 4.12). The frequency content of the radial component transfer function contains large values in tight frequency bands. Some frequencies outside of the windowed 1.5 Hz range go above an amplitude of 15. Failing to filter out these frequencies would make the response more cluttered, but was done so as it is of typical teleseismic processing work and allows for better signal comparison. It is clear that the radial transfer function is more complicated than the calculated vertical transfer function. It is also clear that an imperfect model will map noise into the data, and that this effect is stronger in the radial component. This is especially true at later times where the response is based on longer travel times through incorrect model parameters. It will be more effective to apply the transfer functions separately to the vertical and radial components, instead of the calculated receiver function. While a transfer function for the receiver function could be produced, computing a receiver function maps noise into the data. The transfer function is likely to be more effective at filtering before that noise is mapped. For example, the vertical component can be layer-stripped more effectively than the receiver function, as the radial component will contain much of the noise.

Figure 4.12. Frequency Spectra of transfer functions generated from Model 4 (Table 4.4).

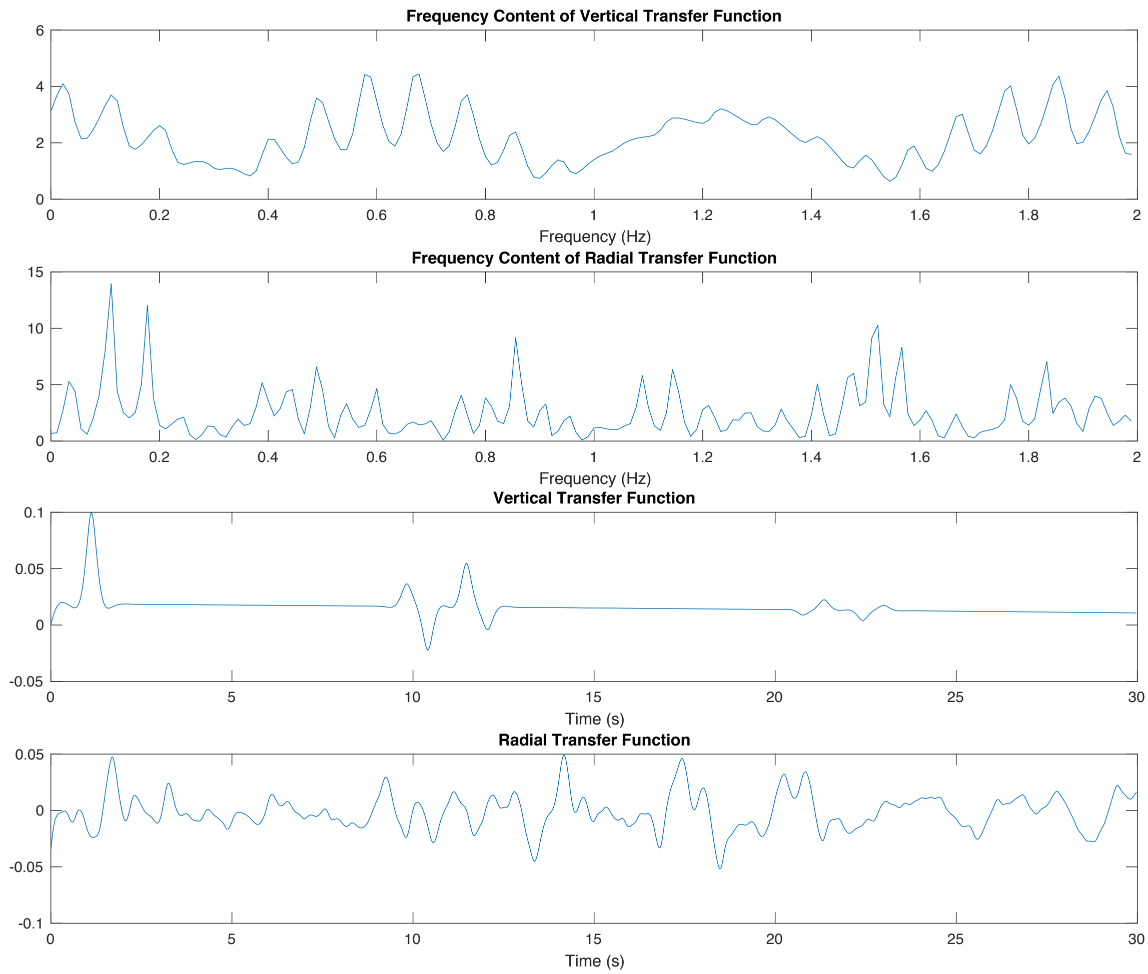

The results in this chapter indicate that the propagator method is effective at generating reverberations and demonstrating the difference between areas with and without sedimentary basins. The modelled synthetic data indicate that even a simple receiver side model produces a cluttered radial response when thick sedimentary layers are present. The reverberations present mask important later arrivals, and the early time radial response is dominated by the first basin reverberation.

The layer-strip tests on synthetic data were effective when the model used for the layer-strip is similar to the model that generates the data. The method is stable enough to effectively filter data when small deviations between models are made. With differences to the layer-strip sedimentary thickness on the order of 100 m, the layer-stripped function contains noise that masks later, weaker arrivals. A 1-layered sedimentary model for the transfer function is not effective in filtering a 2-layered sedimentary system. This indicates that an accurate model must exist in order to effectively layer-strip teleseismic data.

Chapter 5. Data Collection and Pre-processing Methods

5.1 Station selection

Before the layer-strip filter can be tested on real-world data, a data set must be chosen, obtained and pre-processed. The data set must also pass through a quality control step to ensure only properly captured events are included. The criteria for choosing which stations to use included location, access to velocity models of the region and ease of retrieval. The locations must be in a sedimentary basin thick enough to produce reverberations and a relatively strong velocity contrast from basin to basement rock must be observed. For this research two separate data sets are used. The first is collected from a single station located in the Western Canadian Sedimentary Basin, and the second data set is obtained from a group of stations transecting the Williston Basin.

The first station selected for analyzing the effectiveness of the layer-strip method is EDM in Edmonton. This station was chosen for three reasons, the first being that it is located on thick sedimentary rocks, which makes it a useful candidate for this research (Cassidy, 1995; Zelt and Ellis, 1989). Additionally, the station produces complex receiver functions, cluttered with reverberations (Cassidy, 1995). The final reason EDM was chosen is that velocity models exist of the Peace River Arch region of the Western Canadian Sedimentary Basin due to oil and gas exploration and reflection surveys completed nearby (Cassidy, 1995; Zelt and Ellis, 1989). As an area of well-known structure, the results from the EDM station in the Western Canadian Sedimentary Basin will be a useful starting point to examine for filtering teleseismic data from thick sedimentary basins. The data collected at this station are publicly available from the Geological Survey of Canada (GSC).

A second data set was needed to ensure that the layer-strip filter works under general sedimentary basin conditions, and not just in the Western Canadian Sedimentary Basin. Importantly, the second data set also tests the effectiveness where the structure is less well-known and allows for the testing of a range of basin thicknesses and multiple structural models. This test will help determine when it is appropriate to apply the methodology and under what conditions it fails to be effective. For this purpose, stations in the Williston Basin from the Earthscope Transportable Array (TA) in the United States of America were chosen. This area was chosen as station coverage allows for testing a wide range of basin thicknesses across the basin and a previous study provides structural velocity models (Frederiksen and Delaney, 2015). The TA data also provides an opportunity to test whether basin velocity models derived from teleseismic data produce accurate enough information to correct receiver functions. This test will help determine if this approach works in the absence of independent datasets, such as deep controlled source seismic studies.

A collection of stations is selected to create an array that transects the Williston Basin. This transect will provide the opportunity to test how the filter works for a variety of sedimentary thicknesses and varying data quality. These stations are located in North Dakota, South Dakota, Minnesota and Iowa (Figure 1.1). The names for the transportable array stations used in this research are A25A, B26A, C27A, D28A, E30A, F32A, G34A, H35A, I36A, J38A. They are selected to follow a straight line across the Williston Basin.

5.2 Instrumentation

Station EDM in Edmonton is operated as part of the Canadian National Seismograph Network (Siddiqqi and Atkinson, 2002; Cassidy, 1995). Since 1991 the Canadian National Seismograph Network (CNSN) has deployed broadband three-component digital seismometers across Canada (Cassidy, 1995). Operated through the Geologic Survey of Canada (part of Natural Resources Canada), the network consists of roughly 100 high-gain seismometers (Natural Resources Canada, 2016). The data from these stations are collected in real time by processing centres in Ottawa, Ontario and the Pacific Geoscience Centre in Sidney, British Columbia and stored in the Standard for the Exchange of Earthquake Data (SEED) format. Station EDM began with a Guralp CMG3 seismometer (flat from 0.03 to 50 Hz) where the data were sampled at 40 Hz. This seismometer was used until 1998, when it was replaced with a Guralp CMG-3NSN. The data used in this study were recorded between 1994 and 2001. The Guralp GMG-3NSN seismometer was used at EDM through 2001.

Earthscope's TA began in 2004, where a set of 400 broadband seismometers were placed in the western United states and subsequently mobilized eastward collecting teleseismic and regional seismic data for roughly two years at each location (Williams *et al.*, 2010). With the end of the main TA program, station coverage has run through the entire United States, reaching the East Coast in 2012 and moving to Alaska in 2014.

One of the first phases of the TA included collecting teleseismic data over the Williston Basin. During this time, the TA used STS-2 Broadband Seismometer Sensors. These sensors record a flat response to velocity from 120 seconds to 10 Hz. The seismometers were in place between 2009-07-24 and 2011-07-22 for the western stations used in this research and 2010-09-20 until 2012-09-12 for more easterly stations.

5.3 Data acquisition

To acquire the data from EDM, first an event list was created using an ANSS Composite Catalog Search centered around the coordinates of EDM (NCEDC, 2016). Events were requested if their epicenter fell between 30 and 100° arc distance from the EDM station and the date fell within EDM's operating period. The distance requirements ensure that the earthquakes are in the teleseismic range. Events must also exceed magnitude 5. The magnitude requirement ensures the amplitude of arrivals is above background noise. This search produced a list of events that was used to request data from CNDC. The EDM data were acquired from Natural Resource Canada via an automated request sent to the CNSN. Canadian National Data Centre (CNDC) AutoDRM data request forms are completed using a shell script that converts lines from an event list into a series of emails sent to the CNDC. Each email prompts the upload of requested event data to an FTP server. The server is then accessed to download the data from as SEED files. These SEED files contain the time series data requested, and the metadata required for the file.

The data from the TA in the Dakotas were acquired by Dr. Andrew Frederiksen prior to the start of this research. Data for this portion of the project were recorded by Earthscope and obtained from the IRIS Data Management Centre (Frederiksen and Delaney, 2015). These data were provided via a hard drive in 2016.

5.4 Quality control and pre-processing

Before the layer-strip is applied, or the H-K stacking algorithm may be used, the data require quality control and pre-processing to increase the quality of the data set. For these purposes, MATLAB scripts and Shell Scripts were provided by Dr. Andrew Frederiksen prior to the start of this research.

A shell script was used to extract the SEED files and produce SAC files. Another script sorted the files into directories based on date and time. Preprocessing was applied to the data using a third Unix shell script. The pre-processing script adds three main elements to the header of the data: (1) date and time; (2) ray parameter and predicted P time; and (3) event location and back azimuth. The ray parameter and predicted P time were generated using the TauP Toolkit (Crotwell et al., 1999). The back azimuth was calculated as the angle from north at the receiver of a great circle that intersects the receiver and source locations. In addition to adding the previous elements, the pre-processing script trimmed each file to 180 seconds in length, beginning 30 seconds before the predicted P arrival. Finally, the script rotated the north-south and east-west components of the wave field into radial (in line with the back azimuth) and transverse (orthogonal to the back azimuth) components for use in generating receiver functions. This ensures the trace components are in terms of source direction instead of cardinal direction for mathematical simplicity.

The final result for each event at each station is an event.r, event.t, and event.z file. The transverse component (event.t) went unused because it consists of horizontally polarized S-waves. These S-waves are not converted from P-waves and therefore do not produce significant reverberations and are not used as part of this receiver function analysis (Section 4.2).

The processing steps taken between retrieving the data and obtaining the final output are outlined in Figure 5.1. Four final outputs are generated with this data flow for analysis: a set of layer-stripped receiver functions, a set of non-layer-stripped receiver functions, a layer-stripped HK Stack and a non-layer-stripped HK stack. A layer-stripped H-K stack and layer-stripped receiver functions can be produced for each structural model applied. Therefore, if two models were used there would be six outputs instead of four.

Figure 5.1. Pre-processing and filtering data flow chart. 4 final products are produced: receiver functions sorted by ray parameter with and without layer-strip applied and H-K stacks with and without layer-strip applied.

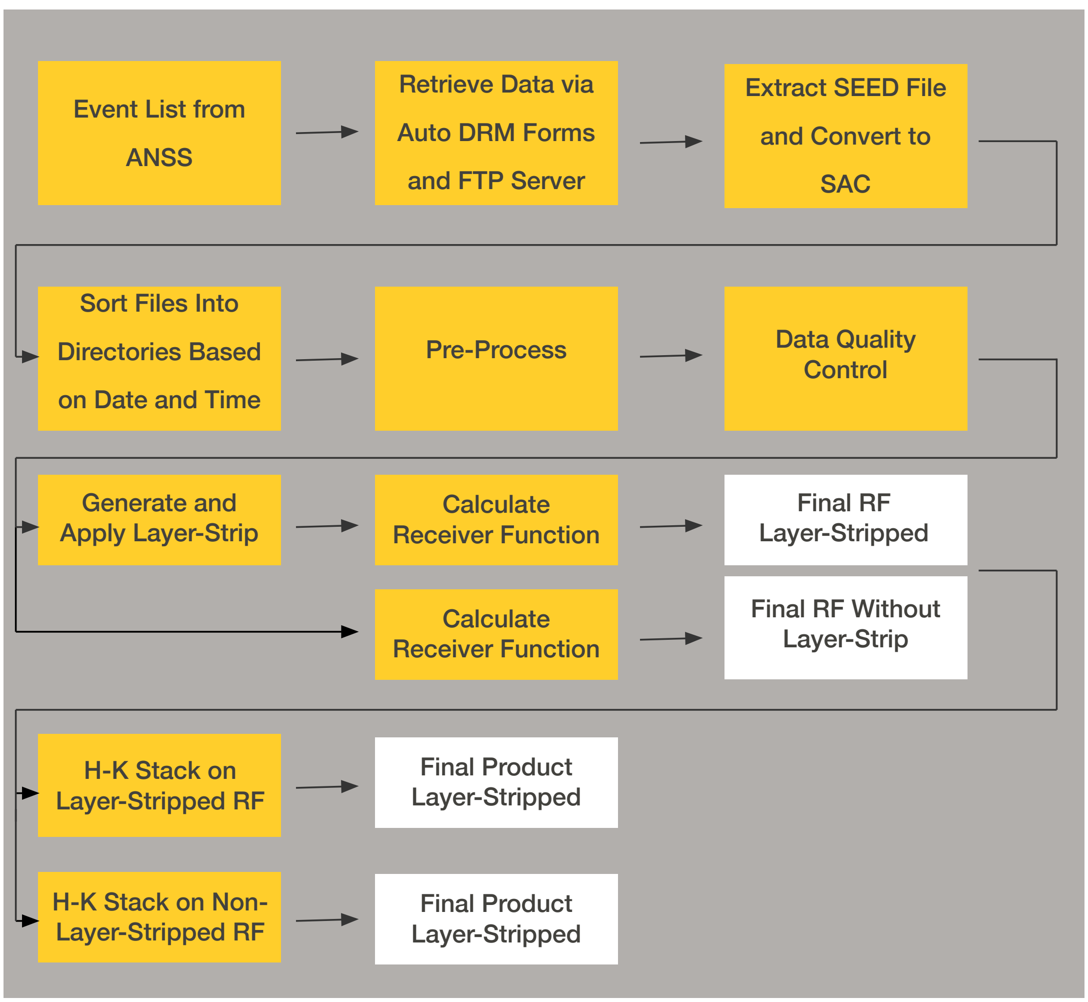

The final step to outline in Figure 5.1 is quality control. Quality control is completed on the data collected from EDM and stations in the Transportable Array to ensure that events recorded with poor signal to noise ratio were not used in analysis. Quality control was completed based on a receiver function as well as on the original radial and vertical traces for each event at the station. This assessment was done using a MATLAB script that displays all the events for a station as radial and vertical traces (using a passband filter between 0.3 and 3 Hz), and the corresponding receiver function (using a passband filter between 0.1 and 1 Hz). These ranges were chosen as the default from the program, it was found that altering the passband in the 1-3 Hz range did not have a large effect on quality control decisions.

The criteria for acceptable receiver functions was such that events with reverberations were not discarded. This ensures that events containing reverberations could be tested. Instead, events with high levels of noise prior to the first arrival (*i.e.* before 0s), where no signal should occur, were discarded. Events where first motion was not close to 0s were also discarded, as the first arrival should not be greatly delayed. An example of 12 traces considered during quality control are displayed in Figure 5.2. Traces that are dotted and colorless are toggled off for future use. They were deselected due to negative-time noise and lack of defined expected arriavals. 50% of the 797 events were retained for future use during quality control of the EDM data. An example of the receiver function quality control is displayed in Figure 5.3 where further traces were deselected due to poor signal to noise ratio.

Figure 5.2. A portion of the quality control performed on the first twelve events at EDM, where the radial and vertical components of each event are displayed in green and black, respectively. Traces default to an on positon but can be toggled off. The traces that did not pass quality standards are displayed as dotted lines.

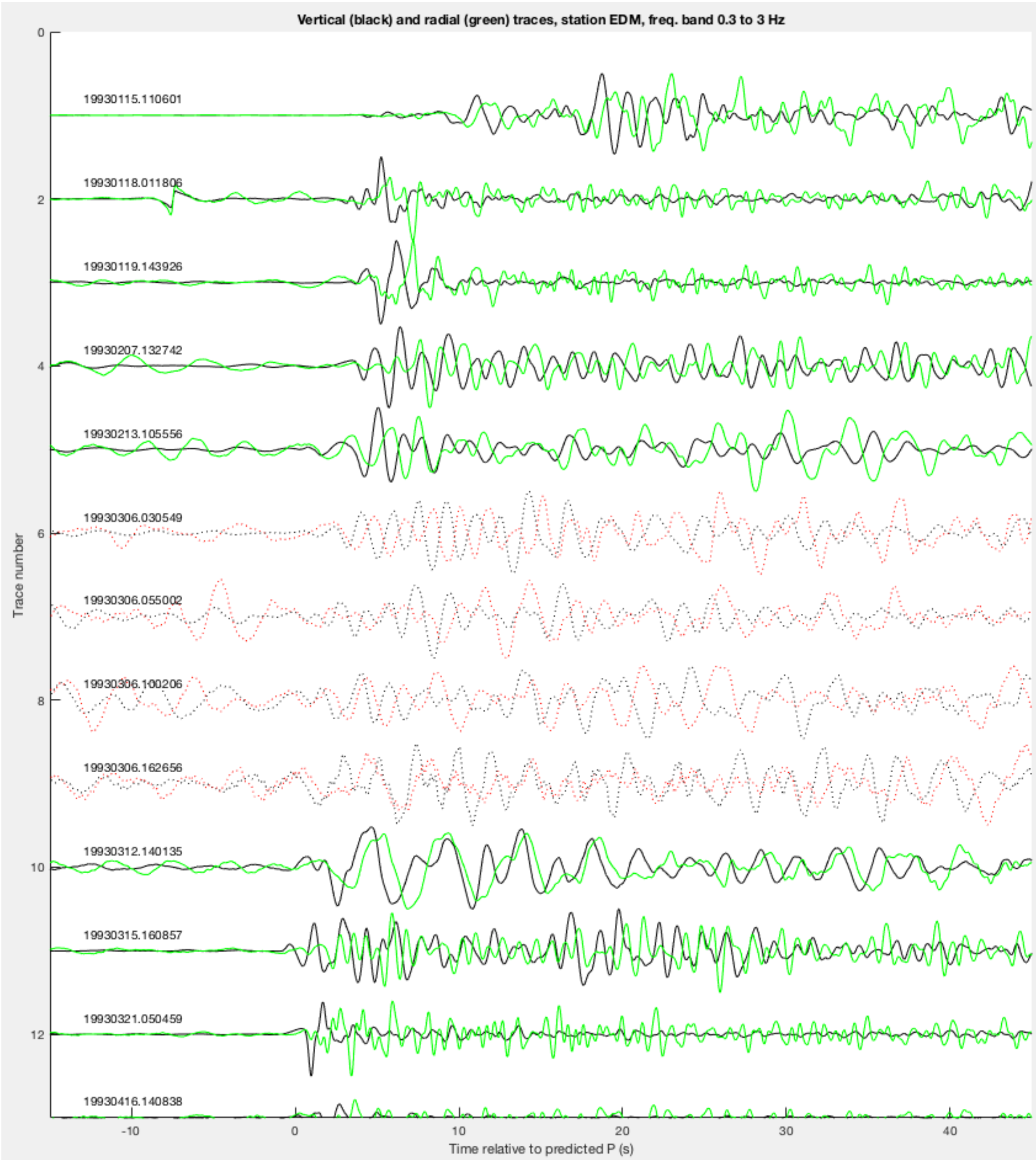

Figure 5.3. A portion of the quality control performed on twelve receiver functions from EDM. Traces default to an on position but can be toggled off. The traces that did not pass quality standards are displayed as dotted lines.

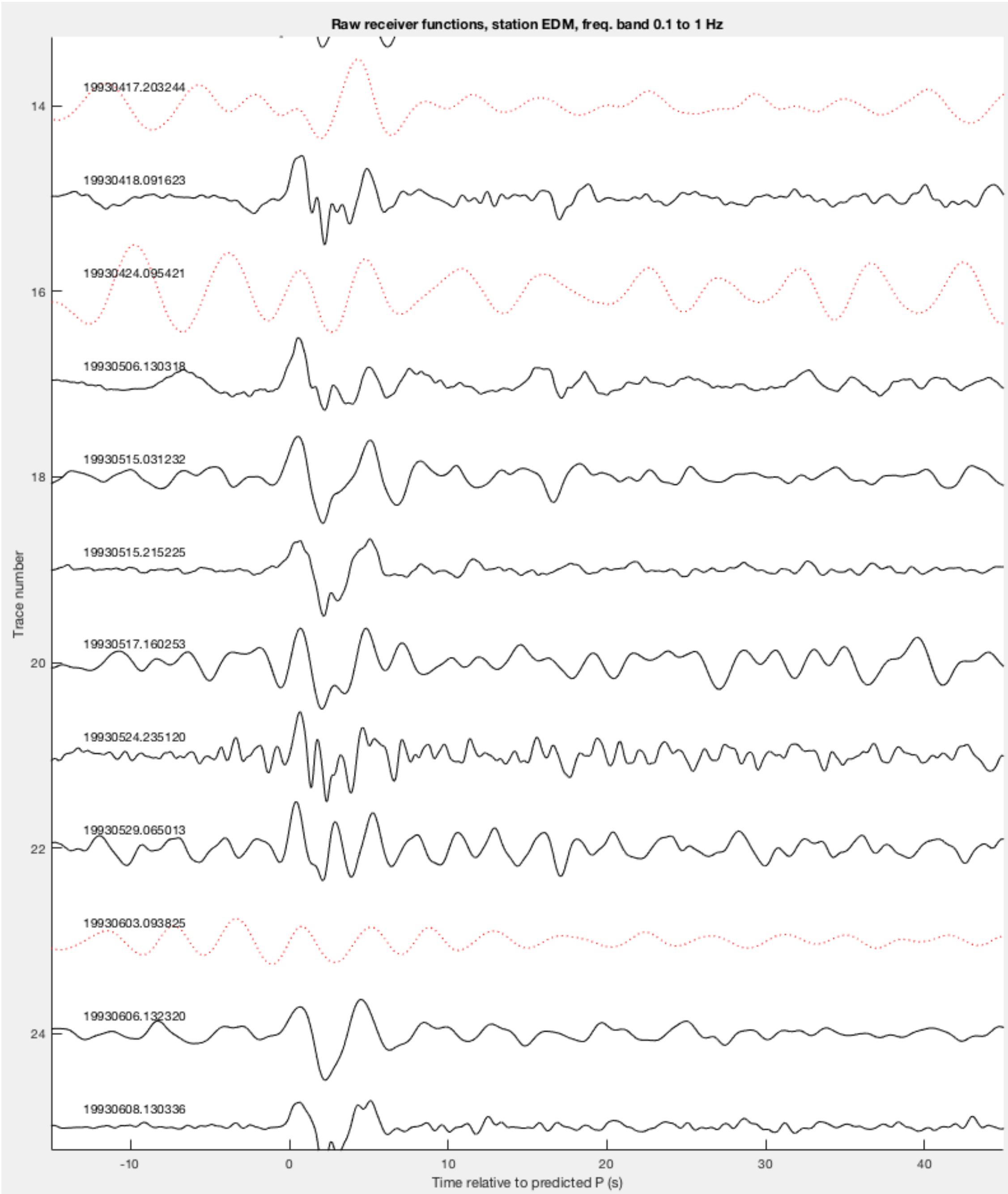

Pre-processing and quality control were completed on the data from the Williston Basin study area prior to the start of this research project. Quality controlled data was taken from Frederiksen and Delaney (2015). The same standards for quality control were used on these data as for EDM.

Chapter 6. Station EDM

6.1 Regional background

This chapter I will describe a layer-strip test of data from station EDM, the first real-world application of this methodology. A collection of teleseismic data from EDM station are filtered for the purpose of comparing the layer-stripped and non-layer-stripped receiver functions. Following this an H-K stack is completed on both data sets to determine crustal properties, and the effect of the layer-strip on the results.

EDM is located 10 km south of Edmonton, Alberta at latitude 53.223° N, longitude 113.349° W and elevation 727 m. The station is in the central portion of the Western Canada Sedimentary Basin (Porter *et al*., 1982). This station's data is ideal for testing the layer-strip methodology due to the location's thick Phanerozoic sediments and the complicated receiver functions produced here due to basin reverberations (Porter *et al*., 1982; Cassidy, 1995). To test the effectiveness of the layer-strip filter, we must produce a model of the elastic properties of the crust in this location. It is useful to look at the local geology around the station in search of physical constraints for the model.

The Western Canada Sedimentary basin was emplaced on the Precambrian continental craton (Porter *et al*., 1982). The basement Precambrian crystalline igneous and metamorphic rock ranges in age from 2.5 Ga to 1.75 Ga and was formed from various collisions crustal blocks (Porter *et al*., 1982). The boundary between Precambrian basement and sedimentary basin produces a strong velocity contrast. This velocity contrast is the main contributor to reverberations in data collected over the Western Canada Sedimentary Basin.

Station EDM lies east of the Cordilleran foreland thrust belt, towards the central portion of the Western Canada Sedimentary Basin. The thickness of Phanerozoic sediments at the station location is approximately 2.5 km (Porter *et al.,* 1982; Cassidy, 1995). The sedimentary basin thickness is shown in Figure 6.1. This thickness value is used in the layer-strip model.

Figure 6.1. Thickness of Phanerozoic rocks east of the Cordilleran foreland thrust belt. Contours are in km and EDM station is marked as a red star (modified from Porter et al., 1982).

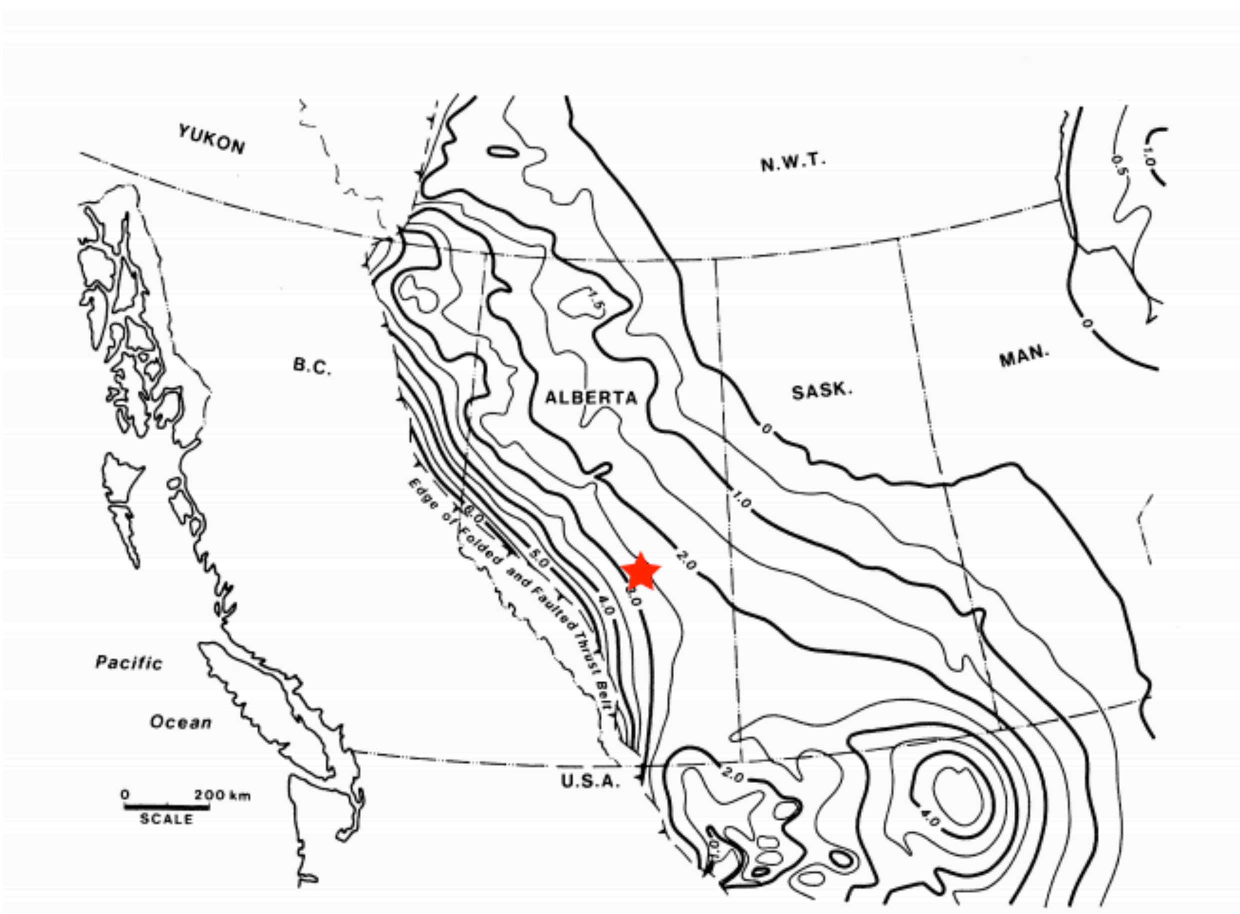

The Western Canada Sedimentary Basin is defined evolutionarily by six stratigraphic sequences. Each of these sequences comprises a transgression-regression megacycle (Porter *et al.,* 1982). Prior *et al.* (2013) indicate that EDM is located on a bedrock comprised of the Upper Cretaceous and Paleogene Edmonton Group overlying the Belly River Group. The uppermost portion of the Edmonton group at this location is the Horseshoe Canyon Formation. The sedimentary bedrock consists primarily of fine-grained feldspathic sandstone to coarse-grained bentonitic to carbonaceous sandstone. Coal layers are also present in the sedimentary bedrock (Prior *et al.,* 2013). The Late Cretaceous sediments of the Edmonton Group are poorly consolidated (Bayrock and Berg, 1966). The sedimentary bedrock of the Edmonton Group is overlain by unconsolidated surficial deposits that can be divided into three units. The surficial deposits include preglacial Saskatchewan sands and gravels, overlain by glacial till that is again overlain by glacial Lake Edmonton sediments. Surficial deposits in the Edmonton area generally range in thickness from 23 to 55 m in thickness, but the exact location of EDM is not sampled (Bayrock and Berg, 1966). The surficial deposits are of small enough thickness that they are not included in the models from Cassidy (1995) and Crust1.0.

Beyond understanding the geology of the region, an elastic property model is needed to perform the transfer function/layer-strip filtering method (such as Table 4.1). As a starting place for this search, Crust1.0 is used. Crust1.0 is a global crustal model with a resolution of 1 degree (Laske *et al*., 2013). This means that the model contains crustal properties for each 1-by-1 degree square of earth's surface. The model is based on a recently (as of 2013) updated database of crustal thicknesses derived from active and passive source seismic studies (Laske *et al*., 2013). The depths to interfaces, P and S velocity and density are given for 8 layers (some of which are listed as 0 thickness at EDM). The layers are: water, ice, three sedimentary rock layers and upper, middle and lower crystalline crust. The layer boundary is relative to sea level, and at EDM the first two layers (water and ice) are listed at 0.71 km which corresponds to a thickness of 0 km as expected. The third/lowest sedimentary layer also has a thickness of 0 km. Therefore, the Crust1.0 model splits the sedimentary basin into two distinct layers with respect to elastic properties. Four other layers have non-zero thickness; the model containing these layers is presented in table 6.1. Layer 1 is the upper sedimentary layer, layer 2 is the lower sedimentary layer, layer 3 is the upper crystalline portion of the basin, layer 4 and 5 are lower layers of the crystalline basement and layer 6 corresponds to the Earth's uppermost mantle.

Table 6.1 Model EDM-1. Parameters from model CRUST1.0 at latitude 53.223, longitude -113.349. The first two layers are sedimentary, the next three are the rest of earth's crust and the final layer is the half space or the earth's mantle.

EDM-1	1(sedimentary)	2(sedimentary)	3	4	5	6
S Velocity (m/s)	1070	2740	3530	3710	3930	4400
P Velocity (m/s)	2500	4800	6100	6500	6900	8100
Density (kg/m^3)	2110	2500	2740	2830	2920	3300
Depth to bottom of layer (m)	490	2400	14050	27150	38790	

Although CRUST1.0 may be an effective starting point, it is worthwhile attempting a second model for the layer-strip to compare the results when different crustal models are used to generate the filter. Cassidy (1995) produced a velocity model for EDM station displayed in table 6.2. This model is based on a starting model taken from Zelt and Ellis (1989). It was generated from an interpreted section of refraction seismic data in the Peace River Arch region of the Western Canada Sedimentary Basin, 350 km northwest of EDM. Somerville and Ellis (1972), Porter *et al* (1982) and Cassidy (1995) all have a 2.5 km thick sedimentary rock layer located at EDM.

Table 6.2 Model EDM-2. A second model for the crust below EDM based on Cassidy (1995).

EDM-2	1(sedimentary)	2(sedimentary)	3	4	5
S Velocity (m/s)	1100	2200	3600	3900	4800
P Velocity (m/s)	2500	3800	6300	6700	8300
Density (kg/m^3)	2100	2500	2700	2800	3300
Depth to bottom of layer (m)	700	2500	17000	37000	

6.2 Receiver function analysis

After producing two receiver side layer-strip models, two layer-strips can be performed on data from EDM. After preprocessing and applying quality control to the data collected from EDM between 1993 and 2001, the data are filtered using the layers-strip methodology outlined in Chapter 3. A suite of MATLAB scripts generates synthetic receiver side seismic data, based on the input elastic model with and without the layers to be removed. The scripts then generate the layer-strip filter and the filter is applied. After this is completed with the models EDM 1 and EDM 2, two layer-stripped versions of the EDM data exist, and can be compared to the non-layer-stripped data.

The first layer-strip filter is generated using EDM-1 taken from Crust1.0. The results of the first layer-strip are displayed as receiver functions stacked in bins and plotted by ray parameter (Figure 6.2 and 6.3). After the layer-strip is applied to the vertical and radial component of the seismic data, corrected receiver functions are produced and finally a bandpass filter is applied.

The bandpass filter is produced as a Butterworth filter with maximum and minimum frequency values, and applied as a zero-phase filter in MATLAB. The same bandpass filter is applied to the non-layer-stripped data for effective comparison. Two different frequency bands are used for displaying the results so that the differences can be analyzed. Figure 6.2 uses a 0.08-0.8 Hz bandpass filter and Figure 6.3 uses a 0.05-0.5 Hz bandpass filter. The bandpass filter removes undesirable high frequencies as well as low frequencies. The filtering also is likely removing reverberations from the data from thinner layers which produce relatively high frequency reverberations.

Figure 6.2 Non-layer-stripped receiver functions (left panel) and layer-stripped receiver functions (right panel) plotted and stacked in bins by ray parameter from EDM station. The results in the right panel were filtered using the model in Table 6.1 from Crust1.0. Both plots are bandpass filtered between 0.08 and 0.8 Hz.

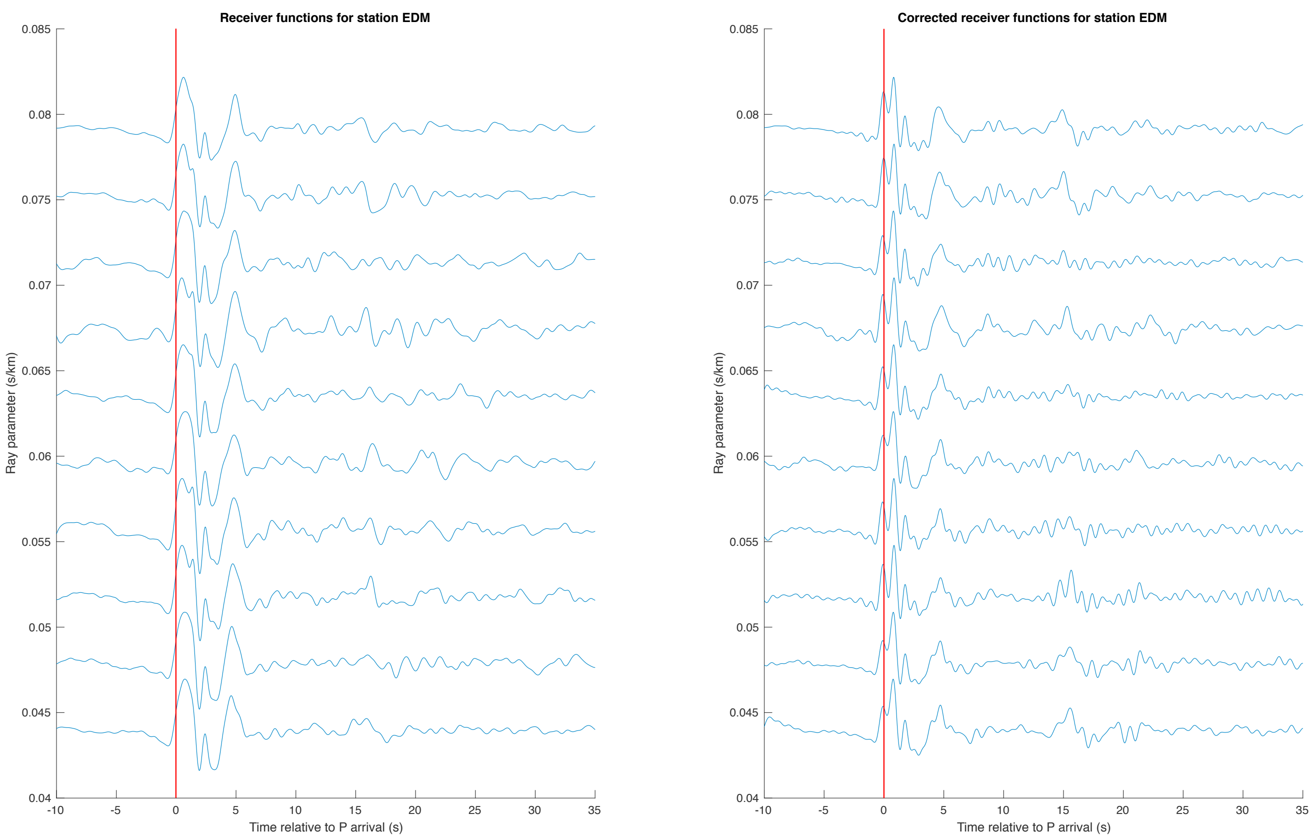

Figure 6.3 Non-layer-stripped receiver functions and corrected (layer-stripped) receiver functions plotted and stacked in bins by ray parameter from EDM station. Filtered using the model in Table 6.1 from Crust1.0. Both plots are bandpass filtered between 0.05-0.5 Hz.

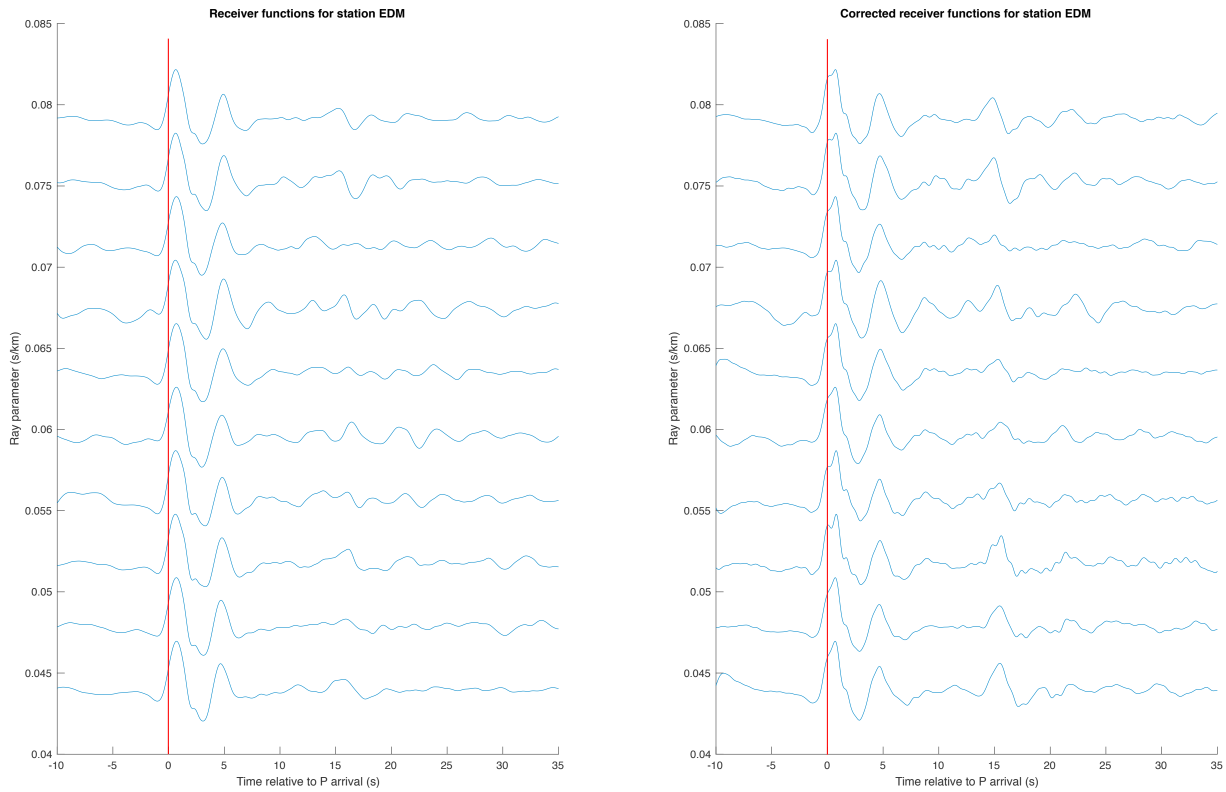

In figure 6.2 the results from the EDM layer-strip using the Crust1.0 model is displayed with a bandpass of 0.08-0.8 Hz. It is clear that, as with the synthetic tests in Chapter 5, the layer-strip filter is amplifying higher frequencies. The first arrival has moved to an earlier time with the layer-strip filter, and the arrival appears to have separated into the basin conversion (PbS) and the original arrival, where the two are combined in the non-layer-stripped counterpart. If the layer-strip were perfect, we would expect that the basin conversion would be removed, instead of separating the arrivals. The Moho conversion at about 5s appears to be mostly unaffected, but at smaller ray parameters it has become a sharper peak. A sharper, or higher frequency peak would be useful for analysis, as picking arrival times is more accurate with sharper arrivals. The most prominent change to the receiver functions, excluding the high frequency noise, is the improvement to the 15 s PpmS arrival. The layer-stripped data has an improved signal to noise ratio for that arrival, as its amplitude has been increased relative to the background.

Due to the high-frequency noise in the layer-stripped receiver functions, a second look is taken at these data with a lower frequency passband (Figure 6.3). 0.5 Hz is a typical lowpass frequency for receiver functions (Cassidy, 1992). This new passband removes the majority of added noise, and makes the layer-stripped and non-layer-stripped receiver functions appear more similar. Ensuring the displayed frequency is below 0.5 Hz improves the appearance of the data, and it is clearer that the layer-strip is at least partially effective in removing the effects of basinal reverberations by improving the signal to noise ratio of certain arrivals. Once again, the 15 s PpmS arrival is improved. The 21 s PsmS arrival also seems to be more visible in the layer-stripped receiver functions. The separation of the first arrival that was observed in Figure 6.2 is no longer obvious. The 0.5 Hz filtered response is a promising result, and indicates that a global database model such as Crust1.0 may be accurate enough in well-explored areas to provide models for the layer-strip.

While the 0.5 Hz bandpass displays the layer-stripped receiver functions more cleanly, some features (such as the separated first arrival) are lost to the filter. The frequency content of the layer-stripped and non-layer-stripped receiver functions is displayed in Figure 6.4. It is clear that the layer-strip has affected the frequency content of the receiver functions, especially between 0.7 and 1.5 Hz. The layer-strip causes this band to dominate the frequency spectrum. Between 0.05 and 0.5 Hz the frequency spectrum is relatively similar between the two spectra in Figure 6.4. The noise generated by the layer-strip is dominating in frequencies not usually considered during receiver function analysis. This is an important consideration for this methodology, as the result indicates it will still be useful in removing basin reverberations in bands below the threshold of this noise.

Figure 6.4. Frequency spectrum of stacked receiver functions from EDM for layer-stripped and non-layer-stripped data. Power here represents the amplitude at corresponding frequencies. Filtered using the layer-strip model EDM-1 from Table 6.1.

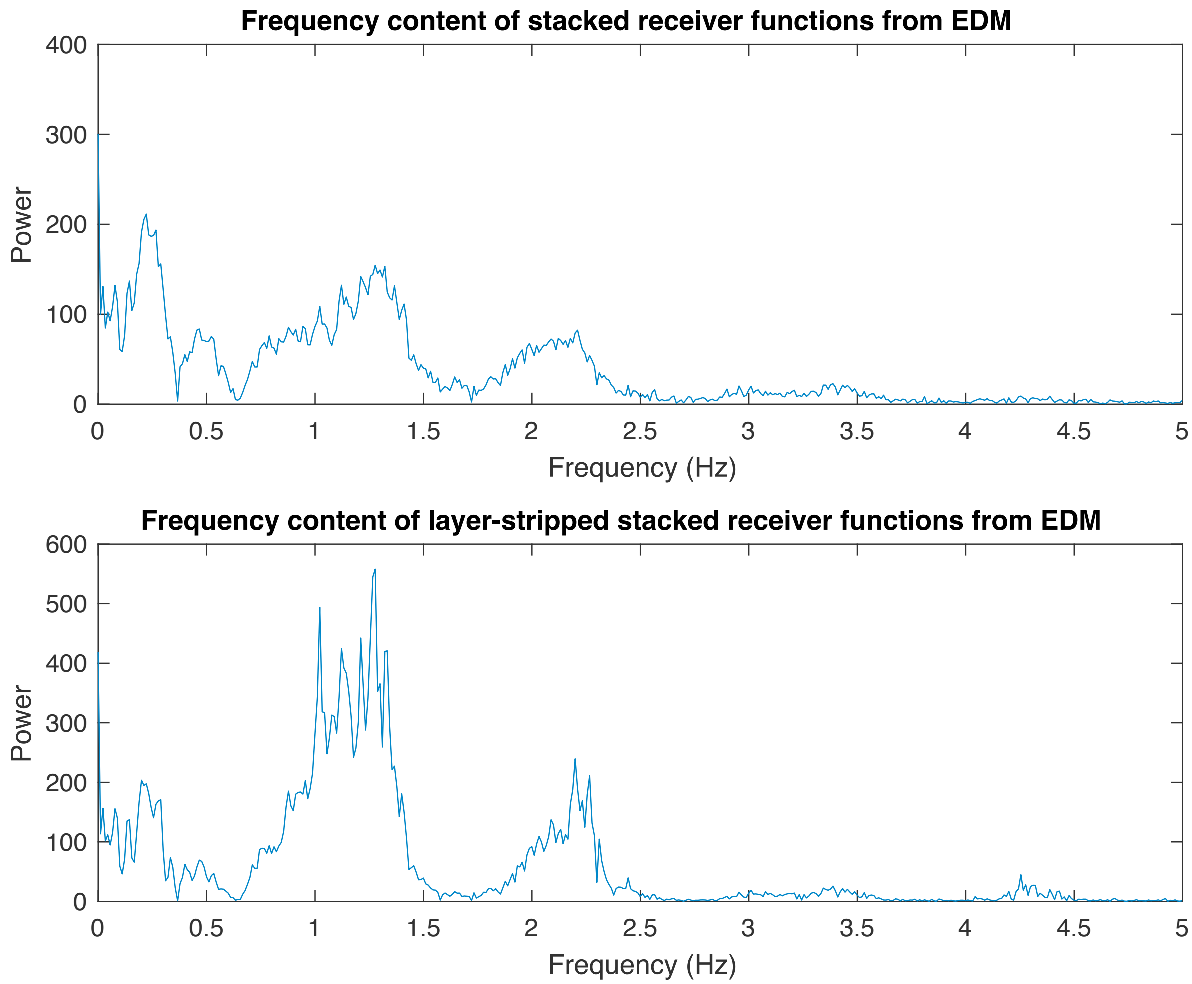

A second layer-strip filter is generated using the model from Table 6.2 taken from Cassidy (1995). After the layer-strip is applied to the vertical and radial component of the seismic data, receiver functions are produced and finally a bandpass filter is applied. The same bandpass filter is applied to the non-layer-stripped data as well as the layer-stripped data to allow for effective comparison. Once again, the results of the layer-strip are displayed as receiver functions stacked in bins and plotted by ray parameter (Figure 6.5 and 6.6). The band-passed non-layer-stripped receiver functions are identical to the ones in Figure 6.2 and 6.3 but are repeated for ease of comparison. Two frequency bands are again used for displaying the results. Figure 6.5 uses a 0.08-0.8 Hz bandpass filter and Figure 6.6 uses a 0.05-0.5 Hz bandpass filter.

Figure 6.5. Non-layer-stripped receiver functions and corrected (layer-stripped) receiver functions plotted and stacked in bins by ray parameter from EDM. Filtered using the model outlined in Table 6.2 from Cassidy (1995). Both plots are bandpass filtered between 0.08-0.8 Hz.

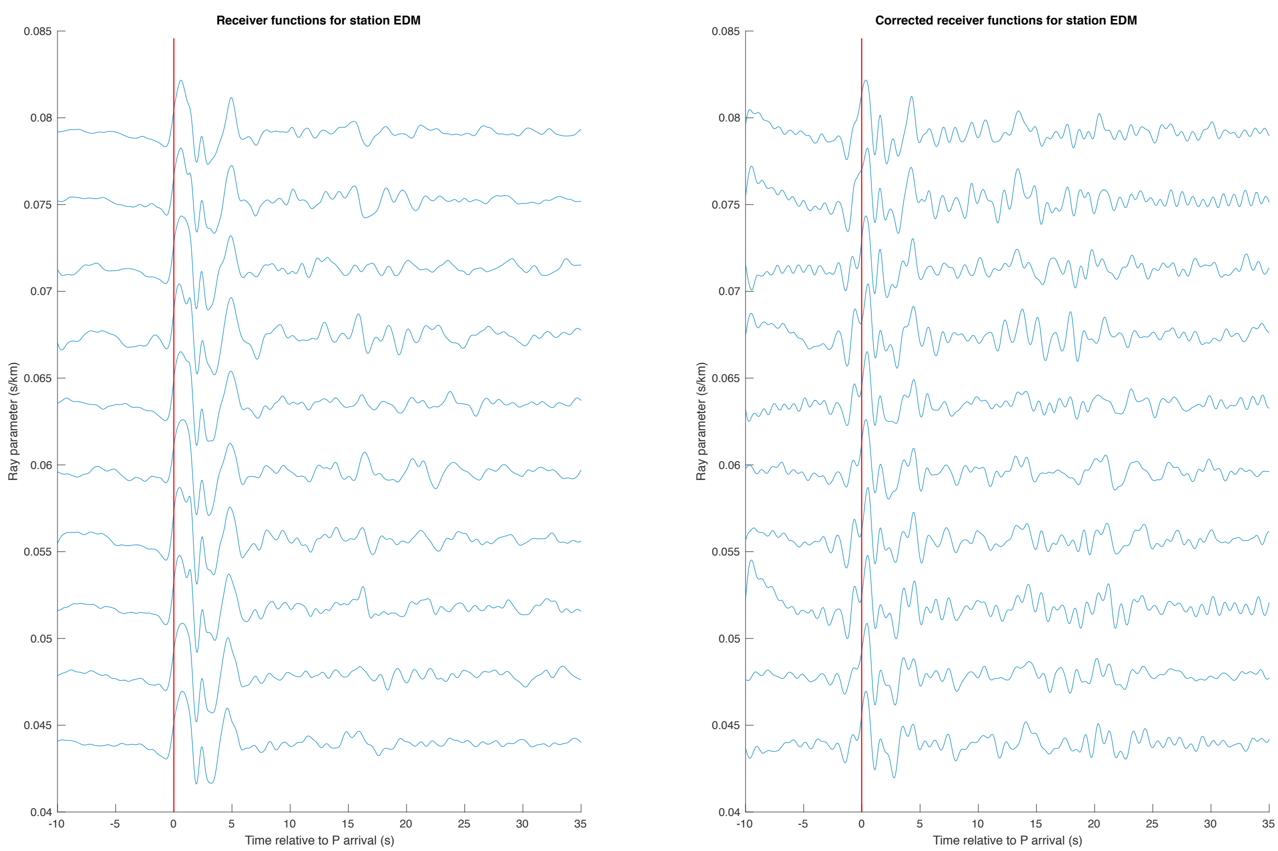

Figure 6.6. Non-layer-stripped receiver functions and corrected (layer-stripped) receiver functions plotted and stacked in bins by ray parameter from EDM. Filtered using the model outlined in Table 6.2 from Cassidy (1995). Both plots are bandpass filtered between 0.05-0.5 Hz.

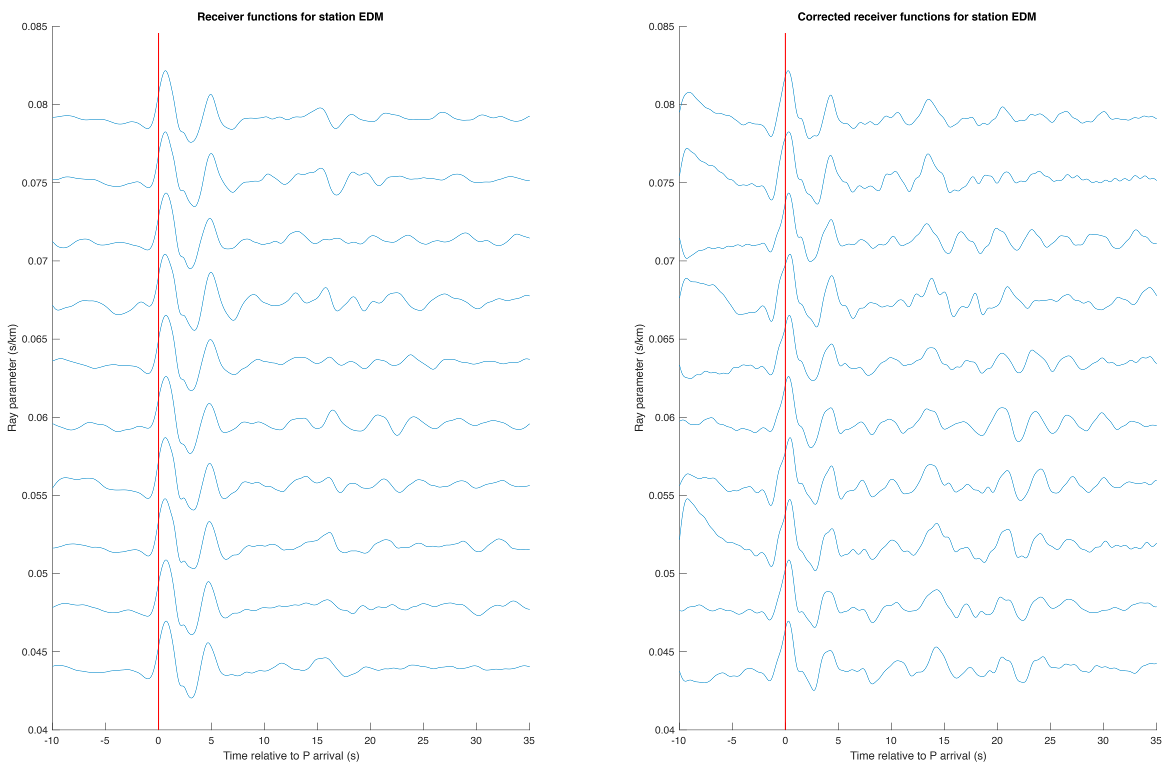

The filter generated from model EDM-2 appears less effective than from the previous model when viewed in the passband of 0.08-0.8 Hz (Figure 6.5 and 6.2). There is more noise in these receiver functions than in Figure 6.2 and the negative times contain a slope that is less present in either of the plots in Figure 6.2. The first arrival is located at negative time for some of the ray parameters, with the same separation happening as with model EDM-1 into a P arrival and PbS arrival. The earlier arrival is expected, as the velocity in the second layer of sediments is reduced with EDM-2 (Table 6.1 and 6.2). Removing the effects of the layer, and layer-stripping to the base of the sedimentary layer (and replacing it with basement material) will make the first arrival appear earlier in time.

In Figure 6.6 where the passband used is 0.05-0.5 Hz, the layer-stripped receiver functions appear less noisy compared with Figure 6.5. The 15 s PpmS arrival is increased in amplitude in the layer-stripped version of Figure 6.6. The first arrival is also located closer to 0 s. The layer-strip in this frequency band has led to later times being noisier than the non-layer-stripped counterpart. Arrivals later than 15 s are obscured by reverberations in the majority of ray parameter bins in the corrected portion of Figure 6.6. The layer-strip based on model EDM-2 appears to be less effective than the earlier Crust1.0 EDM-1 layer-strip. This result could be due to the size of dataset used to generate Crust1.0's, implying that it should be incorporating newer, controlled source data and should therefore be a more effective model. In contrast, Cassidy (1995) uses data to generate an elastic model from Zelt and Ellis (1989) and Somerville and Ellis (1972). Since EDM-2 is based on an older, sparser dataset, this may explain the poorer performance.

The frequency content of the second EDM layer-strip is displayed in Figure 6.7. The non-layer-stripped frequency spectrum is also displayed a second time, as it is useful for comparison. Similar to the Crust1.0 layer-strip frequency spectrum, there is increased power in the range from 0.7 to 1.2 Hz. The spectrum near 0.25 Hz is altered more from the non-layer-stripped data compared to the first layer-strip (Figure 6.4). To further assess the effects of the layer-strip filter, both sets of filtered data, and the unfiltered data are used to determine crustal properties at EDM.

Figure 6.7. Frequency spectrum of stacked receiver functions from EDM for layer-stripped and non-layer-stripped data. Power here represents the amplitude at corresponding frequencies. Filtered using a layer-strip model from Cassidy (1995) and Table 6.2.

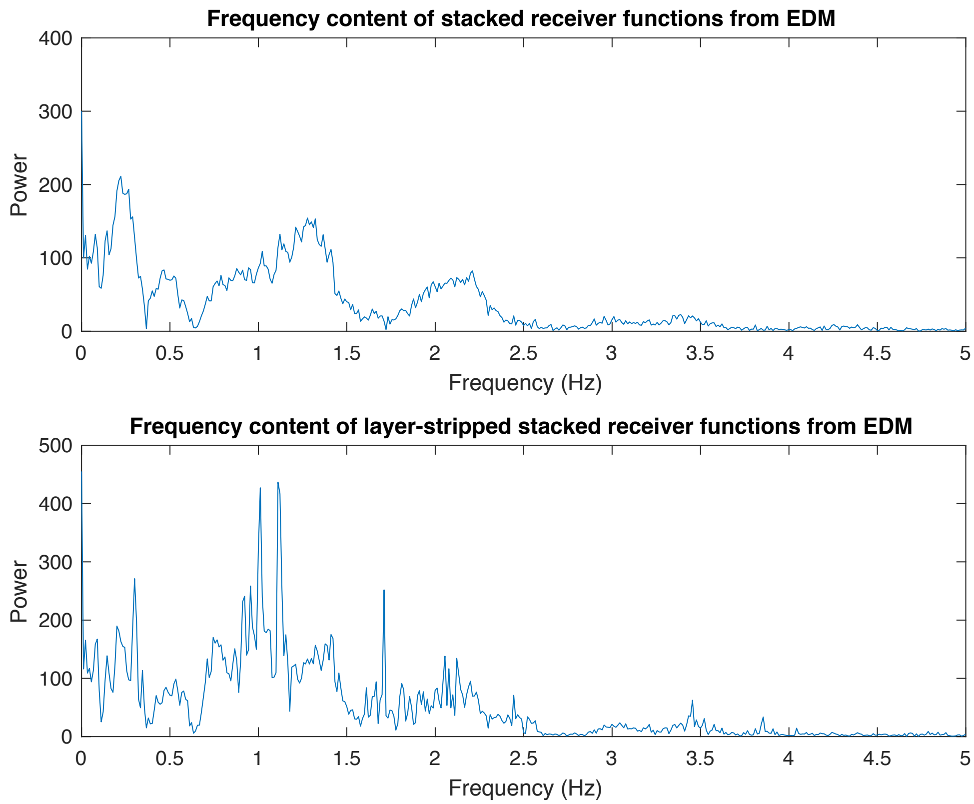

6.3 H-K stacking analysis

Analyzing the difference between receiver functions with and without layer-stripping is useful in determining the effectiveness of the methodology, and the effects of the filter with different models. Another technique to determine the effects of the layer-strip is to use the filtered data in receiver function analysis to determine crustal thicness and Vp/Vs. Once again, we can compare the results with the non-layer-strip results. H-K stacking, a crustal thickness and Vp/Vs grid search method, is chosen as it is a standard form of crustal analysis with a history of teleseismic use (Zhu and Kanamori, 2000; Crotwell and Owens, 2005; Eaton *et al*., 2006; Yuan *et al*., 2010; Fontaine *et al.,* 2013). This technique relies on recognizing maximum local amplitudes of stacked receiver functions that correspond to phase arrival times estimated from a grid of crustal thicknesses and Vp/Vs (Zhu and Kanamori, 2000). The effectiveness of the H-K stack is dependent on the amount of noise in the data. Incorrect times may be associated with reverberations instead of the sought phase arrivals, if the amplitude of similar timed reverberations is significant. Reverberation noise can alter the estimation of crustal thickness by up to 10 km (Yeck *et al.*, 2013)

Using the methodology outlined in Chapter 3, the non-layer-stripped data from EDM are used in a 4th root H-K stack. Default weights for the three phases are used corresponding to 0.5 for Ps, 0.25 for Pps and 0.25 for Pss. Receiver functions are calculated for each event that passed quality control, and they are combined in a stack. A grid of H and K values is generated in which each point on the grid corresponds to an arrival time on the stack. The point on the grid of highest stacked amplitude at the arrival times provides the estimate of H and K for the data. Figure 6.8 contains an illustration of the result for EDM where no layer-stripping is performed. The result is a crustal thickness of 38.4 km. This estimated thickness is between the total crustal thickness of the two models in Table 6.1 and 6.2. Similar values to the models are expected, as receiver function analysis is at least partially used to determine the crustal thickness for both models (Laske et al., 2013; Cassidy, 1995). The result in Figure 6.8 also indicates a second maximum within a zone of 90% of the maximum amplitude at 33.2 km. The receiver functions are passband filtered between 0.08 and 0.8 Hz. This band was chosen to be consistent between H-K stacks, given that data above this frequency contain the majority of the additional power in the layer-stripped spectra (Figure 6.4 and 6.7).

Figure 6.8. Result from 4th root H-K stack performed on non-layer-stripped data from EDM station. Areas of lighter color show a higher stacked amplitude at times calculated using associated crustal thickness and Vp/Vs. Resulting crustal thickness is 38.4 km. The asterisk indicates the maximum stacked amplitude.

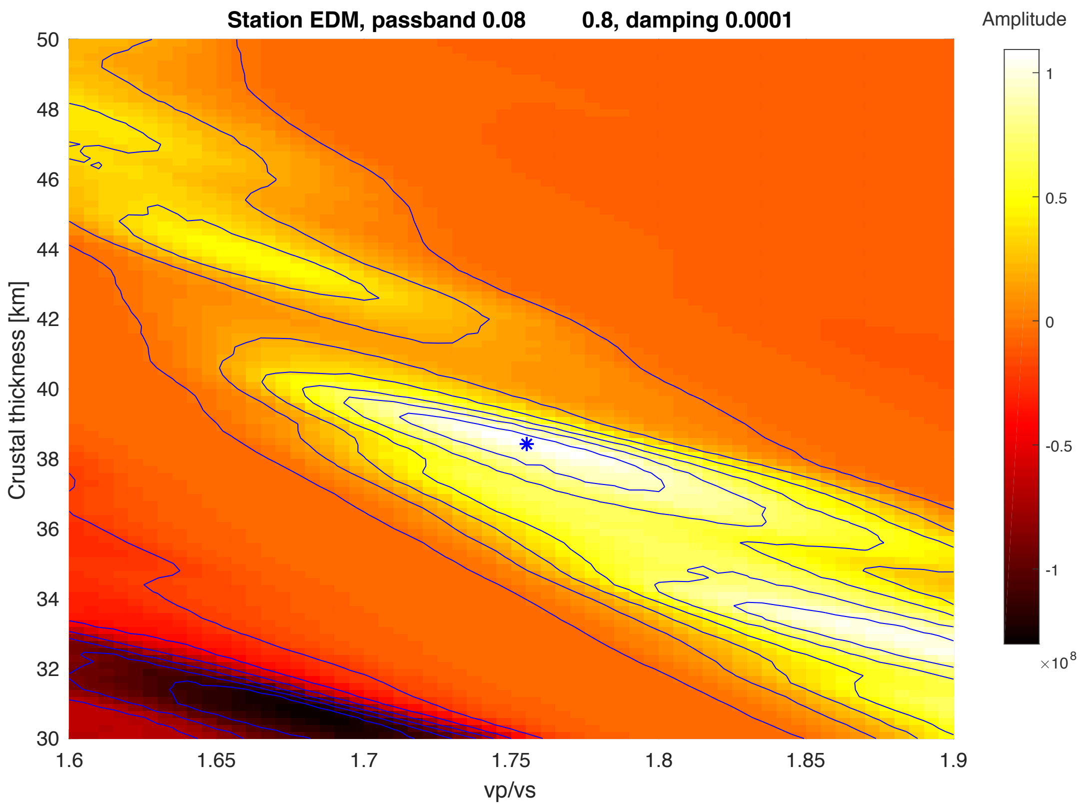

The layer-stripping process, under perfect circumstances, removes the effect of the sedimentary basin layer. This has the effect of reducing the calculated crustal thickness, as the basin is replaced with higher velocity crust, and the time average velocity of the crust is increased beyond the actual velocity. This corrected value should represent a more accurate crustal thickness estimate, because the HK stack does not account for a sedimentary basin but instead it presumes a 1-layer crust. The change in estimated crustal thickness from removing the basin will complicate the comparison to the non-layer-stripped result, which is ultimately the goal. To account for this change, the travel time change was calculated, and the corresponding crustal thickness was added to the layer-stripped results to produce corrected crustal thickness values. This is done using the time average equation, under the presumption the rays are travelling vertically.

The same H-K stack method as above is applied to the EDM data after filtering using the EDM-1 model from Crust1.0. The results of the H-K search are displayed in Figure 6.9. The EDM-1 layer-stripped H-K stack returned a crustal thickness of 35.8 km. After this value is altered to account for the layer-stripping effect, the crustal thickness is 37.5 km, 900 m thinner than the non-layer-stripped estimate in Figure 6.8. The highest amplitude region of the grid search appears much tighter in Figure 6.9 than in Figure 6.8. This indicates that the layer-strip has improved the resolution and confidence of the result. The range of crustal thickness within 90% of maximum stacked amplitude has been reduced from 1 km to 0.3 km and the range of Vp/Vs has been reduced from 0.9 to 0.5. Finally, the Vp/Vs is increased when the sedimentary effects are stripped.

Figure 6.9. Result from H-K stack performed on layer-stripped data from EDM station. The data is filtered using model EDM-1. Areas of lighter color show a higher stacked amplitude at times calculated using the associated crustal thickness and Vp/Vs. The resulting corrected crustal thickness is 37.5. The asterisk indicates the maximum stacked amplitude, and corresponds to the crustal thickness before correction.

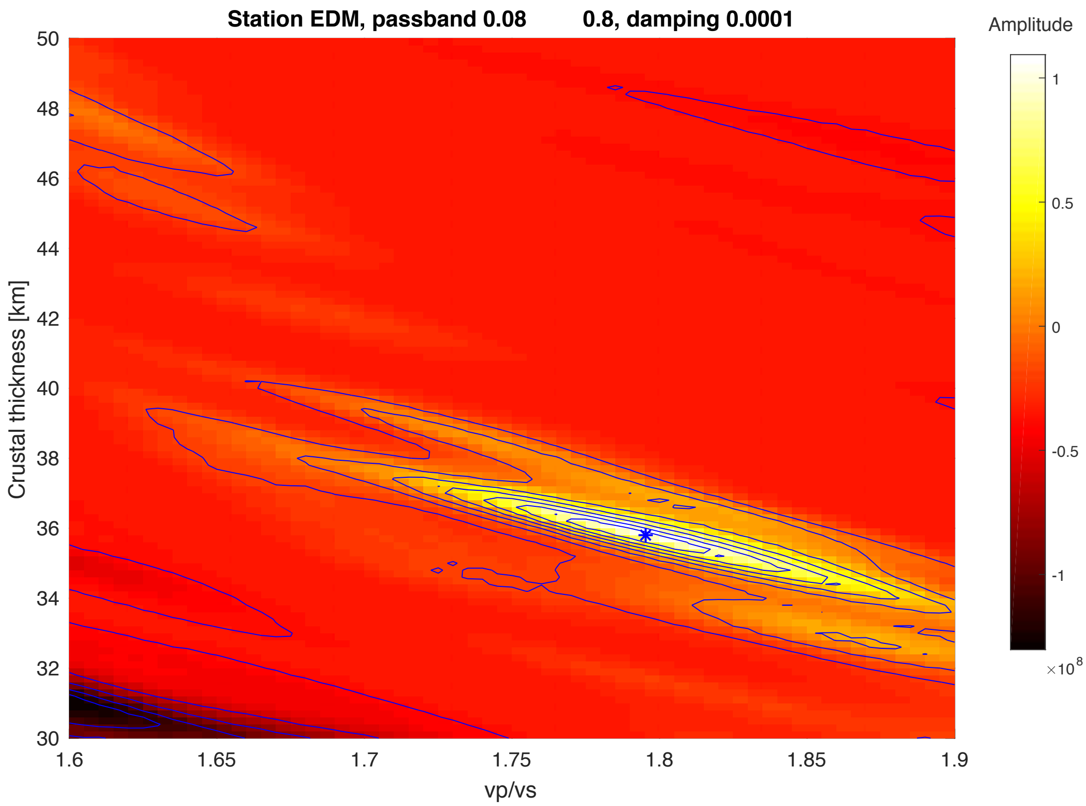

The agreement between the layer-stripped H-K stack and the non-layer-stripped result is moderately high, which may indicate that the initial H-K stack result was fairly accurate. As noted earlier, in figure 6.8, a second local maximum of high amplitude exists at a shallower crustal thickness and larger Vp/Vs (33.2 km). This local maximum is within 90% of the amplitude of the regional maximum and offers a second potential solution to the H-K search. The existence of the local maximum is likely due to basin reverberations in the receiver functions, producing a local amplitude surface, as this second maximum is mostly removed after the layer-strip (Figure 6.9). If the second solution in Figure 6.8 had generated a higher amplitude, the layer-strip would have made a substantial correction in the H-K stack by removing it.

Finally, an H-K stack is done on the EDM data layer-stripped using model EDM-2 to produce Figure 6.10 and a crustal thickness of 33.0 km. After the layer-strip correction, the crustal thickness is estimated to be 35.7 km. Once again, the stacked receiver functions produce a higher resolution estimate compared with Figure 6.8. This is likely due to the higher frequency arrivals visible in the corrected portion of Figure 6.5 compared with the other receiver functions. The resulting crustal thickness is 2.76 km thinner than in the non-layer-stripped H-K stack. Once again, the second local maximum at lower crustal depth is removed. It is unlikely that the result in Figure 6.10 corresponds to the smaller local maximum in Figure 6.8, as the shape of the contours around the global maximum in Figure 6.10 and 6.9 are similar. The discrepancy between the results for the two layer-strips is challenging to explain. Model EDM-2 from Cassidy (1995) may be underestimating the sedimentary rock velocity, and thus overcompensating with the layer-strip. The large difference between results in Figure 6.9 and 6.10 illustrates the importance of model accuracy, and the challenge of defining what an appropriate change is from the filter.

Figure 6.10 Result from H-K stack performed on layer-stripped data from EDM station. The data is filtered using model EDM-2. Areas of lighter color show a higher stacked amplitude at times calculated using associated crustal thickness and Vp/Vs. Resulting corrected crustal thickness is 35.7 km. The asterisk indicates the maximum stacked amplitude, and corresponds to the crustal thickness before correction.

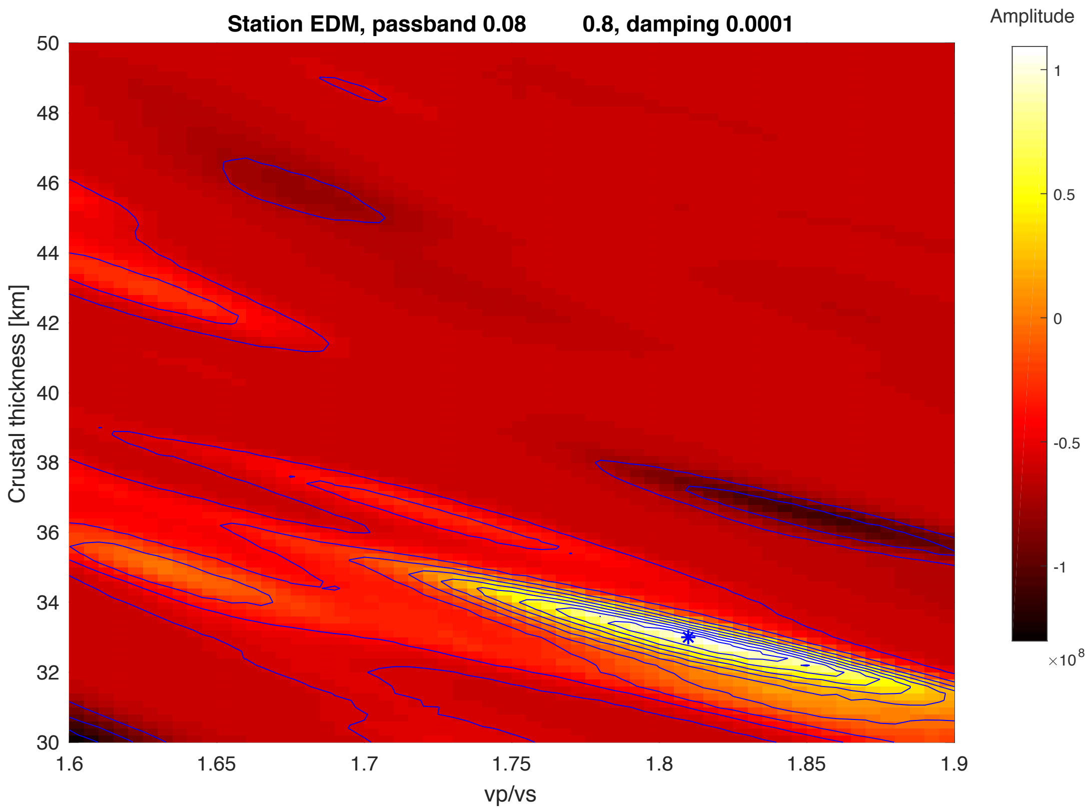

A trend can be determined from the two layer-strip tests, which matches the theoretical expectations. In the case of model EDM-2 (table 6.2), with lower velocity sedimentary rock, the crustal thickness after the layer-strip is more greatly altered compared to the layer-strip with the higher velocity sedimentary model. The Vp/Vs estimate has also increased a greater amount with the lower velocity basin. This test indicates that certain models may overcompensate or under compensate for the sedimentary basin layer. Determining if a model is effectively filtering the data is challenging. Despite this, it is clear that the signal to noise ratio is improved in times before 15s throughout the layer-stripped receiver functions. It is also clear that secondary local maxima are removed from the H-K stack, likely associated with reverberations. Finally, the resolution of the maximum amplitude is increased by the layer-strip.

Chapter 7. Williston Basin Transect

7.1 Regional background

To further test the effectiveness of the layer-strip methodology, a second set of teleseismic data is filtered and the results are analyzed in this chapter. For this purpose, the data are taken from seismometers throughout North and South Dakota (the Dakotas), Minnesota and into northern Iowa from stations that make up a portion of the Earthscope TA (Williams *et al.,* 2010). The stations sample a wide range of sedimentary thicknesses across the north-central United States (Figure 1.3). The teleseismic data are filtered for the purpose of comparing the layer-stripped and non-layer-stripped receiver functions (RFs) and H-K stacks. By studying the effect of the layer-strip filter on this data set, our understanding of the effectiveness of the filter on a basin of variable thickness can be improved.

The Williston basin is a large, petroleum-bearing sedimentary basin located near the center of the North American landmass in the Great Plains region of Canada and the United States (Burrus *et al.*, 1996; Gerhard *et al.*, 1991). The basin underlies land in Saskatchewan and Manitoba, and throughout the Dakotas and Montana (Figure 7.1). The depocentre of the Williston basin, where the axes of maximum deposition meet, is the thickest portion of the basin, and the basin thins towards the southeastern edge. To the east of the Williston Basin, sedimentary rock with decreasing by varying thickness exists in Minnesota and Iowa. In the Dakotas the Williston basin comprises Paleozoic carbonate rock at its base up to 2 km thick, overlain by siltstone and shale units of Mesozoic and Cenozoic age (Burrus *et al.*, 1996; Gerhard *et al.*, 1991). The siltstone and shale units are over 1.5 km thick in places. The basin is up to 4 km thick towards its centre and has a maximum diameter of nearly

1000 km (Burrus *et al.*, 1996; Gerhard *et al.*, 1991). Transportable Array stations A25A, B26A, C27A, D28A and E30A lie within the Williston Basin.

Figure 7.1. Map of the Williston Basin with lines of peak sedimentary unit thickness of Devonian and Carboniferous age, representing general thickness of Paleozoic sediment thickness. The 6 stations used from North and South Dakota are included (Modified from Kent and Christopher, 1994).

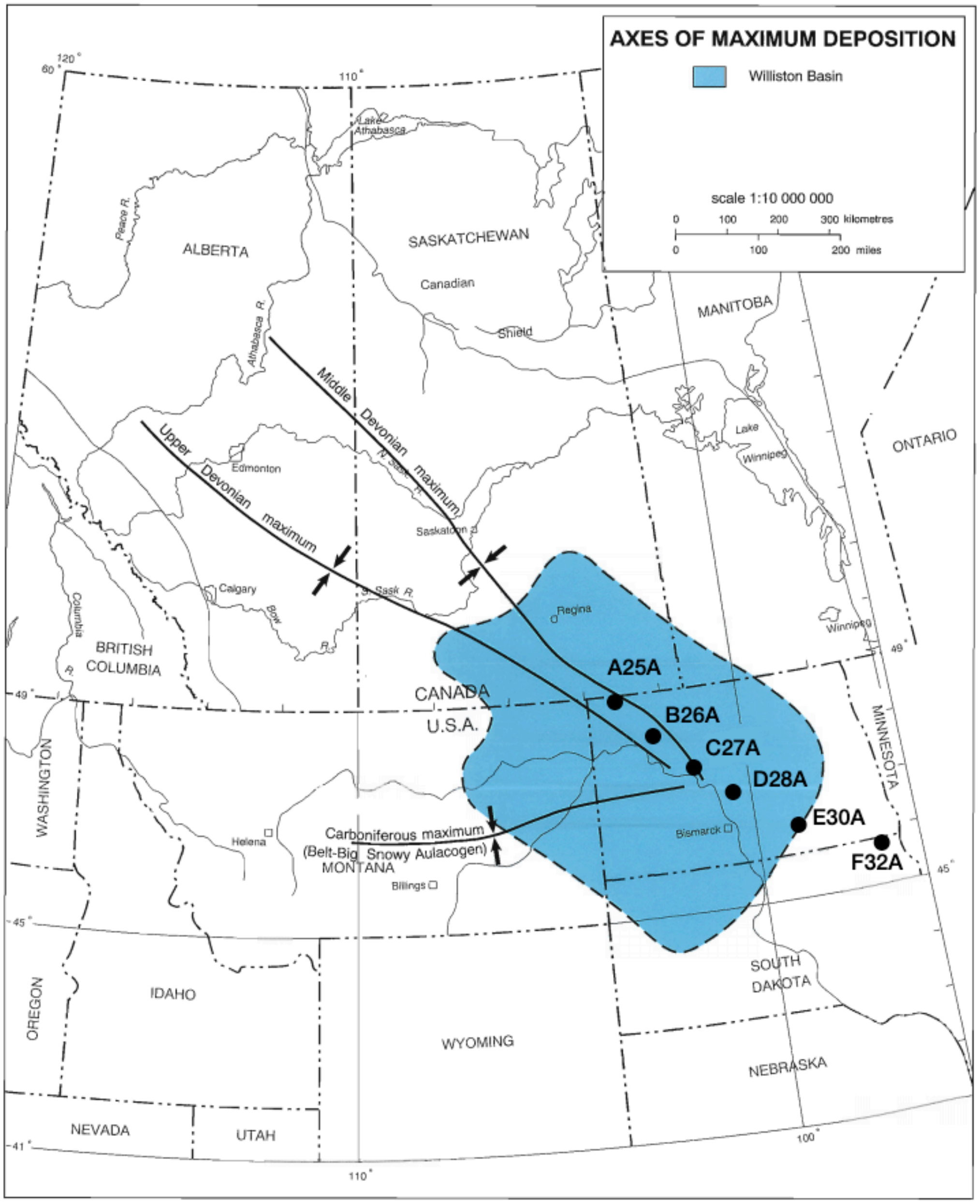

Stations were selected on a basis of availability, and to produce a transect across a range of sedimentary thicknesses. Only half of the stations selected lie within the Williston

Basin, while the remaining 5 stations lie over thinning sedimentary rock to the southeast. The stations selected from the TA are outlined in Table 7.1 and Figure 1.3. To generate the layer-strip filter, a crustal model of the elastic properties and layer thicknesses for each station must be developed. For this purpose, two data sources were used to generate two models at each station; the first is from Crust1.0 (Laske *et al.*, 2013) and a second from a previous teleseismic study of the TA data (Frederiksen and Delaney, 2015). By using these two different sets of models, we can test the relationship between model confidence/quality and layer-strip effectiveness. The models taken from Frederiksen and Delaney (2015) have varying misfit between each station and are therefore of varying confidence and quality. The models derived from Frederiksen and Delaney (2015) included only 1-layer basin structures. The models were modified into two-layer basins where sediment thickness is greater than 700 m. This decision is based on regional knowledge of the basin geology and discussed in Section 7.2.

Table 7.1. Stations used from the Earthscope Transportable Array that make up the transect for this study. See also Figure 1.3.

Station Name	Latitude	Longitude	State
A25A	48.94	-103.11	North Dakota
B26A	48.37	-102.23	North Dakota
C27A	47.71	-101.50	North Dakota
D28A	47.19	-100.56	North Dakota
E30A	46.50	-98.90	North Dakota
F32A	45.87	-97.12	South Dakota
G34A	45.24	-95.63	Minnesota
H35A	44.69	-94.83	Minnesota
I36A	44.01	-94.01	Minnesota
J38A	43.31	-92.47	Iowa

When considering the 1D velocity structure of the Williston Basin, the contact between the basin's carbonate basement and upper shale and siltstone units provides a useful interface bound (Burrus *et al*., 1996). Crust1.0 also generally contains a mid-basin interface based on geophysical data that corresponds with this boundary. Thus, dividing the sedimentary basin into two units is appropriate based on regional knowledge of the basin. The second set of elastic models for this region is taken from Crust 1.0. Two distinct sedimentary layers are present in the model in areas where sediment thickness exceeds 700 m (Laske *et al.*, 2013).

7.2 Background geophysics

COCORP (Consortium for Continental Reflection Profiling) studies were completed across the Williston Basin in North Dakota and to the east in Minnesota to study the crust in the 1980's and 1990's (Gibbs *et al.,* 1984; Nelson *et al.,* 1993; Baird *et al.,* 1995). These COCORP studies consisted of large-scale, deep-sensing reflection seismic lines that transected the Trans-Hudson Orogen and the transition zone within the Superior Province between younger terranes and the older Archean gneiss of the Minnesota River Valley Terrane. In the process, the overlying Williston Basin and sedimentary rocks in Minnesota including the Minnesota River Valley were studied as well (Gibbs *et al.,* 1984; Nelson *et al.,* 1993; Baird *et al.,* 1995).

The purpose of COCORP was to improve understanding of the tectonic history of the North American Craton, and therefore the surveys were on a crustal scale instead of a basin scale and did not focus on basin properties. The studies thus did not provide direct basin constraints such as velocity or thickness. Gibbs *et al.* (1984) found that the "L" group arrivals associated with the basin sedimentary rock produced multiples that were hard to distinguish from later arrivals. It is also likely that basin reverberations/multiples contributed to the weakly defined Moho described in Nelson *et al.* (1993).

With the release of EarthScope TA data, newer crustal and upper mantle studies could be completed in the Dakotas and Minnesota. Shen *et al.* (2013) used the TA data to study the western arm of the Midcontinental Rift in Minnesota and Iowa, including stations G34A, H35A, I36A and J38A used in this research. They used ambient noise and earthquake tomography to estimate Rayleigh wave phase velocities across the Midcontinent Rift. Receiver functions were also used in the analysis to construct 3-D models using a joint inversion of the surface wave dispersion curves and RFs. As a starting model for the joint inversion, Crust2.0 was used (Shen *et al.,* 2013). They found that some sedimentary rocks generate strong reverberations in RFs that coincide in time with the Moho arrival, resulting in large uncertainties in the crustal thickness map. The authors reference the poor reference sedimentary rock model in explaining the effect of reverberations on the joint inversion. In other areas with sedimentary rock, the Moho arrivals are not obscured but reverberations still exist. The authors also discuss the source of reverberations in northern Minnesota: low sedimentary velocities possibly associated with the Wadena glacial lobe moraines. With only 4 stations overlapping with this research, results from the Shen *et al.* (2013) study are not used as a source for models in this research.

Frederiksen and Delaney (2015) examined many of the Earthscope stations over the Dakotas, northern Iowa and Minnesota, including the 10 stations from this research, to estimate crustal thickness and bulk elastic properties throughout the southwestern Superior Province. They use transfer functions to predict the relationship between radial and vertical components of the teleseismic data. A catalogue of synthetic transfer functions is convolved with the vertical component of teleseismic data, and misfit is calculated between the result of the convolution and the true radial component. Crustal properties are estimated from models that produce a minimum misfit. This approach also allows for the estimate of sedimentary thickness (a two-layer model with a sedimentary layer and a crystalline crust below), as it does not require a single-layer crust like traditional H-K stacking.

The results from Frederiksen and Delaney (2015) are useful for this research in two ways. The results provide a basis for a set of models to produce layer-strip filters, as was completed at EDM in Chapter 6, but also offer an opportunity to compare the results of a layer-strip with the misfit of the model used to produce the layer-strip. The misfit between real and predicted vertical components allows for the comparison of model quality and layer-stripping effectiveness.

By analyzing the results from Frederiksen and Delaney (2015), the relationship between sedimentary thickness and final model misfit can be assessed (Figure 7.2). There is no linear correlation evident between sedimentary thickness and two-layer model misfit. The correlation coefficient is calculated to be 0.252. If station J38A is removed from the 10 data points, a weak correlation is observed, and results in a correlation coefficient of 0.464. Due to the lack of correlation, the sedimentary thickness is not determining the misfit of the output model. If instead sedimentary thickness and misfit were strongly correlated, a superior layer-strip at stations of low model misfit would imply that the layer-strip is only effective in areas lacking reverberations due to a thinner basin, but this is not the case.

Figure 7.2. Sediment thickness VS model misfit at stations used in this research. Data taken from results of Frederiksen and Delaney (2015). A lack of strong correlation between the two values is observed.

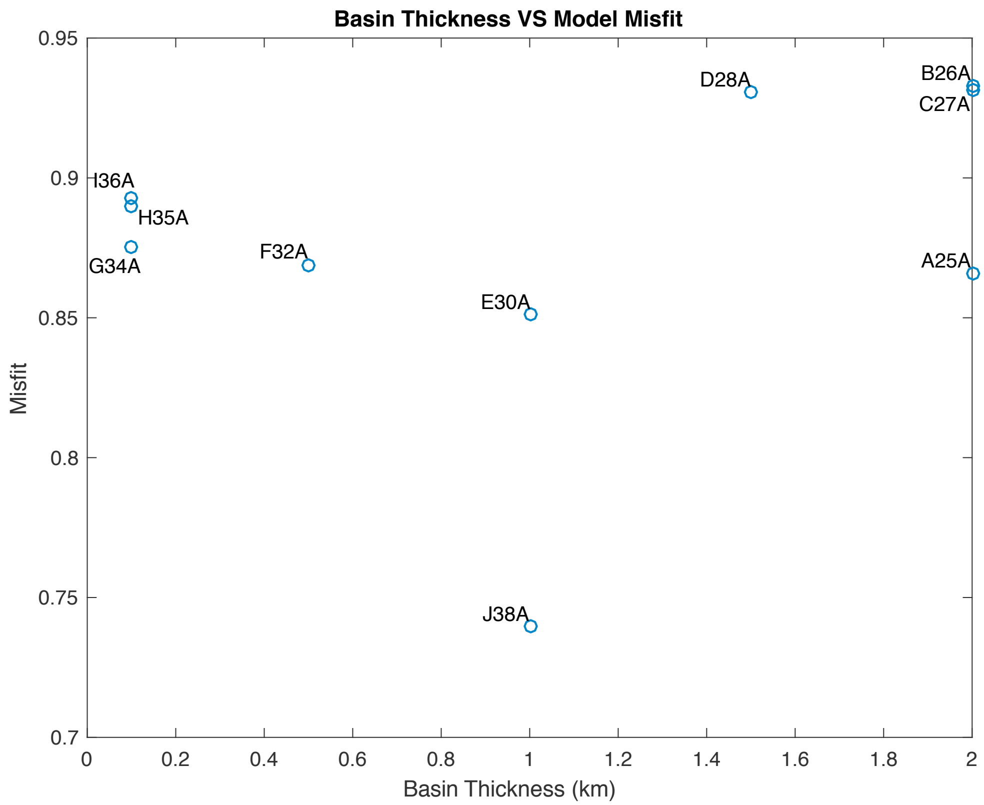

7.3 Data set and models

The source of data and the station selection criteria for the 10 stations looked at in this chapter are described in Chapter 5. The data were previously collected as part of the research described in Frederiksen and Delaney (2015).

The data set is described as having a significant transverse component, indicating a moderate strength of noise (Frederiksen and Delaney, 2015). The transverse component does not have a strong coherence with the other two components, indicating that structures such as dip or anisotropic fabrics are not responsible for the transverse energy.

This indicates that a horizontal layer approach is applicable. Reverberations are known to be present in the data set (Frederiksen and Delaney, 2015).

The first layer-strip filter applied to each station was generated using models taken directly from Crust1.0. This set of models is referred to as TA-1. Crust1.0 has a resolution that allows for a unique model at each of the ten stations in this research. The models ranged in complexity from 6 layers, where two sedimentary layers where present, to 4 layers, where no sedimentary layer was listed for the model. Stations with sediment thicker than 700m contained two sedimentary layers, while stations with thinner sediment contained one. Station G34A was the only station to have no sedimentary layer and therefore, a layer-strip could not be performed using the Crust1.0 model at that station.

Using two sources for the layer strip models provides a benchmark for consistency in the layer-strip, and demonstrates the effect that changes in model produce in the layer-strip results. Generally, it helps test the sensitivity of the methodology to models and model sources.

Frederiksen and Delaney (2015) provided a second estimate for crustal thickness and sedimentary thickness. This second set of models will be referred to TA-2. The model is produced with bounds from Frederiksen and Delaney (2015) applied to a consistent velocity model taken from Crust1.0. In areas where sedimentary thickness is greater than 700 m, a 4-layer crustal model was used with 2 sedimentary layers, while in areas with less than 700m of sediments a 3-layer model was used. The 700m value is based on the Crust1.0 data and results from Burrus *et al.* (1996). The importance of splitting the sedimentary layer in two in areas of greater thickness is demonstrated in section 7.4. The 10 models produced using this method are available in Appendix A and the estimated sedimentary thickness at each station is displayed in Figure 7.2. An example of the velocity models produced using this methodology is shown in Figure 7.3.

Figure 7.3. Velocity diagram developed from crustal and sedimentary basin thickness values from Frederiksen and Delaney (2015) and a velocity structure taken from Crust1.0. The red line is P velocity, and the blue line is S velocity.

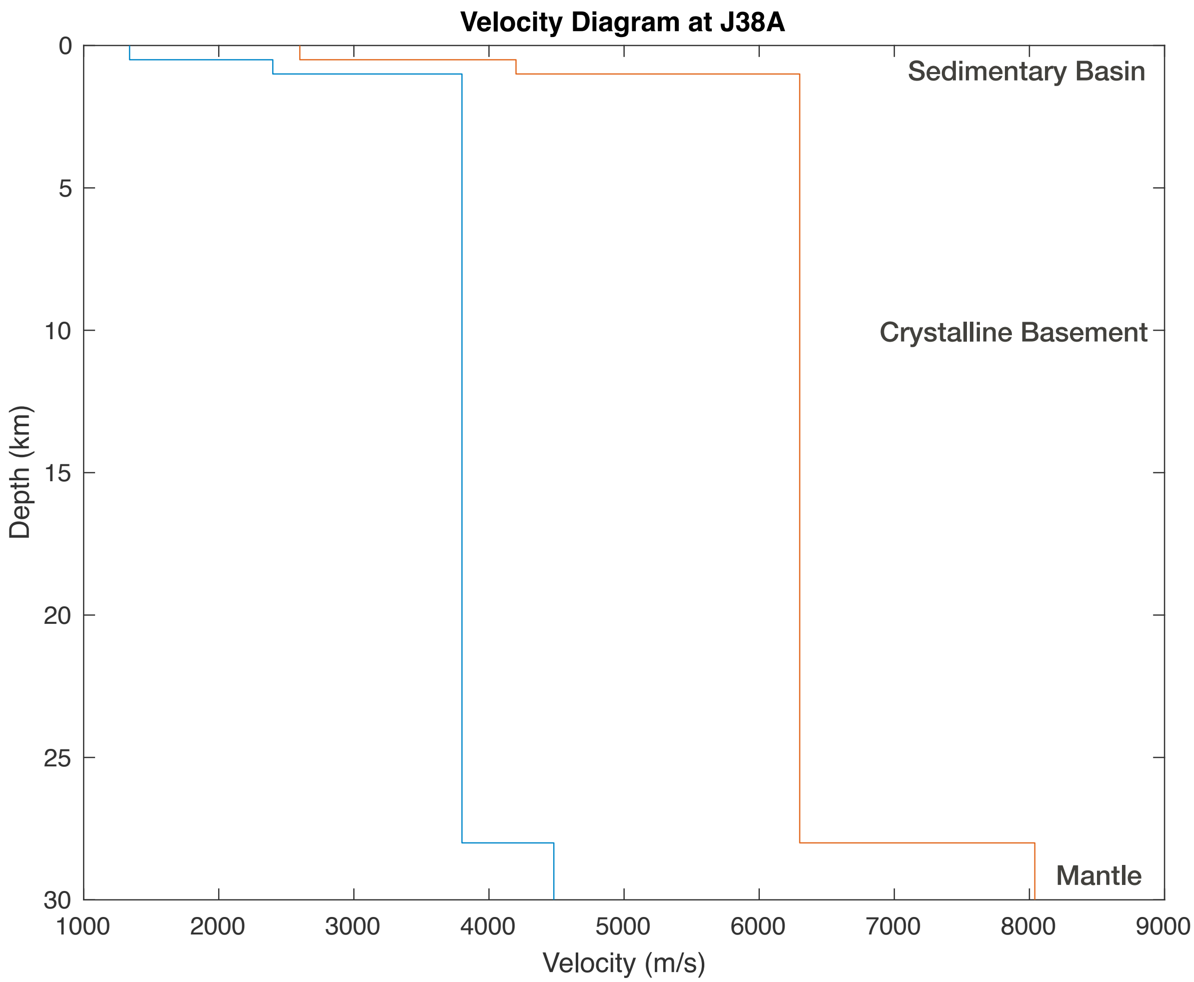

7.4 Receiver function analysis

As with EDM, RFs were stacked and analyzed with and without the layer-strip filtering. Three stations will be focused on for discussion: J38A, which had the highest quality result; E30A, which has a comparable structure but poorer result; and finally, C27A, which had the poorest result after filtering. The first station results presented here is J38A, for which layer-stripping appeared to have the most positive effect. Improvements with the filter are defined as improving the Moho and PpPs arrival without adding unwanted noise to the RF.

The results from filtering at J38A using the Crust1.0 model (TA-1) are displayed in Figure 7.4. The frequency below 2Hz content of the RFs is not greatly affected by the layer-strip below 2 Hz. The effect to the receiver function is subtle, but a noticeable improvement of the 15.4 s Moho PpPs multiple is observed. The sedimentary thickness at this station is 200 m in the Crust1.0 model, so minimal effects are to be expected. This result indicates that the layer-strip at this thickness can improve the quality of signal and produces a stable result within the frequency range of 0.05-0.5 Hz.

Figure 7.4. Frequency spectrum and stacked RFs from J38A for non-layer-stripped and layer-stripped data. Filtered using layer-strip model TA-1 taken from Crust1.0 with one sedimentary layer. Power here represents the amplitude at the corresponding frequency. RFs are band-pass filtered between 0.05-0.5 Hz.

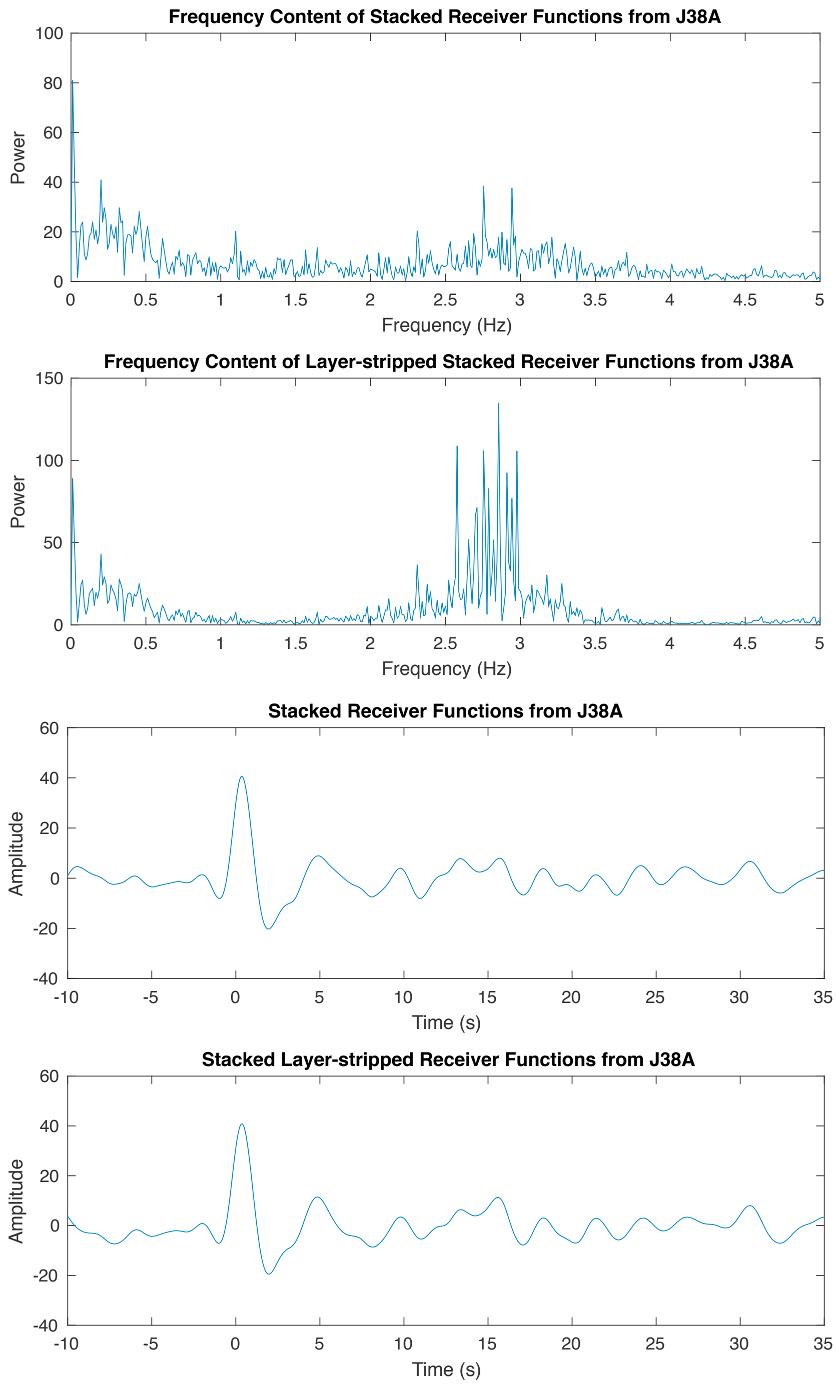

While Crust1.0 estimates the sedimentary thickness at this station to be 200 m, Frederiksen and Delaney (2015) estimated the basin thickness at 1000 m. With the sedimentary thickness larger than 700m, this station offers the opportunity to test the effect of splitting the sedimentary basin in two. To test the difference between using a 1-layer model and a 2-layer sedimentary basin model, both were used to layer-strip data from J38A. In Figure 7.5, a 1-layer 1000 m basin was used to layer-strip while in Figure 7.6 and 7.7 a 2-layer basin was used. The results from Figure 7.5 indicate that a 1-layer basin is not effective at filtering in this region, as the results are ringy and poor. The frequency content in Figure 7.5 is greatly altered, and the layer-strip is ineffective.

Figure 7.5. Frequency spectrum and stacked RFs from J38A, layer-stripped and non-layer-stripped data. Filtered using layer-strip model from Frederiksen and Delaney (2015) with one sedimentary layer. Power here represents the amplitude at the corresponding frequency. Stacked RFs are band-pass filtered between 0.05-0.5 Hz.

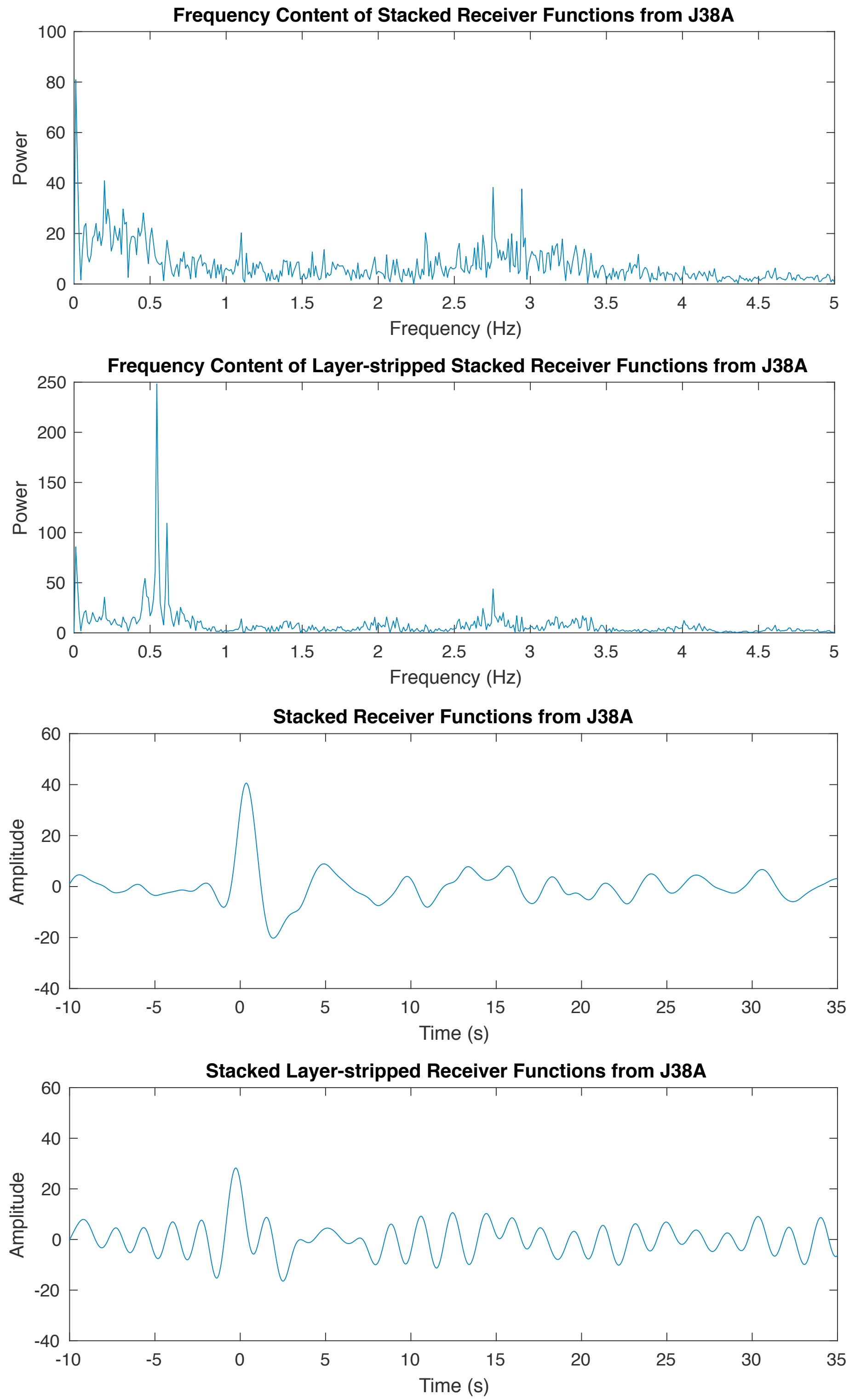

Figure 7.6. Frequency spectrum and stacked RFs from J38A for layer-stripped and non-layer-stripped data. Filtered using a layer-strip model from Frederiksen and Delaney (2015) with two sedimentary layers. Power here represents the amplitude at the corresponding frequency. RFs are band-pass filtered between 0.05-0.5 Hz.

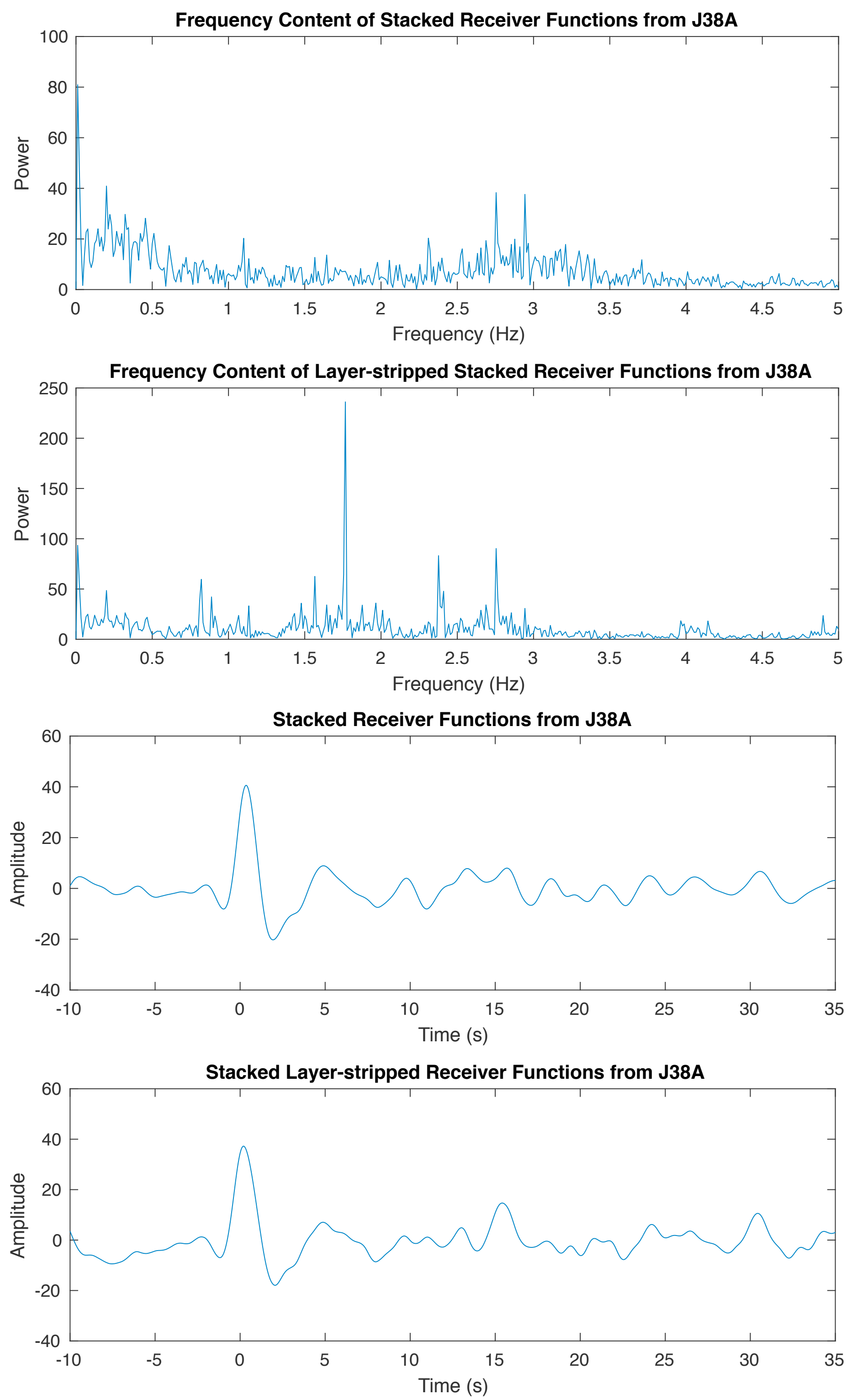

Figure 7.7. Non-layer-stripped RFs and layer-stripped RFs plotted and stacked in bins by ray parameter from J38A. These RFs were filtered using a layer-strip model TA-2 from Frederiksen and Delaney 2015 with two sedimentary layers. Both plots are band-pass filtered between 0.08-0.8 Hz.

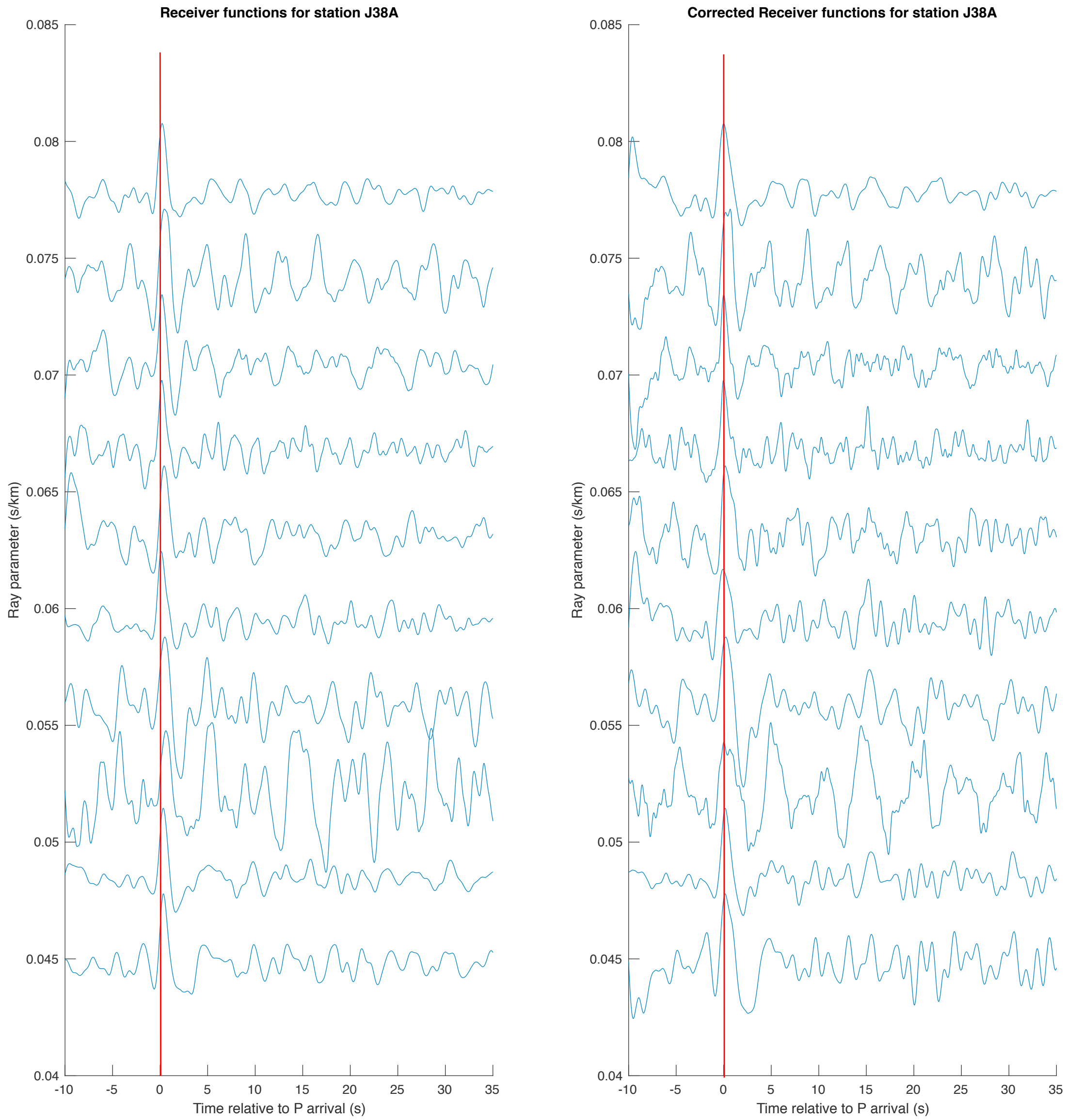

The 2-layer basin strip produced a superior result (Figure 7.6), with the frequency content mostly altered beyond 1.5 Hz, ensuring that the data is useful for receiver function analysis. This result indicates that the interface outlined in Burrus *et al*. (1996) cannot be ignored when layer-stripping this data. The effect of the layer-stripping is most dominant at 15s where the Moho reverberation arrival PpPs is predicted to be. This indicates that the layer-strip has improved the quality of data for RF analysis and has removed reverberations that were masking the Moho arrival. The arrival at 30s is also accentuated. The stacked RF appears less ringy in the lower, filtered panel. The same is true in Figure 7.7, although the effects are less apparent. At a ray parameter of 0.67 s/km there is a large improvement to the PpPs arrival.

Of the 10 stations tested in the transect, J38A had the most qualitatively effective layer-strip. It is worthwhile to also discuss other stations to determine how the layer-strip is functioning throughout the region, and at different levels of effectiveness. Station E30A is considered next.

E30A is predicted to have the same basin thickness as J38A (1 km). The stacked RF results from this station are displayed in Figure 7.8. It is clear from the results that the Crust1.0 model layer-strip had minimal effect on the RFs. The effects that are noticeable include that the first arrival is moved closer to 0s, the Moho multiple at 15s is tightened and the amplitude is increased in relative intensity. Applying the Frederiksen and Delaney (2015), where basin thickness is 1 km, the model appears to remove the Moho P to S conversion multiple at 15s. The layer-strip has failed to remove the ringing at early positive times. Although the results appear mostly stable, the layer-strip does not have a positive impact when used with the model derived using bounds taken from Frederiksen and Delaney (2015).

Figure 7.8. Stacked non-layer-stripped receiver functions and layer-stripped receiver functions from E30A. Filtered using a layer-strip model from Crust1.0 and one derived with data from Frederiksen and Delaney (2015), both models have two sedimentary layers. Band-pass filtered between 0.05-0.5 Hz.

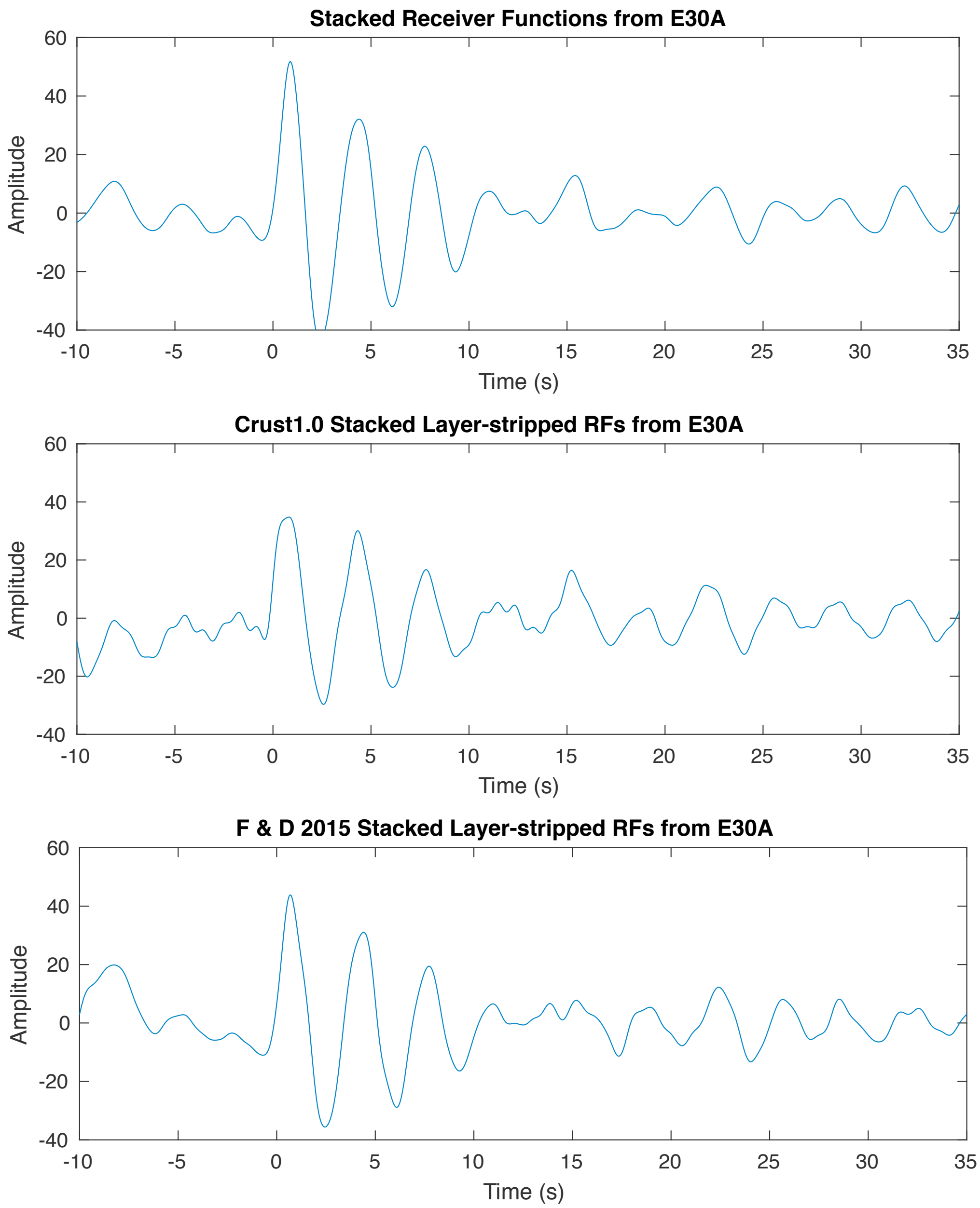

The poorest layer-strip qualitatively with either model is observed at C27A. The frequency content of non-layer-stripped and layer-stripped RFs is plotted in Figure 7.9, and the stacked RFs are displayed in Figure 7.10. The frequency content is altered within the layer-strip between 0.7 and 1 Hz such that the power is over 3 times greater than the maximum in the non-layer-stripped data. This effect on frequency is still noticeable on the RFs despite the bandpass in Figure 7.10. Using Crust1.0 to produce layer stripped RFs in Figure 7.10 caused a strong dampening of peaks and generated ringing. The stronger 25s reverberated P to S conversion is also removed from both layer-strips. The results from the two models indicate a strong dependence on sedimentary layer model quality, as the sedimentary thickness used in Crust1.0 is 3500 m, while it is 2000 m in Frederiksen and Delaney (2015). The crustal estimate in Frederiksen and Delaney (2015) is superior when comparing the resulting RFs, but is still ineffective at layer-stripping the dataset.

7.9. Frequency spectrum of stacked receiver functions from C27A for layer-stripped and non-layer-stripped data. Filtered using a layer-strip model from Frederiksen and Delaney (2015) with two sedimentary layers. Power here represents the amplitude at the corresponding frequency.

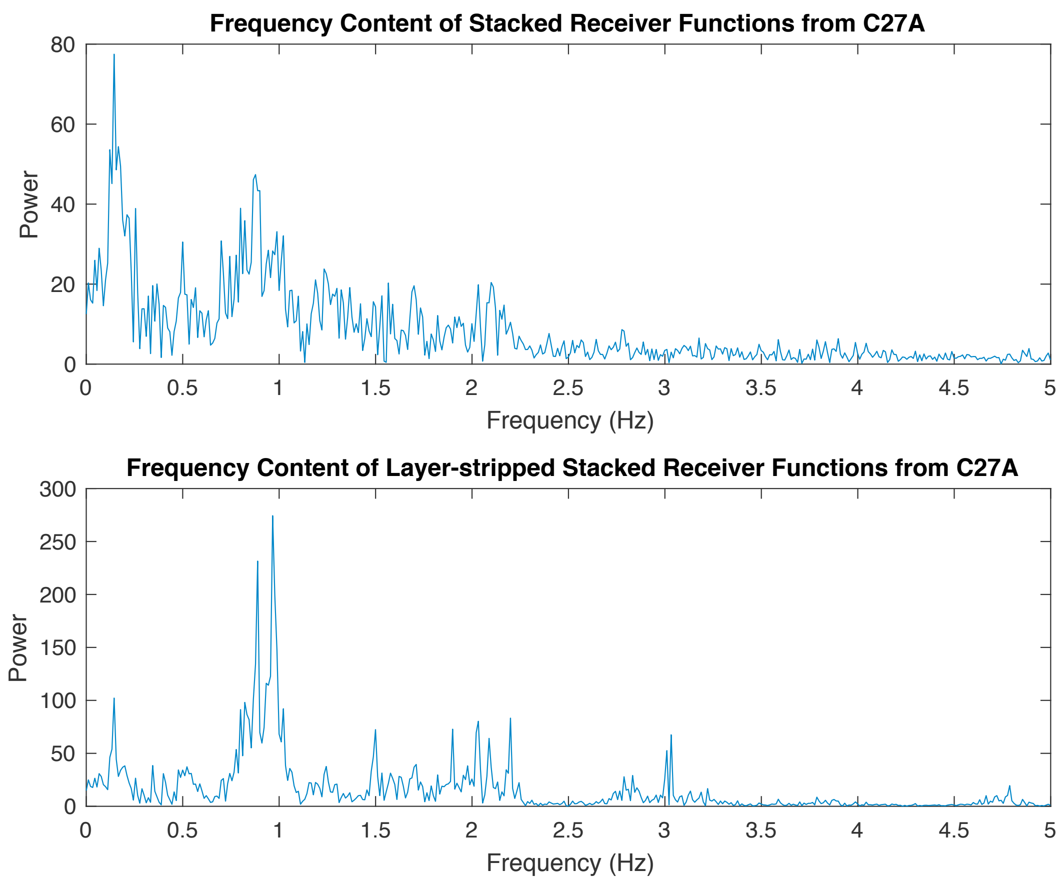

Figure 7.10. Stacked non-layer-stripped receiver functions and layer-stripped receiver functions from C27A. Filtered using a layer-strip model from Crust1.0 and one derived with data from Frederiksen and Delaney (2015), both models have two sedimentary layers. Band-pass filtered between 0.05-0.5 Hz.

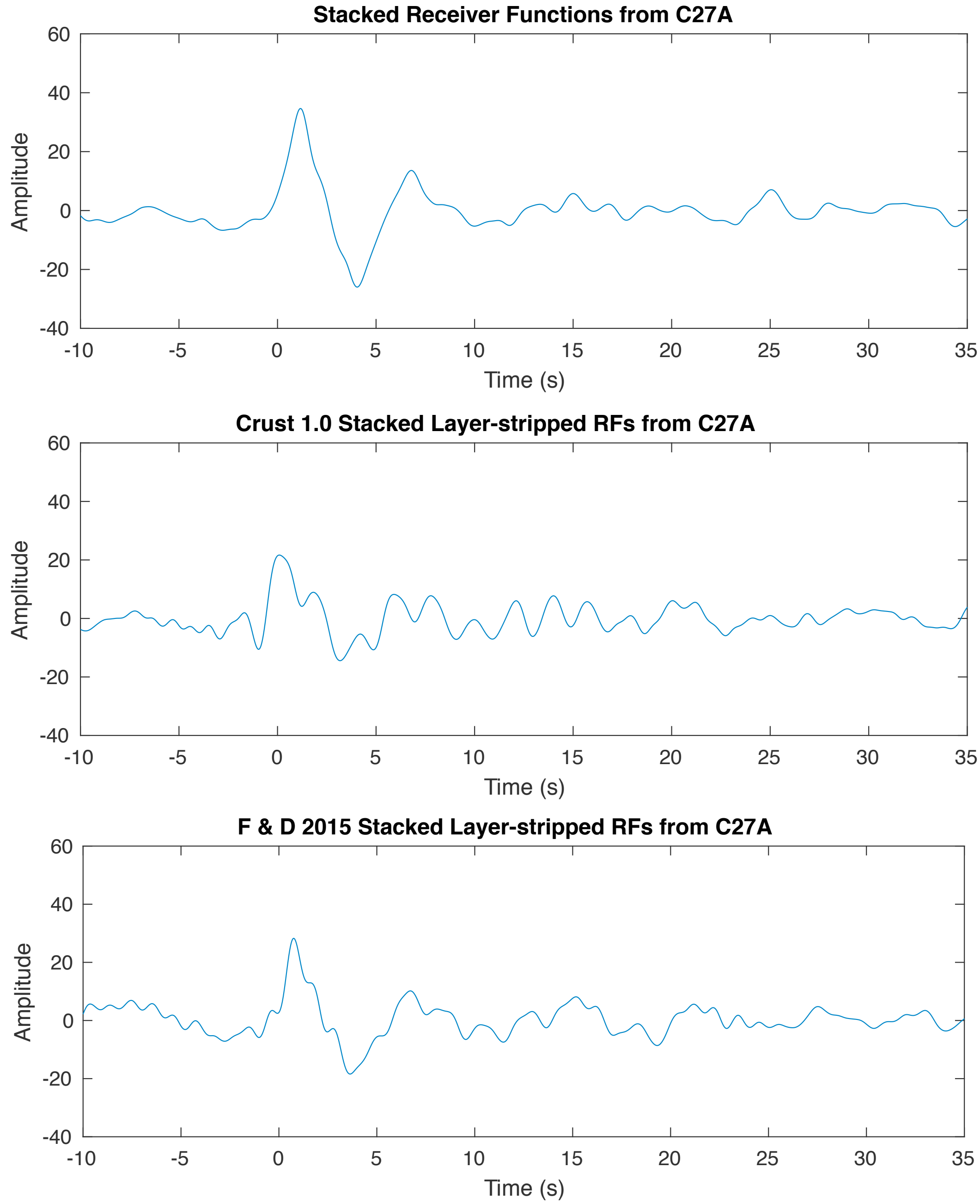

Although the effectiveness of the layer-strip is determined qualitatively, a strong correlation between the misfit from Frederiksen and Delaney (2015) and the resulting layer-stripped RFs is observed. The most effective layer-strip from the 10 stations analyzed is J38A. The misfit at this location is 0.73, the lowest of all 10 stations. The misfit calculated for J38A is substantially lower than the remaining stations. E30A has the second lowest misfit of 0.85 and the resulting RFs are stable (figure 7.8). Results from G34A indicate a positive effect; the station results are available in Appendix B Figure B.5 and are layer-stripped with a model misfit of 0.87. The highest misfit is 0.93 calculated with data from C27A, B26A and D28A. The layer-strips at these stations are the poorest, producing unstable ringing RFs. The correlation between stripped RF quality and model misfit appears to be strong through qualitative analysis. The effectiveness of the layer-strip is strongly correlated with the quality of the model, and a low misfit or high model confidence is required to remove reverberations effectively.

Only four or five of the ten stations (depending on the definition basin limits) fall within the Williston Basin. Of these stations, B26A, C27A and D28A are located within the depocenter of the basin. These stations were the poorest quality layer-strips. Station A25A is also within the basin, and an effective layer-strip took place at this station. Because there seems to be poorer results within the basin, it is possible that another effect is taking place at these sites related to the basin, in addition to reverberations. Basin amplification within the semi-sphere of the basin could be producing poorer results with the layer-strip.

7.5 H-K stacking analysis

In Chapter 3, the methodology is outlined for the H-K stack technique. This technique is used again in this chapter to produce a 4^{th} root H-K stack for each station along the Dakotas Transect from the non-layer-stripped data and layer-stripped data using models derived from Crust1.0 and Frederiksen and Delaney (2015). The H-K stack outputs an estimate for crustal thickness (H) and Vp/Vs (K), though I will focus on the crustal thickness, which is more robust. The H-K stack is performed by generating a grid of stacked receiver function amplitudes at a range of H and K, where the result is taken to be the highest stacked amplitude. The first station to be examined is J38A. Figure 7.11 displays the results of the non-layer-stripped H-K stack. The resulting crustal thickness is 36.6 km and Vp/Vs is 1.8. There are two other local maxima within the range of crustal thickness but neither reach 90% the value of stacked amplitude.

Figure 7.11. Result from 4th root H-K stack performed on non-layer-stripped data from J38A. Areas of lighter color show a higher stacked amplitude at time calculated using associated crustal thickness and Vp/Vs. The asterisk indicates highest amplitude, and isolines represent 10% amplitude change from maximum. Resulting crustal thickness is 36.6 km.

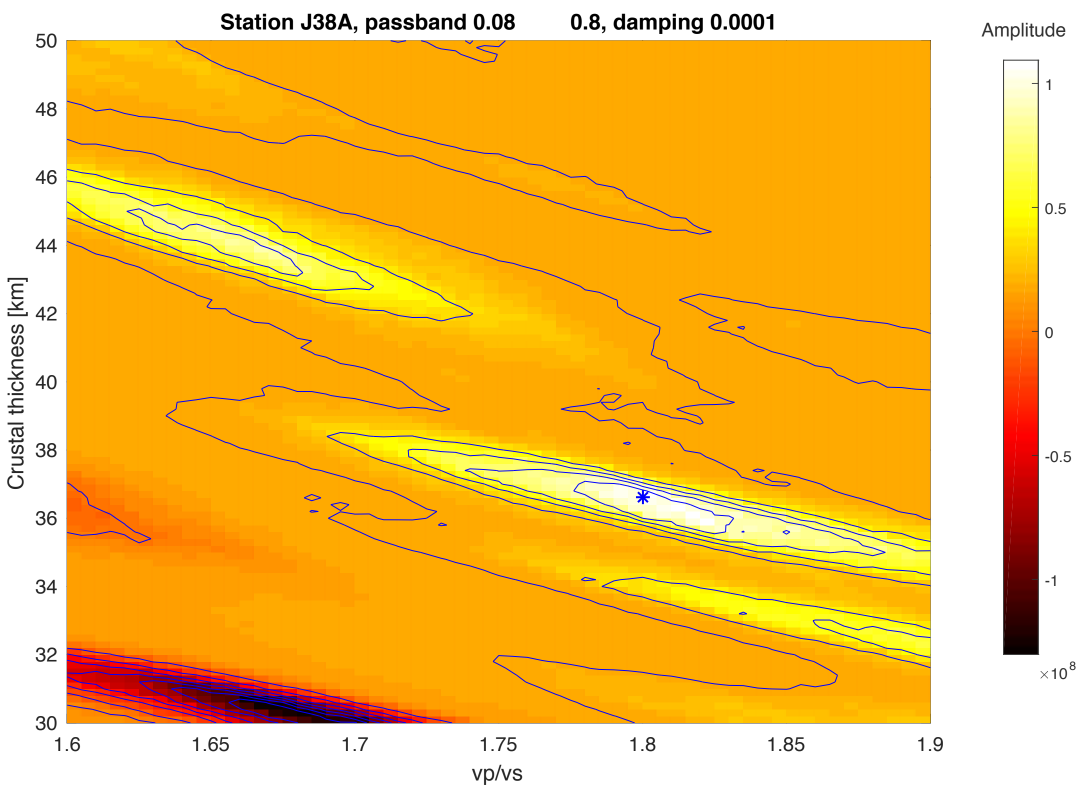

As the layer-stripping process removes the effect of the sedimentary layer that is stripped, the crustal thickness estimate is reduced. To account for this change, as in chapter 6, the travel time change was calculated, and the corresponding crustal thickness was added to the layer-stripped results. This correction does not necessarily improve the estimate, as the basin is not accounted for in the HK stack, but it is done for comparison purposes. Figure 7.12 compares the corrected crustal thickness values at each station with the non-layer-stripped crustal thickness. The H-K stack results for J38A are visualized in Figure 7.13 (Crust1.0) and Figure 7.14 (Frederiksen and Delaney, 2015). The zone size with the 90% amplitude isoline is reduced in both of these stacks, and the results are identical, 200 m thicker than the non-layer stripped results.

Figure 7.12. Resulting crustal thickness from 4th root H-K stack on non-layer-stripped data set, and layer-stripped data sets using models derived from Crust1.0 and Frederiksen and Delaney (2015). The dashed line is a plot of the 2-layer transfer function results taken directly from Frederiksen and Delaney (2015).

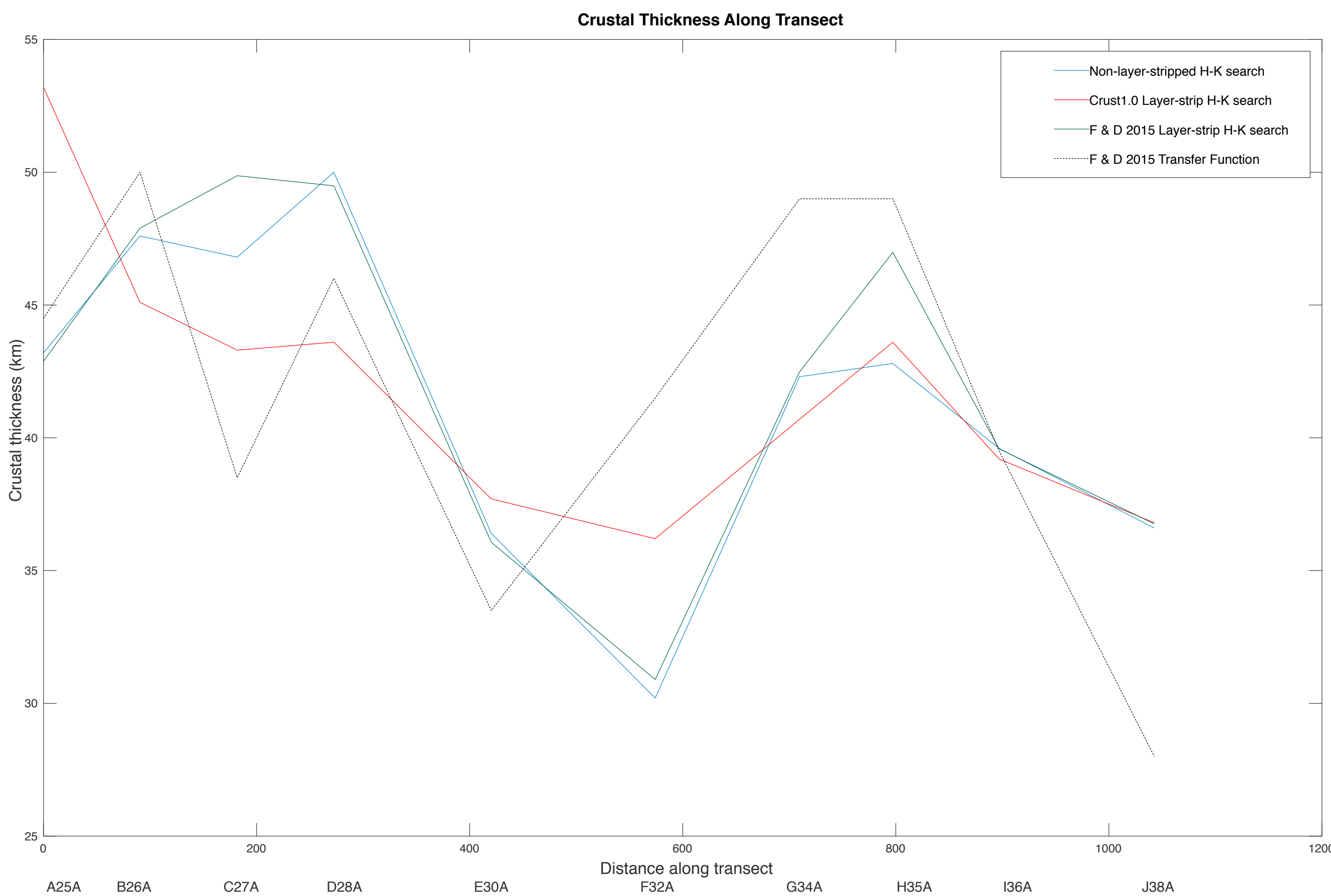

Figure 7.13. Result from 4th root H-K stack performed on layer-stripped data from J38A using Crust 1.0 model TA-1. Areas of lighter color show a higher stacked amplitude at times calculated using associated crustal thickness and Vp/Vs. Resulting crustal thickness after the correction for the stripped crust is 36.8 km.

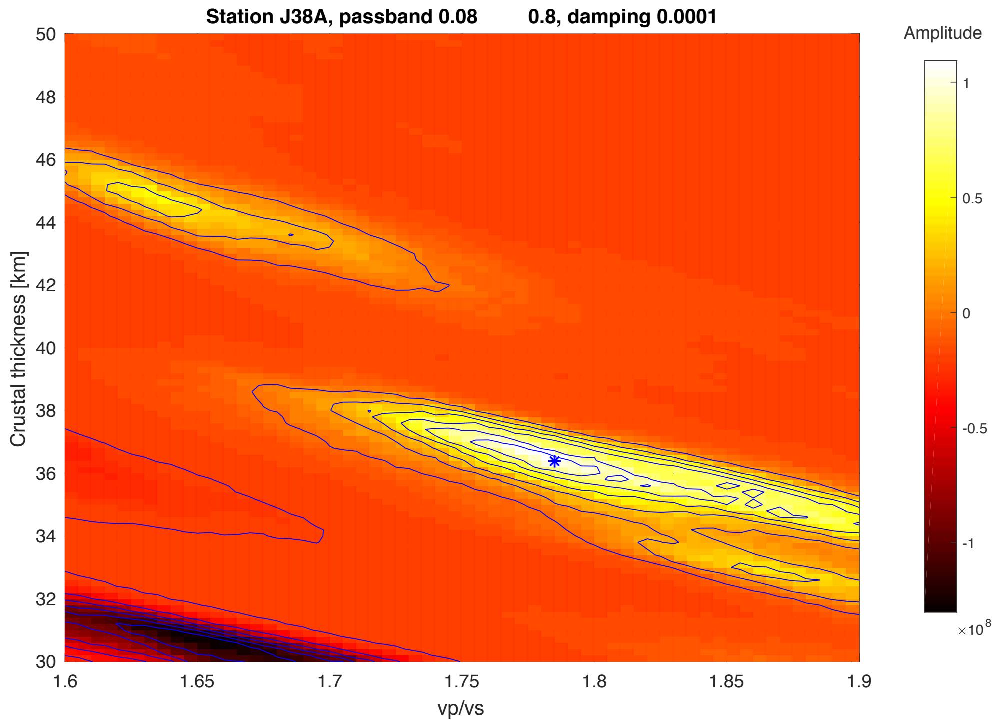

Figure 7.14. Result from 4th root H-K stack performed on layer-stripped data from J38A using TA-2 model. Areas of lighter color show a higher stacked amplitude at times calculated using associated crustal thickness and Vp/Vs. Resulting crustal thickness corrected for the stripped crust is 36.8 km.

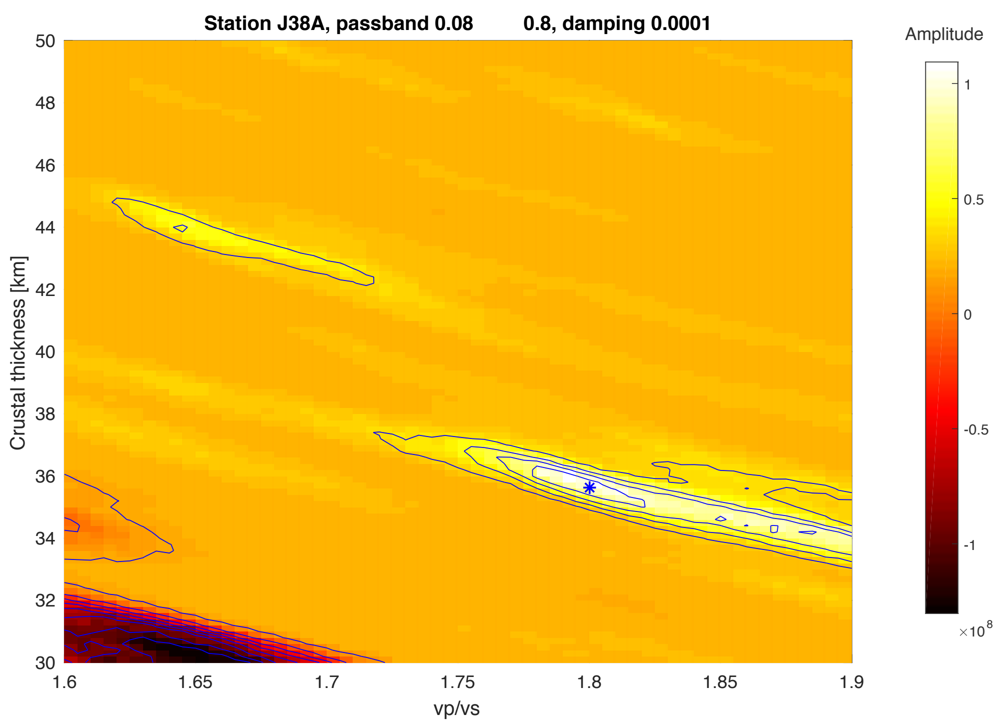

The results indicate that the solution for generating a crustal thickness of 36.8 is non-unique, as the two models used to layer-strip vary (Appendix A). It also indicates that the most effective layer-strip was completed at a station where the crust can be estimated moderately accurately without the layer-strip filter. As with EDM from Chapter 6, if the local maximum at 45 km had greater amplitude than at 36.6 km in Figure 7.11, then the layer-strip would have a large effect for the solution. When the transfer-function approach was applied to this station in Frederiksen and Delaney (2015) with a 2-layer model misfit, the resulting crustal thickness was 28 km. This same reduction in crustal thickness was not observed at this station.

The improvement in H-K stack contours (as indicated by the relative width of space within 90% isoline) means that the layer strip is making the RFs more coherent. The results from E30A show that this improvement is more prominent in the H-K stack than on unstable RFs.

Unlike J38A, E30A has a higher 2-layer misfit in Frederiksen and Delaney (2015) and poorer certainty in the crustal model. Figure 7.15 displays the H-K stack result from the non-layer-stripped data taken from E30A. The crustal thickness is estimated at 36.4 km and Vp/Vs is 1.77. The effects of the layer-strip are profound (Figure 7.16 and Figure 7.17). As with the ringy stacked RFs in Figure 7.8, the H-K stacks appear to be affected by noise introduced with the layer-strip. New local maxima are introduced in both layer-strips. The corrected crustal thickness estimate is over 1 km thicker for the Crust1.0 model over the non-layer stripped crust. It is challenging to determine which value is more accurate, but there is no strong indication that the Crust1.0 result is superior.

Figure 7.15. Result from 4th root H-K stack on non-layer-stripped data from E30A. Areas of lighter color show a higher stacked amplitude at times calculated using associated crustal thickness and Vp/Vs. Resulting crustal thickness is 36.4 km.

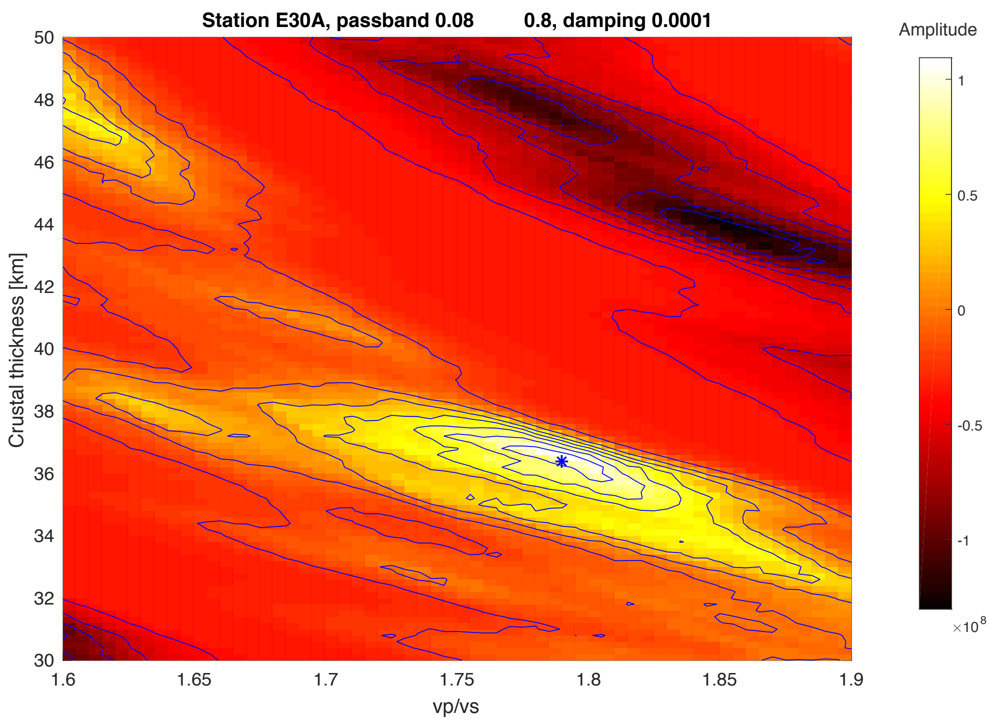

Figure 7.16. Result from 4th root H-K stack on layer-stripped data using the two sedimentary layer model TA-1 on E30A. Areas of lighter color show a higher stacked amplitude at times calculated using associated crustal thickness and Vp/Vs. Resulting crustal thickness corrected for the stripped crust is 37.6 km.

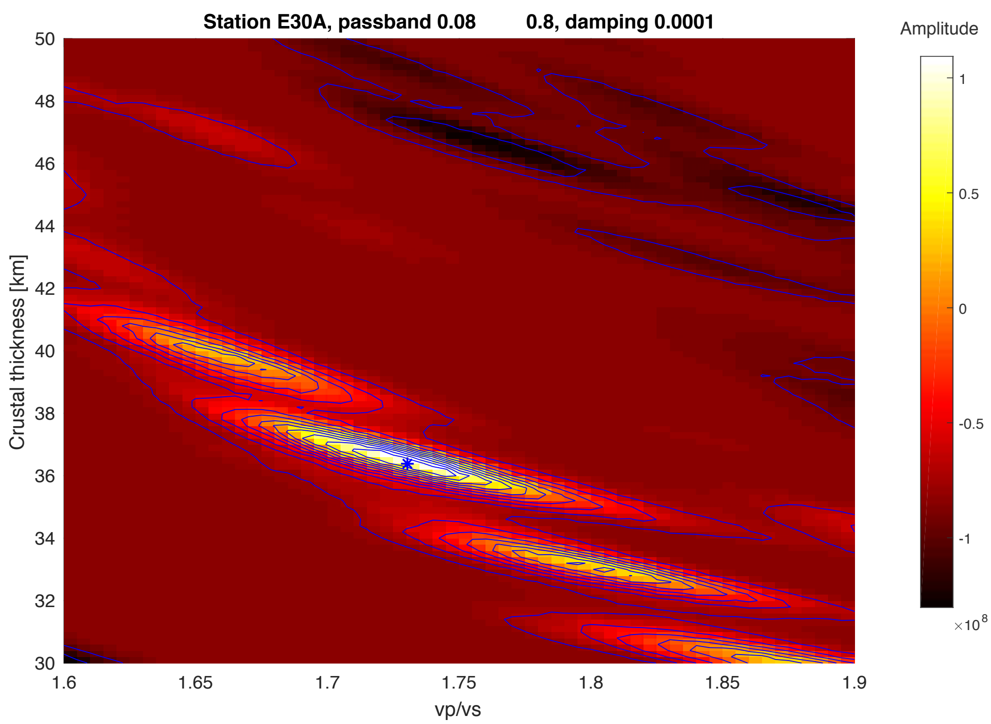

Figure 7.17. Result from 4th root H-K stack on layer-stripped data using the model TA-2 on E30A. Areas of lighter color show a higher stacked amplitude at times calculated using associated crustal thickness and Vp/Vs. Resulting crustal thickness corrected for the striped crust is 36.0 km.

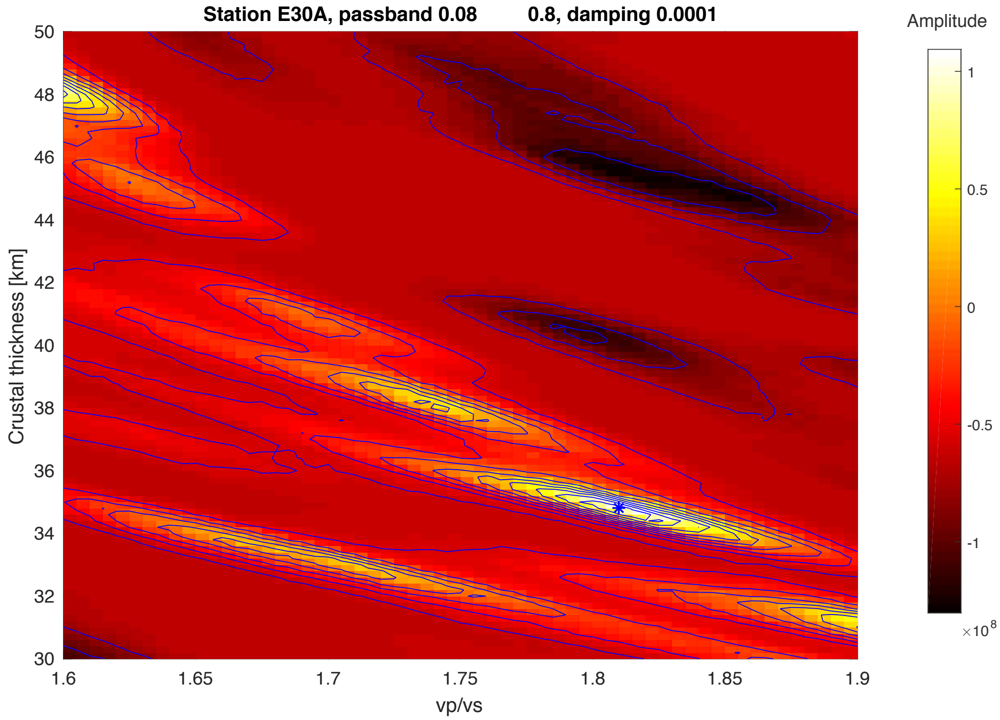

The results of the layer-strip on receiver functions from C27A (Figure 7.10) indicate that the layer-strip is ineffective on this data with both models tested. The layer-stripped and non-layer-stripped receiver functions are H-K stacked for comparison and to visualize the effects (Figure 7.18, Figure 7.19 and Figure 7.20). The corrected crustal thickness estimate is 3 km thicker using the Frederiksen and Delaney (2015) model, and 3.5 km thinner when the layer-strip is done using the Crust1.0 model. In all three of the H-K stacks, the amplitude of the peak relative to background is weaker than for previous stations. This is especially true in Figure 7.19 and Figure 7.20. This station's data indicate that the crustal thickness certainty is low, and has been made poorer by both layer-strips. The layer-strip does not appear to do anything useful if the input data are too noisy.

7.18. Result from 4th root H-K stack performed on non-layer-stripped data from C27A. Areas of lighter color show a higher stacked amplitude at times calculated using associated crustal thickness and Vp/Vs. Resulting crustal thickness is 46.8.

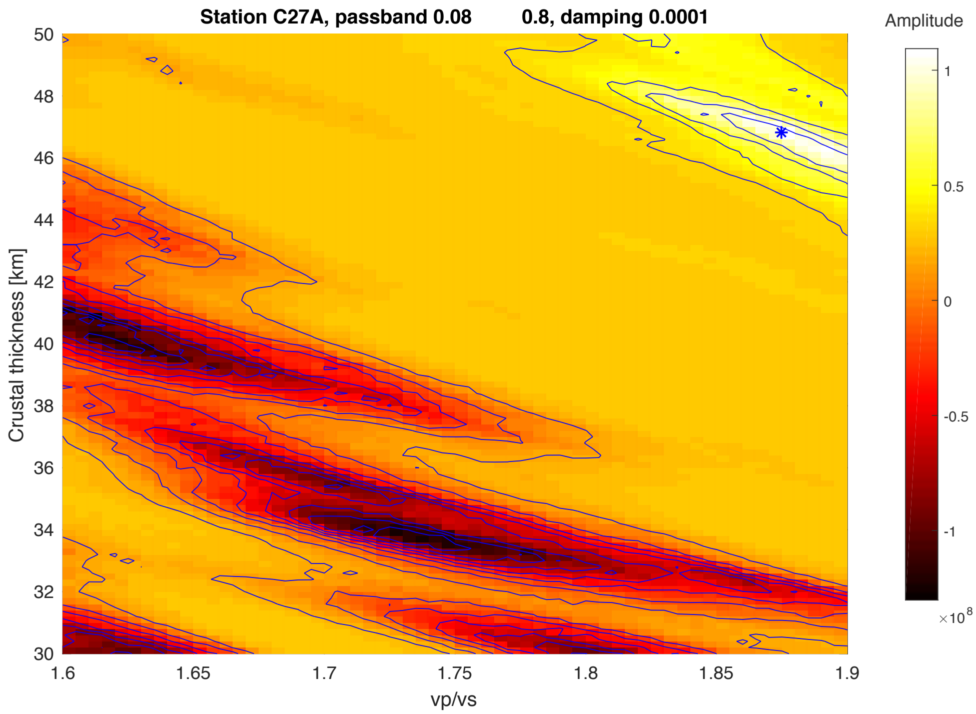

Figure 7.19. Result from 4th root H-K stack performed on layer-stripped data using the model TA-1 on C27A. Areas of lighter color show a higher stacked amplitude at times calculated using associated crustal thickness and Vp/Vs. Resulting crustal thickness corrected for the stripped crust is 43.3 km.

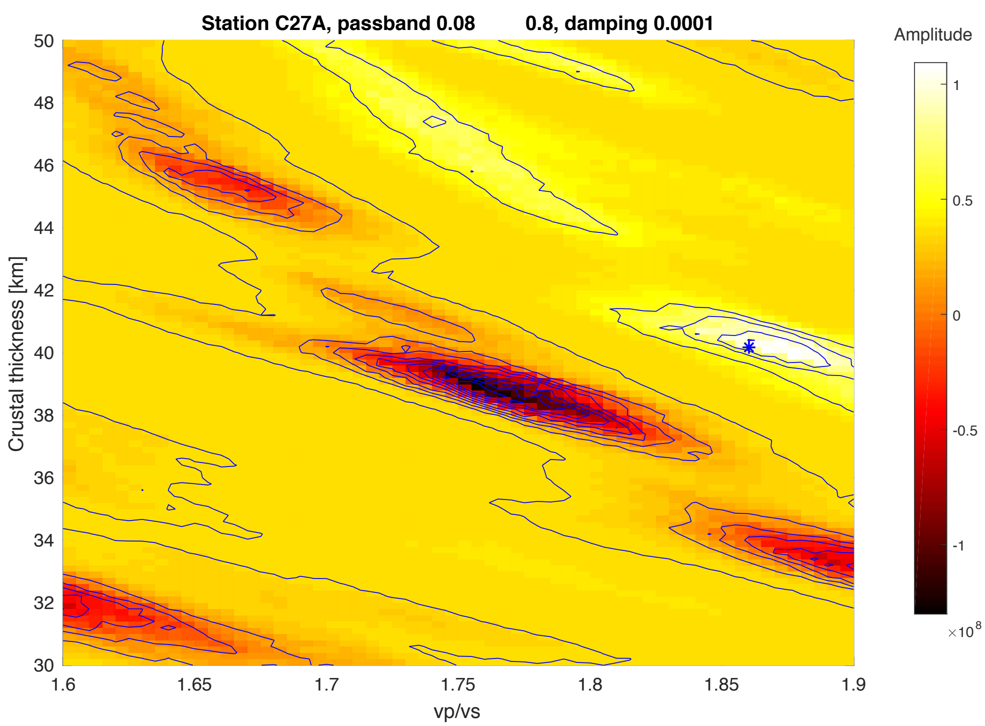

Figure 7.20. Result from 4th root H-K stack performed on layer-stripped data using model TA-2 from Frederiksen and Delaney (2015) on C27A. Areas of lighter color show a higher stacked amplitude at times calculated using associated crustal thickness and Vp/Vs. Resulting crustal thickness corrected for the stripped crust is 49.9.

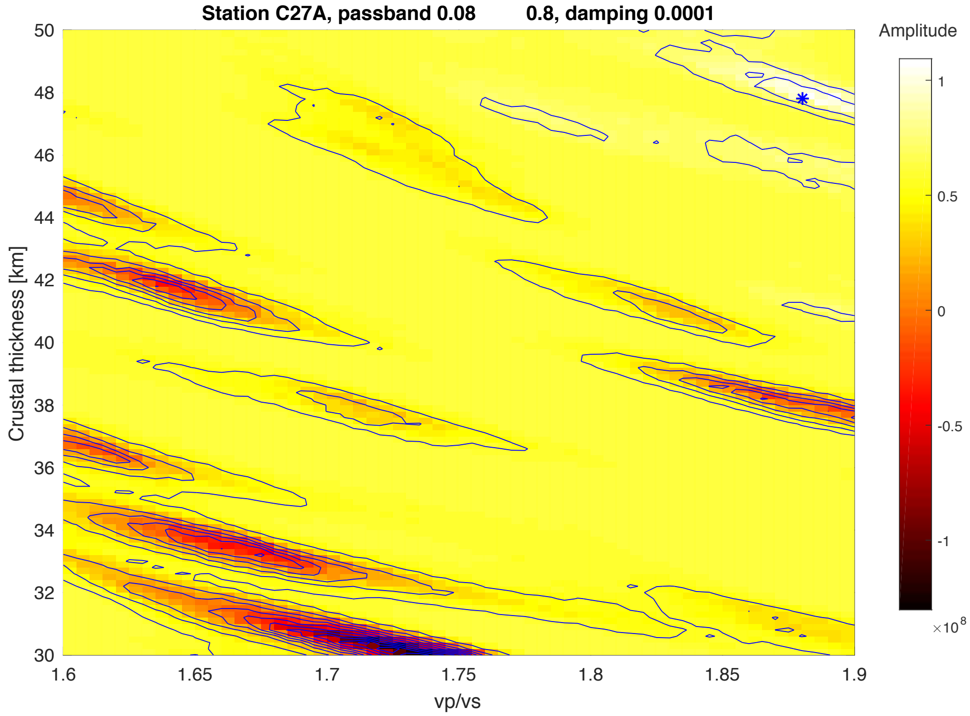

The C27A result is in line with the results of Frederiksen and Delaney (2015), in which C27A had the highest misfit of the models (along with B26A and D28A). Although the summed amplitude of the H-K estimate vs background amplitude is one indicator of a poor result, it is not sufficient in itself to determine the effectiveness of the H-K stack, the layer-strip or the data quality. It is important that the receiver functions are considered directly, as in section 7.4.

The correlation between ranking of layer-strip effectiveness and the ranking of model misfit from Frederiksen and Delaney (2015) was found to be perfect from qualitative analysis of the stacked receiver functions. The three most successful layer-strips were on J38A, G34A and E30A, all three of which had the lower 2-layer model misfit (Frederiksen and Delaney, 2015). J38A produced the best results and had a misfit of 0.73, while C27A produced the worst results and had a misfit of 0.93. More accurate models not only produce a better layer-strip filter, but also determine whether the layer-strip filter improves receiver functions or is detrimental, adding ringing noise (Figure 7.10).

Interestingly, the correlation coefficient between 2-layer misfit at the ten stations from Frederiksen and Delaney (2015) and the change in crustal thickness estimate after layer-stripping is 0.0537. This indicates that a higher model misfit does not directly lead to a spurious change in crustal thickness estimate.

Unlike for the stacked receiver functions, it is less obvious whether the effects are positive or negative pre and post layer-strip filtering in the H-K stack plots. The two main indicators of the effect, outside the H and K output, are the area of the 90th percentile isoline, and the amplitude difference between the maximum and background. Although these effects indicate that the certainty may be improved for J38A and E30A, and reduced for C27A, it is necessary to assess the filtering effects on the receiver function and estimate the accuracy of the layer-strip model while completing layer-stripping.

Comparing the changes in crustal thickness in Figure 7.12, in general, the layer-stripping from Frederiksen and Delaney (2015) models had a smaller effect on corrected crustal thickness than Crust1.0 models. Overall, the consistency between models was moderate to poor (Figure 7.12). This indicates that the certainty of the layer-strip model must be high before the result can be trusted.

It is also likely that ineffective layer-stripping takes place due to compounding effects. The major cause is expected to be a poor basin model, but other sources of complexities may add to the poor layer-strip results. These effects could include crustal complexities that can obscure the Moho arrivals, or a weaker velocity interface at the Moho discontinuity producing weaker conversions. The technique may also require more detailed models in areas where strong reverberations are produced in a structure with more than two dominant layers.

The major conclusions drawn from this chapter and the analysis of layer-stripping the Earthscope TA data include the following. Firstly, sediment thickness and model misfit do not appear to be correlated in results obtained from Frederiksen and Delaney (2015). Second, two greatly different basin models were used successfully to layer-strip Station J38A. Thirdly, another model with a 1-layer basin, 1 km in thickness, generated an extremely poor result at J38A. Breaking the basin into two layers based on geophysical and geological sources greatly improved the result. This indicates that model accuracy is very important with thicker sediment layer-stripping. Finally, it is concluded that the ranked result of the layer-strip matches the rank of model misfit from the model used to produce the layer-strip.

These results show that layer-stripping can work under circumstances in which model certainty is high. At EDM the results were better, likely due to the longer data record and improved SNR. More data is likely also to be included in Crust1.0 at this location, offering a better model. The Williston Basin stations are generally noisier, and data was only collected over a period of 3 years. Unfortunately, assessing the result of the layer-strip with respect to the change in analytical outcome, such as crustal thickness, is a challenge. This is especially important when different models used to layer-strip can affect the resulting crustal thickness by 10 km (Figure 7.12).

Chapter 8. Conclusions

The main objective of this project was to test the effectiveness of the layer-stripping methodology on teleseismic data collected over sedimentary basins. First, synthetic data were generated and layer-stripped to assess the methodology under stringent conditions. Data from the CNSN at EDM and Earthscope TA at an array of stations transecting the Williston Basin were layer-stripped to further test the methodology.

The synthetic test shows that the propagator method is effective at generating data that includes reverberations from sedimentary layers. The modelled synthetic data also indicate that later structural arrivals are masked by the reverberations as expected. Layer-stripping the synthetic data led to the conclusion that the methodology can be effective, even with imperfect models. Finally, it can be concluded from the synthetic tests that the basin model may need to be accurate within as little as 100 m, while the lower crustal model is less important.

Layer-stripping for EDM data shows that the signal to noise ratio is improved and reverberations are removed after the filter is applied. After the strip, the H-K stack had improved resolution. Importantly, secondary local maxima at similar amplitudes to the regional amplitude maxima were removed from the grid search results. These maxima are likely to be associated with reverberations. Determining if the change to crustal thickness and Vp/Vs with layer-stripping is trustworthy is a challenge, despite the positive effects observed.

Generally, the results from layer-stripping the Williston Basin transect were poorer than from EDM. This is concluded to be caused by poorer data and model certainty at many of the Williston Basin TA stations. The Williston Basin transect results demonstrate the importance of model quality. At station J38A, an effective layer-strip was performed with a 2-layer sedimentary structure, while the same strip degraded the receiver functions when 1 sedimentary layer was used. From this result, it is concluded that models must be accurate to be effective, and so should use all available geologic information. The correlation between model misfit from Frederiksen and Delaney (2015) and ranked layer-strip effectiveness is perfect. This indicates that, as expected, the quality of filter is dependent on the quality of model.

The limitations of these results are focused around the challenge to determine when it is appropriate to use the layer-strip filtering technique, and when the outcome of the filter can be considered an improvement. For example, it is not clear which changes to crustal thickness estimates, after layer-stripping the TA data, are correct. The challenge of assessing the effectiveness versus model accuracy is accentuated by the lack of transparency in Crust1.0 data. While these data are very useful in generating models, information is not available on how many lines of evidence were used to produce them. It appears that the layer-strip methodology can only be used confidently when multiple lines of evidence exist for a model, such as geological constraints and active source seismic studies. This mitigates model uncertainty being mapped into receiver function data.

Future work on this topic should focus on completing more tests in areas of sedimentary structure certainty. From here, more examples of when the layer-strip filter can be used confidently will improve the overall confidence of the technique. This filtering methodology may also prove useful in other areas of seismology including seismic research over ice, and in marine settings. Testing the layer-strip filter on these data sets could be completed as a separate research project.

References

Aki, K., and Richards, P. G. (2002): Quantitative Seismology; *University Science Books,* Sausalito, California, Pages 157-161.

Ammon, C. J. (1991): The isolation of receiver effects from teleseismic P waveforms; *Bulletin Seismological Society of America*, Volume 81, Pages 2504–2510.

Ammon, C.J., Randall, G. E., and Zandt, G. (1990): On the nonuniqueness of receiver function inversions; *Journal of Geophysical Research*, Volume 95, No. B10, Pages 15303-15318.

Audet, P. (2016): Receiver functions using OBS data: Promises and limitations from numerical modelling and examples from the Cascadia Initiative; *Geophysics Journal International,* Volume 205, No. 3, Pages 1740-1755.

Baird, D.J., Knapp, J.H., Steer, D.N., Brown, L.D., and Nelson, K.D. (1995): Upper-mantle reflectivity beneath the Williston basin, phase-change Moho, and the origin of intracratonic basins; *Geology*, Volume 23, No. 5, Pages 431-434.

Baker, G.E., Minster, J. B., Zandt, G., Gurrola, H. (1996): Constraints on Crustal Structure and Complex Moho Topography beneath Pinon Flat, California, from Teleseismic Receiver Functions; *Bulletin of the Seismological Society of America,* Volume 86, No. 6, Pages 1830-1844.

Bayrock, L. A., and Berg, T. E. (1966): Geology of the city of Edmonton Part 1: Central Edmonton; *Research Council of Alberta,* Report 66-1, Pages 1-30.

Boore, M. D., Larner, K. L., and Aki, K. (1971): Comparison of two independent methods for the solution of wave-scattering problems: response of a sedimentary basin to vertically incident SH waves; *Journal of Geophysical Research,* Volume 76, No. 2, Pages 558-569.

Burrus, J., Osadetz, K., Wolf, S., Doligez, B., Visser, K., and Dearborn, D. (1996): A two-dimensional regional basin model of Williston Basin hydrocarbon systems; *AAPG Bulletin*, Volume 80, No. 2, Pages 265-291.

Cassidy, J. F. (1992): Numerical experiments in broadband receiver function analysis; *Bulletin of the Seismological Society of America,* Volume 82, No. 3, Pages 1453-1474.

Cassidy, J.F. (1995): A comparison of the receiver structure beneath stations of the Canadian National Seismograph Network; *Canadian Journal of Earth Science,* Volume 32, Pages 938-951.

Clayton, R.W., Wiggins, R.A. (1976): Source shape estimation and deconvolution of teleseismic bodywaves; *Geophysics Journal International*, Volume 47, Issue 1, Pages 151-177.

Clitheroe, G., Gudmundsson, O., and Kennett B. L. N. (2000): Sedimentary and upper crustal structure of Australia from receiver functions; *Australian Journal of Earth Sciences,* Volume 47, No. 2, Pages 209-216.

Crotwell, H. P., and Owens, T. J. (2005): Automated receiver function processing; *Seismological Research Letters*, Volume 76, No. 6, Pages 702-709.

Crotwell, H. P., Owens, T. J., and Ritsema, J. (1999): The TauP Toolkit: Flexible seismic travel- time and ray-path utilities, *Seismological Research Letters*, Volume 70, Pages 154–160.

Eaton, D., W., Dineva, S., and Mereu, R. (2006): Crustal thickness and Vp/Vs variations in the Grenville orogen (Ontario, Canada) from analysis of teleseismic receiver functions; *Tectonophysics*, Volume 420, Pages 223-238.

Fontaine, F. R., Tkalcic, H., and Kennett, B. L. N. (2013): Crustal complexity in the Lachlan Orogen revealed from teleseismic receiver functions; *Australian Journal of Earth Sciences,* Volume 60, Issue 3, Pages 413-430.

Frederiksen, A. W., and Delaney, C. (2015): Deriving crustal properties from the P Coda without deconvolution: the southwestern Superior Province, North America; *Geophysics Journal International*, Volume 201, Pages 1491-1506.

Gerhard, L. C., Anderson, S. B., and LeFever, J. A. (1991): Petroleum geology of the Williston basin, in H. W. Leighton: Interior cratonic basins; *AAPG Memoir,* Issue 34, Chapter 29, Pages 507–559.

Gibbs, A.K., Payne, B., Setzer, T., Brown, L.D., Oliver, J.E., and Kaufman, S. (1984): Seismic-reflection study of the Precambrian crust of central Minnesota; *Geological Society of America Bulletin,* Volume 95, Pages 280-294.

Haskell, N. A. (1962): Crustal reflection of plane P and SV waves; *Journal of Geophysical Research*, Volume 67, No. 12, Pages 4751-4767.

Jensen, O.G., and Ellis, R.M. (1970): Wave propagation in a horizontally-layered crust in terms of linear system theory; *Canadian Journal of Earth Sciences*, Volume 7, Issue 5, Pages 1185-1193.

Julià J., Assumpção, M., and Rocha, M. P. (2008): Deep crustal structure of the Paraná Basin from receiver functions and Rayleigh-wave dispersion: Evidence for a fragmented cratonic root; *Journal of Geophysical Research,* Volume 113, Issue B8, Pages 1-23.

Kent, D.M., and Christopher, J.E. (1994): Geological history of the Williston Basin and Sweetgrass Arch; in Geological Atlas of the Western Canada Sedimentary Basin, G.D. Mossop, I. Shetsen (comp.); *Canadian Society of Petroleum Geologists and Alberta Research Council*, Chapter 27, Pages 421-429.

Langston, C. A. (1977): The effect of planar dipping structure on source and receiver responses for constant ray parameter; *Bulletin of Seismology Society of America*, Volume 67, Pages 1029-1050.

Langston, C. A. (1979): Structure under Mount Rainier, Washington, inferred from teleseismic body waves*; Journal of Geophysical Research*, Volume 84, Pages 4749–4762.

Langston, C. A. (2011): Wave-field continuation and decomposition for passive seismic imaging under deep unconsolidated sediments; *Bulletin Seismological Society of America*, Volume 101, Pages 2176–2190.

Laske, G., Masters, G., Ma, Z., and Pasyanos, M. (2013): Update on CRUST1.0 – a 1-degree global model of Earth's crust; *European Geosciences Union,* General Assembly 2013 Geophysical Research Abstracts, Volume 15, EGU2013-2658.

Leahy, G. M., R. L. Saltzer, and J. Schmedes (2012): Imaging the shallow crust with teleseismic receiver functions; *Geophysical Journal International*, Volume 191, Pages 627–636.

Mandal, P. (2006): Sedimentary and crustal structure beneath Kachchh and Saurashtra regions, Gujarat, India; *Physics of the Earth and Planetary Interiors,* Volume 155, Issue 3-4, Pages 286-299.

Natural Resources Canada (2016): Introduction to the Canadian National Seismograph Network, available at: http://www.earthquakescanada.nrcan.gc.ca/stndon/CNSN-RNSC/, (last accessed 12 November 2017).

NCEDC (2016): Northern California Earthquake Data Center; *UC Berkeley Seismological Laboratory*, Dataset, available at: http://www.ncedc.org/anss/catalog-search.html, (last accessed July 4, 2016).

Nelson, K.D., Baird, D.J., Walters, J.J., Hauck, M., Brown, L.D., Oliver, J.E., Ahern, J.L., Hajnal, Z., Jones, A.G., and Sloss, L.L. (1993): Trans-Hudson orogen and Williston basin in Montana and North Dakota: New COCORP deep-profiling results; *Geology*, Volume 21, Pages 447-450.

Owens, T. J., G. Zandt, and S. R. Taylor (1984): Seismic evidence for an ancient rift beneath the Cumberland Plateau, Tennessee: A detailed analysis of broadband teleseismic P waveforms; *Journal of Geophysical Research*, Volume 89, Pages 7783–7795.

Porter, J. W., Price, R. A., McCrossan, and R. G. (1982): The Western Canada Sedimentary Basin; *Philosophical Transactions of the Royal Society of London*; Volume 305, Pages 169-192.

Prior, G.J., Hathway, B., Glombick, P.M., Pană, D.I., Banks, C.J., Hay, D.C., Schneider, C.L., Grobe, M., Elgr, R. and Weiss, J.A. (2013): Bedrock geology of Alberta; Alberta Energy Regulator, AER/AGS Map 600, scale 1:1 000 000.

Reed, C. A., S. Almadani, S. S. Gao, A. Elsheikh, S. Cherie, M. Abdelsalam, A. Thurmond, and K. H. Liu (2014): Receiver function constraints on crustal seismic velocities and partial melting beneath the Red Sea rift and adjacent regions, Afar Depression; *Journal of Geophysical Research: Solid Earth*, Volume 119, Pages 2138–2152.

Salah, M., Chang, S., and Fonseca, F.J. (2011): Crustal structure beneath the Lower Tagus Valley, southwester Iberia using joint analysis of teleseismic receiver functions and surface-wave dispersion; *Geophysics Journal International*, Volume 184, Issue 2, Pages 919-933.

Sheehan, A. F., Abers, G. A., Jones, C. H., and Lerner-Lam, A. L. (1995): Crustal thickness variations across the Colorado Rocky Mountains from Teleseismic receiver functions; *Journal of Geophysical Research,* Volume 100, No. B10, Pages 20391-20404.

Shen, W., Michael, H. R., and Schulte-Pelkum, V. (2013): Crustal and uppermost mantle structure in the central U.S. encompassing the Midcontinent Rift; *Journal of Geophysical Research: Solid Earth,* Volume 118, Pages 4325-4344.

Siddiqqi, J., and Atkinson, G. M. (2002): Ground-motion amplification at rock sites across Canada as determined from the horizontal-to-vertical component ratio; *Bulletin of the Seismological Society of America,* Volume 92, No. 2, Pages 877-884.

Somerville, P. G., and Ellis, R. M. (1972): P-coda evidence for a layer of anomalous velocity in the crust beneath Leduc, Alberta; *Canadian Journal of Earth Sciences,* Volume 9, Pages 845-856.

Tao, K., Liu, T. Z., Ning, J. Y., and Niu, F. (2014): Estimating sedimentary and crustal structure using wavefield continuation: Theory, techniques and applications; *Geophysical Journal International*, Volume 197, Pages 443–457.

Thomson, W. T. (1950): Transmission of elastic waves through a stratified solid medium; *Journal of Applied Physics,* Volume 21, Pages 88-93.

Williams, M.L., Fischer, K.M., Freymueller, J.T., Tikoff, B., and Tréhu A.M. (2010): Unlocking the secrets of the North American Continent: An EarthScope science plan for 2010–2020, Pages 1-78, available at: www.earthscope.org/assets/uploads/pages/es_sci_plan_hi.pdf (last accessed November 18, 2017).

Yeck, W. L., A. F. Sheehan, and V. Schulte-Pelkum (2013): Sequential H-k stacking to obtain accurate crustal thicknesses beneath sedimentary basins; *Bulletin Seismological Society of America*, Volume 103, Pages 2142–2150.

Yu, Y., Song, J., Liu, K. H., and Gao, S. (2015): Determining crustal structure beneath seismic stations overlying a low-velocity sedimentary layer using receiver functions: Receiver Function Crustal Study; *Journal of Geophysical Research: Solid Earth*, Volume 120, Issue 5, Pages 3208-3218.

Yuan, H., Dueker, K., and Stachnik, J. (2010): Crustal structure and thickness along the Yellowstone spot track: Evidence for lower crustal outflow from beneath the eastern Snake River Plain; *G^3 Geochemistry, Geophysics, Geosystems*, Volume 11, Pages 1-14.

Zandt, G., and Ammon, C. J. (1995): Continental crust composition constrained by measurements of crustal Poisson's ratio; *Nature*, Volume 374, Pages 152–154.

Zelt, B. C., and Ellis R. M. (1999): Receiver-function studies in the Trans-Hudson Orogen, Saskatchewan; *Canadian Journal of Earth Sciences,* Volume 36, Pages 585-603.

Zelt, C.A., and Ellis, R.M. (1989): Seismic structure of the crust and upper mantle in the Peace River Arch region, Canada; *Journal of Geophysical Research,* Volume 94, Pages 5729-5744.

Zhu, L., and Kanamori, H. (2000): Moho depth variation in Southern California from teleseismic receiver functions*; Journal of Geophysical Research*, Volume 105, Pages 2969–2980.

Appendix

A. Seismic models for 10 TA stations

Table A.1. Seismic model TA-1 (taken directly from Crust1.0) for station A25A. All velocities are in m/s, density in kg/m^3 and depth in m. Sedimentary layers highlighted in pale yellow.

A25A	1	2	3	4	5	6
VelS	1070	2740	3600	3700	3900	4560
VelP	2500	4800	6200	6400	6800	8230
Dens	2110	2500	2760	2810	2910	3390
Depth to boundary	1000	4400	19990	35580	51640	

Table A.2. Seismic model TA-2 (partially derived from Frederiksen & Delaney 2015) for station A25A. All velocities are in m/s, density in kg/m^3 and depth in m. Sedimentary layers highlighted in pale yellow.

A25A	1	2	3	4
VelS	1340	2400	3800	4480
VelP	2600	4200	6300	8040
Dens	2200	2400	2900	3600
Depth to boundary	700	2000	44000	

Table A.3. Seismic model TA-1 (taken directly from Crust1.0) for station B26A. All velocities are in m/s, density in kg/m^3 and depth in m. Sedimentary layers highlighted in pale yellow.

B26A	1	2	3	4	5	6
VelS	1070	2740	3600	3700	3900	4490
VelP	2500	4800	6200	6400	6800	8090
Dens	2110	2500	2760	2810	2910	3330
Depth to boundary	1000	3900	18540	33190	48270	

Table A.4 Seismic model TA-2 (partially derived from Frederiksen & Delaney 2015) for station B26A. All velocities are in m/s, density in kg/m^3 and depth in m. Sedimentary layers highlighted in pale yellow.

B26A	1	2	3	4
VelS	1340	2400	3800	4480
VelP	2600	4200	6300	8040
Dens	2200	2400	2900	3600
Depth to boundary	700	2000	50000	

Table A.5. Seismic model TA-1 (taken directly from Crust1.0) for station C27A. All velocities are in m/s, density in kg/m³ and depth in m. Sedimentary layers highlighted in pale yellow.

C27A	1	2	3	4	5	6
VelS	1070	2740	3600	3700	3900	4470
VelP	2500	4800	6200	6400	6800	8050
Dens	2110	2500	2760	2810	2910	3320
Depth to boundary	1000	3500	20020	36550	53570	

Table A.6. Seismic model TA-2 (partially derived from Frederiksen & Delaney 2015) for station C27A. All velocities are in m/s, density in kg/m³ and depth in m. Sedimentary layers highlighted in pale yellow.

C27A	1	2	3	4
VelS	1340	2400	3800	4480
VelP	2600	4200	6300	8040
Dens	2200	2400	2900	3600
Depth to boundary	700	2000	38500	

Table A.7. Seismic model TA-1 (taken directly from Crust1.0) for station D28A. All velocities are in m/s, density in kg/m³ and depth in m. Sedimentary layers highlighted in pale yellow.

D28A	1	2	3	4	5	6
VelS	1070	2740	3530	3710	3930	4480
VelP	2500	4800	6100	6500	6900	8070
Dens	2110	2500	2740	2830	2920	3330
Depth to boundary	1000	2700	16940	32950	47190	

Table A.8. Seismic model TA-2 (partially derived from Frederiksen & Delaney 2015) for station D28A. All velocities are in m/s, density in kg/m³ and depth in m. Sedimentary layers highlighted in pale yellow.

D28A	1	2	3	4
VelS	1340	2400	3800	4480
VelP	2600	4200	6300	8040
Dens	2200	2400	2900	3600
Depth to boundary	700	1500	46000	

Table A.9. Seismic model TA-1 (taken directly from Crust1.0) for station E30A. All velocities are in m/s, density in kg/m³ and depth in m. Sedimentary layers highlighted in pale yellow.

E30A	1	2	3	4	5	6
VelS	1070	2740	3600	3700	3900	4500
VelP	2500	4800	6200	6400	6800	8100
Dens	2110	2500	2760	2810	2910	3340
Depth to boundary	500	700	11140	24570	38000	

Table A.10. Seismic model TA-2 (partially derived from Frederiksen & Delaney 2015) for station E30A. All velocities are in m/s, density in kg/m^3 and depth in m. Sedimentary layers highlighted in pale yellow.

E30A	1	2	3	4
VelS	1340	2400	3800	4480
VelP	2600	4200	6300	8040
Dens	2200	2400	2900	3600
Depth to boundary	500	1000	33500	

Table A.11. Seismic model TA-1 (taken directly from Crust1.0) for station F32A. All velocities are in m/s, density in kg/m^3 and depth in m. Sedimentary layers highlighted in pale yellow.

F32A	1	2	3	4	5
VelS	1070	3600	3700	3900	4510
VelP	2500	6200	6400	6800	8120
Dens	2110	2760	2810	2910	3340
Depth to boundary	700	11690	26320	40960	

Table A.12. Seismic model TA-2 (partially derived from Frederiksen & Delaney 2015) for station F32A. All velocities are in m/s, density in kg/m^3 and depth in m. Sedimentary layers highlighted in pale yellow.

F32A	1	2	3
VelS	1340	3800	4480
VelP	2600	6300	8040
Dens	2200	2900	3600
Depth to boundary	500	41500	

The Crust1.0 global model has no sedimentary layer associated with the location of G34A, therefore the model is absent because no layer-strip can be performed.

Table A.13. Seismic model TA-2 (partially derived from Frederiksen & Delaney 2015) for station G34A. All velocities are in m/s, density in kg/m^3 and depth in m. Sedimentary layers highlighted in pale yellow.

G34A	1	2	3
VelS	1340	3800	4480
VelP	2600	6300	8040
Dens	2200	2900	3600
Depth to boundary	100	49000	

Table A.14. Seismic model TA-1 (taken directly from Crust1.0) for station H35A. All velocities are in m/s, density in kg/m³ and depth in m. Sedimentary layers highlighted in pale yellow.

H35A	1	2	3	4	5
VelS	1070	3600	3700	3900	4510
VelP	2500	6200	6400	6800	8130
Dens	2110	2760	2810	2910	3350
Depth to boundary	100	12790	29100	45410	

Table A.15. Seismic model TA-2 (partially derived from Frederiksen & Delaney 2015) for station H35A. All velocities are in m/s, density in kg/m³ and depth in m. Sedimentary layers highlighted in pale yellow.

H35A	1	2	3
VelS	1340	3800	4480
VelP	2600	6300	8040
Dens	2200	2900	3600
Depth to boundary	100	49000	

Table A.16. Seismic model TA-1 (taken directly from Crust1.0) for station I36A. All velocities are in m/s, density in kg/m³ and depth in m. Sedimentary layers highlighted in pale yellow.

I36A	1	2	3	4	5
VelS	1070	3600	3700	3900	4510
VelP	2500	6200	6400	6800	8130
Dens	2110	2760	2810	2910	3350
Depth to boundary	100	12790	29100	45410	

Table A.17. Seismic model TA-2 (partially derived from Frederiksen & Delaney 2015) for station I36A. All velocities are in m/s, density in kg/m³ and depth in m. Sedimentary layers highlighted in pale yellow.

I36A	1	2	3
VelS	1340	3800	4480
VelP	2600	6300	8040
Dens	2200	2900	3600
Depth to boundary	100	39500	

Table A.18. Seismic model TA-1 (taken directly from Crust1.0) for station J38A. All velocities are in m/s, density in kg/m³ and depth in m. Sedimentary layers highlighted in pale yellow.

J38A	1	2	3	4	5
VelS	1070	3530	3710	3930	4480
VelP	2500	6100	6500	6900	8040
Dens	2110	2740	2830	2920	3600
Depth to boundary	200	11600	25250	37390	

Table A.19. Seismic model TA-2 (partially derived from Frederiksen & Delaney 2015) for station J38A. All velocities are in m/s, density in kg/m^3 and depth in m. Sedimentary layers highlighted in pale yellow.

J38A	1	2	3	4
VelS	1340	2400	3800	4480
VelP	2600	4200	6300	8040
Dens	2200	2400	2900	3600
Depth to boundary	500	1000	28000	

B. Stacked RFs

Figure B.1. Stacked non-layer-stripped (top) receiver functions and layer-stripped receiver functions from A25A. Filtered using a layer-strip model from Crust1.0 (centre) and one derived with data from Frederiksen and Delaney (2015) (bottom). Passband filtered between 0.05-0.5 Hz.

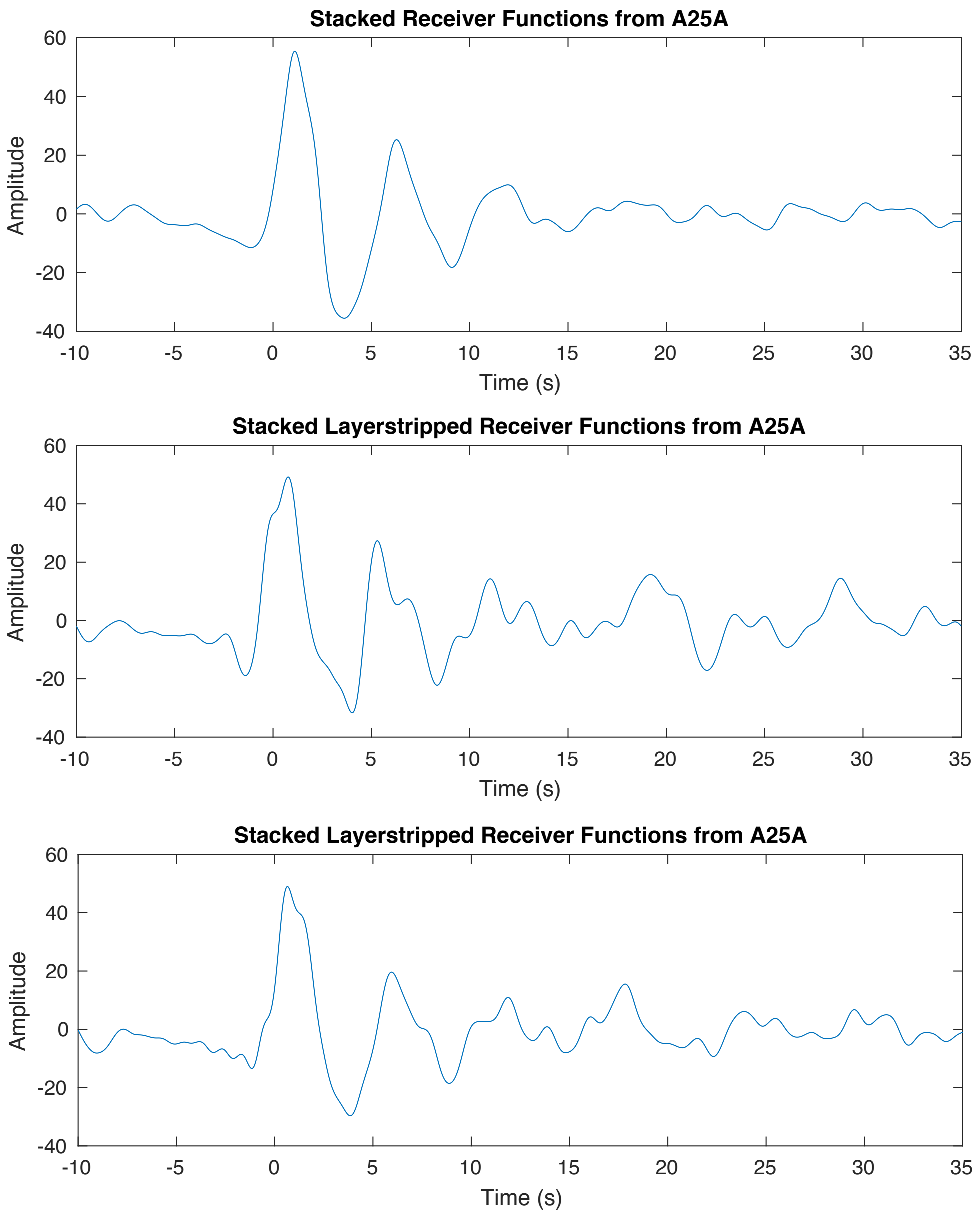

Figure B.2. Stacked non-layer-stripped (top) receiver functions and layer-stripped receiver functions from B26A. Filtered using a layer-strip model from Crust1.0 (centre) and one derived with data from Frederiksen and Delaney (2015) (bottom). Passband filtered between 0.05-0.5 Hz.

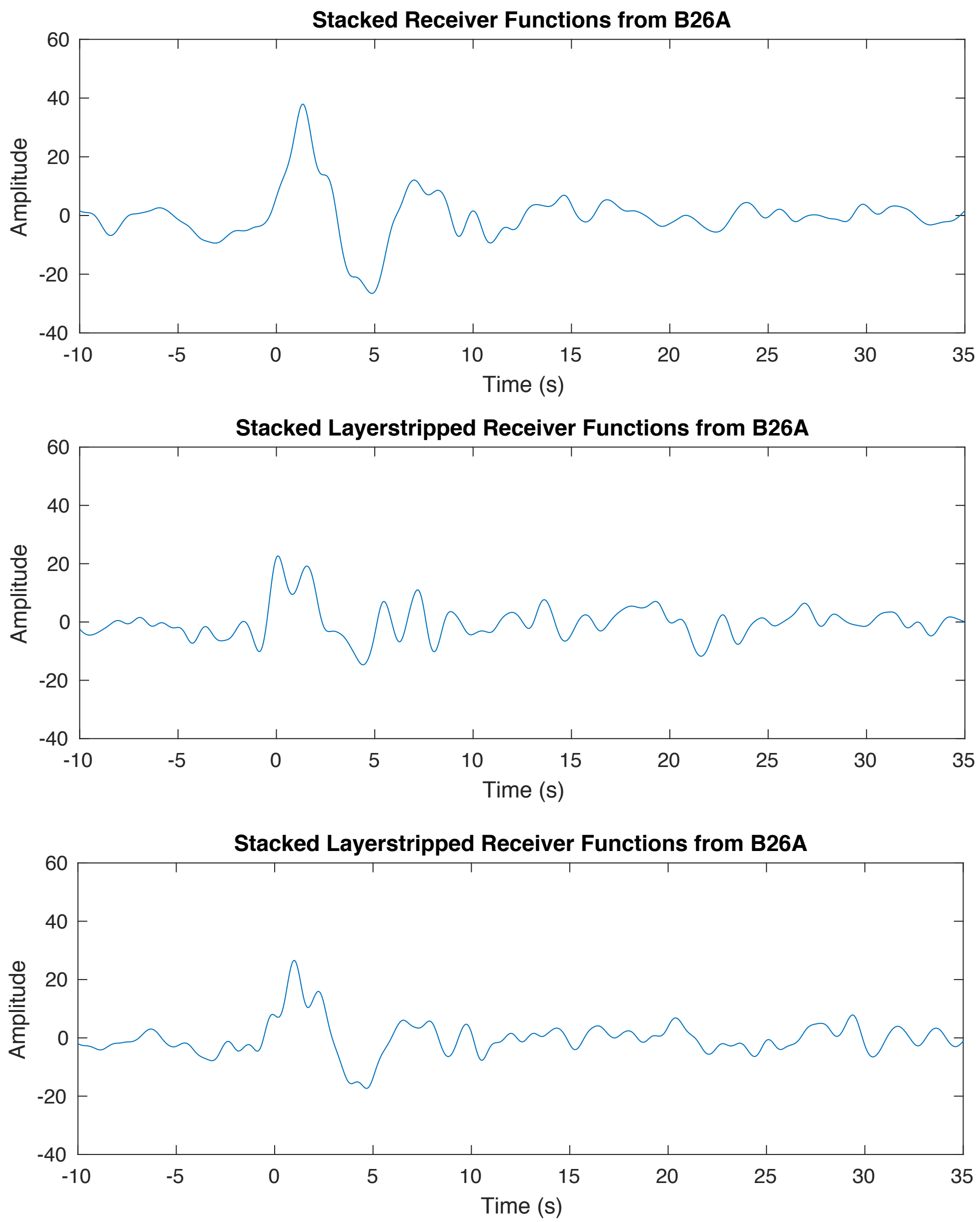

Figure B.3. Stacked non-layer-stripped (top) receiver functions and layer-stripped receiver functions from D28A. Filtered using a layer-strip model from Crust1.0 (centre) and one derived with data from Frederiksen and Delaney (2015) (bottom). Passband filtered between 0.05-0.5 Hz.

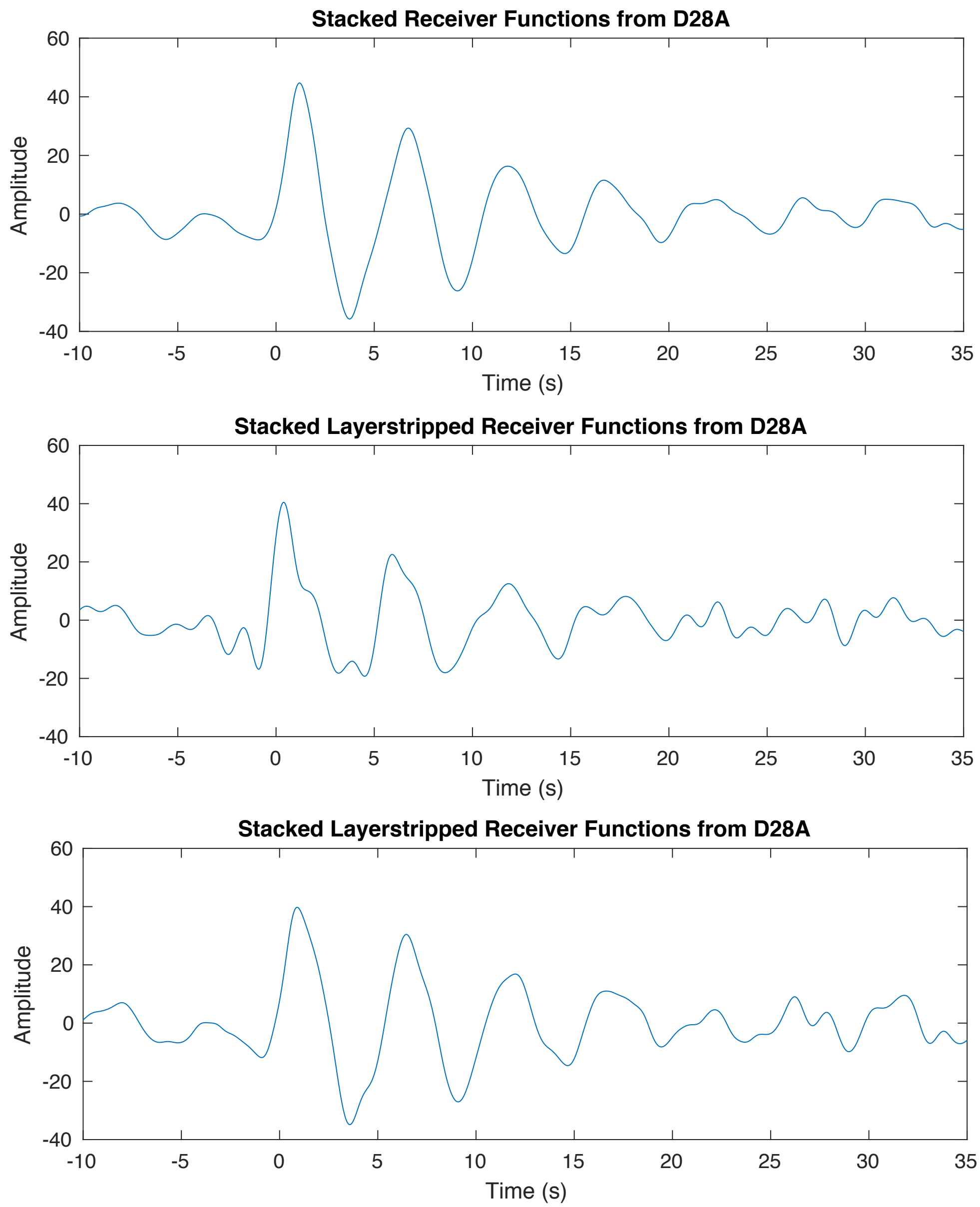

Figure B.4. Stacked non-layer-stripped (top) receiver functions and layer-stripped receiver functions from F32A. Filtered using a layer-strip model from Crust1.0 (centre) and one derived with data from Frederiksen and Delaney (2015) (bottom). Passband filtered between 0.05-0.5 Hz.

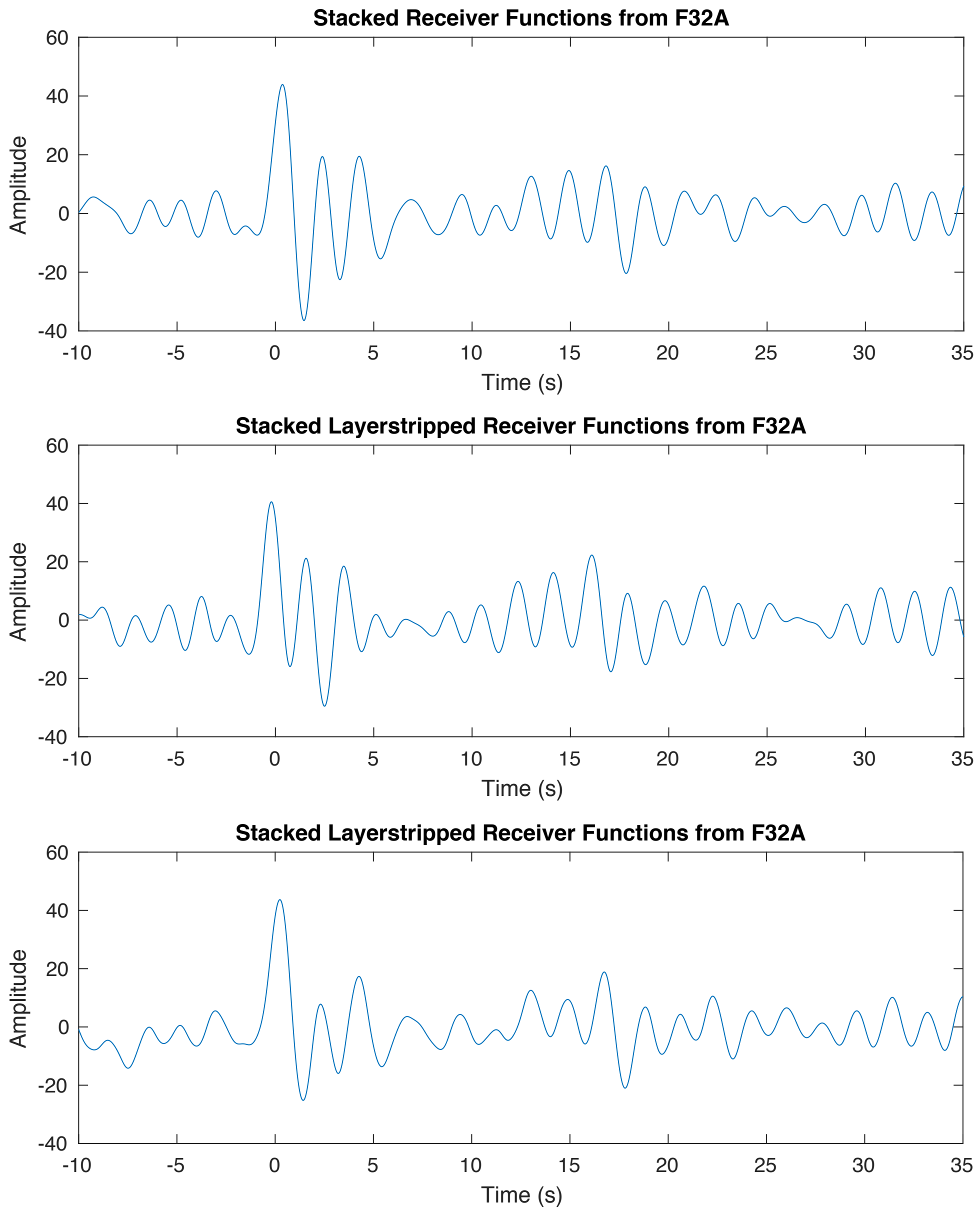

Figure B.5. Stacked non-layer-stripped (top) receiver functions and layer-stripped receiver functions from G34A. Filtered using a layer-strip model partially derived with data from Frederiksen and Delaney (2015) (bottom). Passband filtered between 0.05-0.5 Hz. No model layer-strip was completed with crust1.0 as no sediment exists in the model at this location.

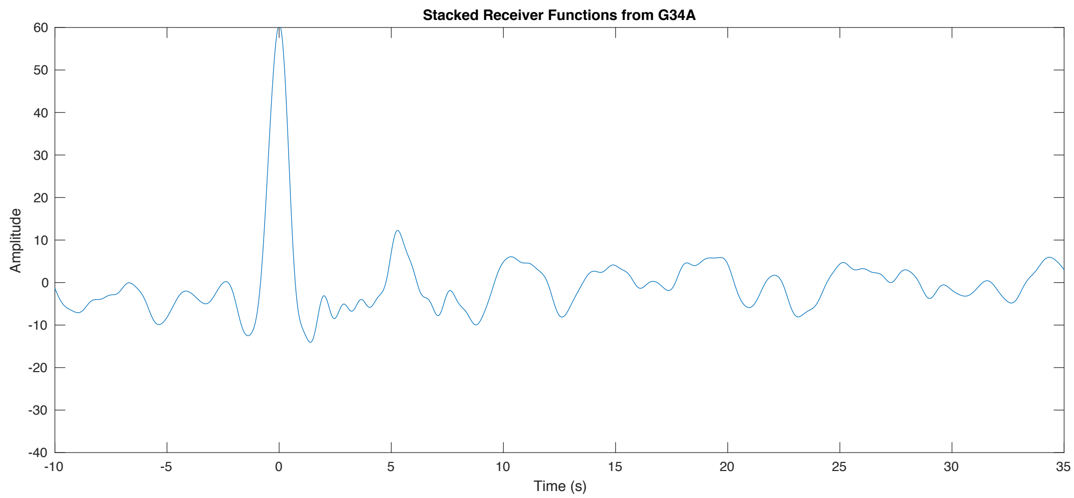

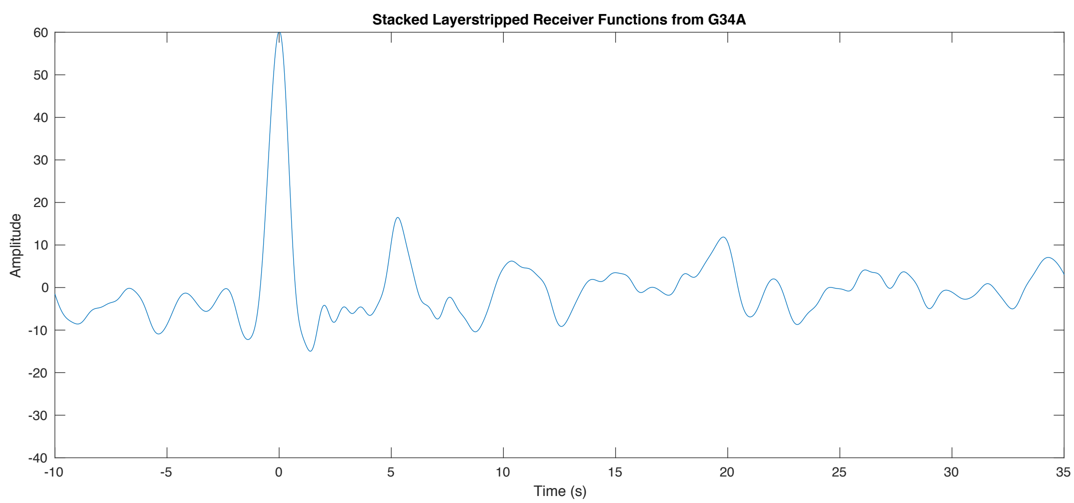

Figure B.6. Stacked non-layer-stripped (top) receiver functions and layer-stripped receiver functions from H35A. Filtered using a layer-strip model from Crust1.0 (centre) and one derived with data from Frederiksen and Delaney (2015) (bottom). Passband filtered between 0.05-0.5 Hz.

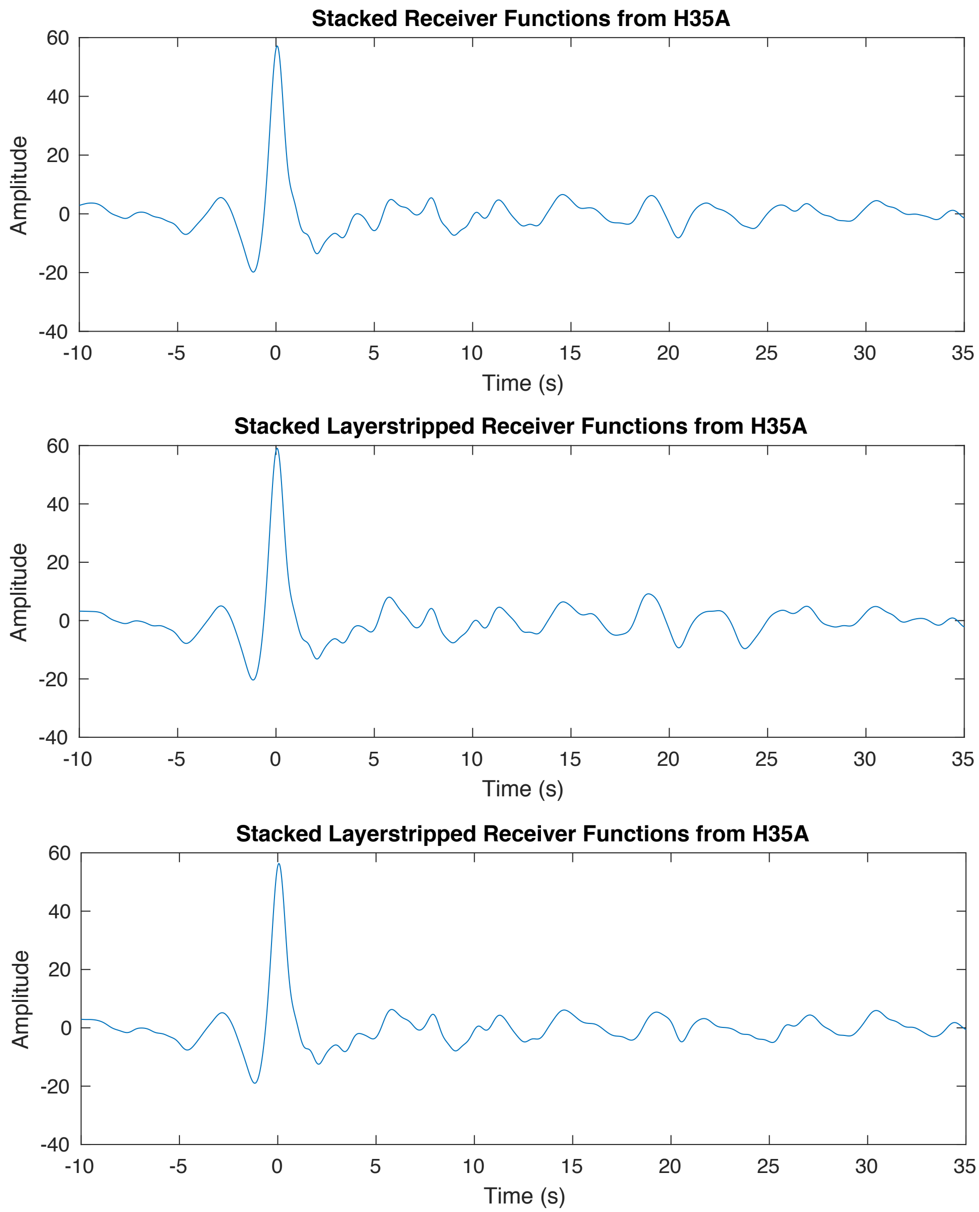

Figure B.7. Stacked non-layer-stripped (top) receiver functions and layer-stripped receiver functions from I36A. Filtered using a layer-strip model from Crust1.0 (centre) and one derived with data from Frederiksen and Delaney (2015) (bottom). Passband filtered between 0.05-0.5 Hz.

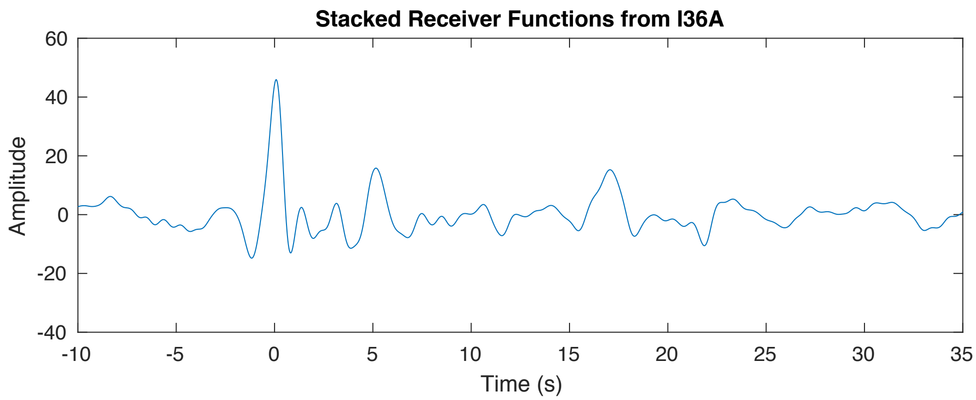

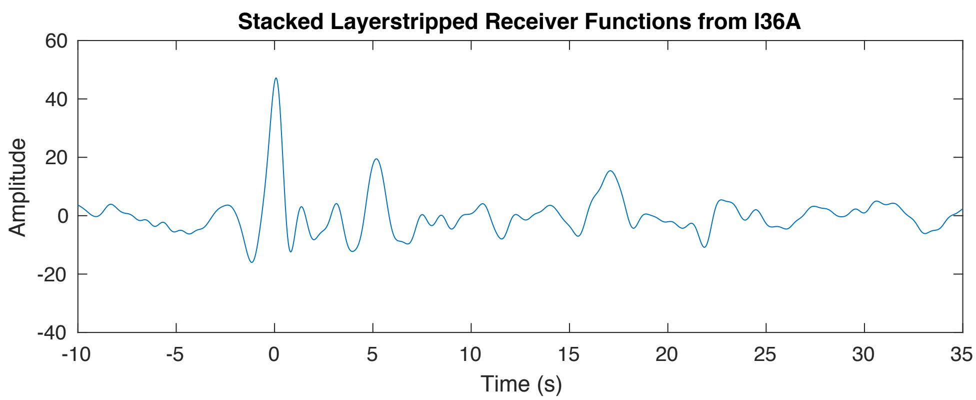

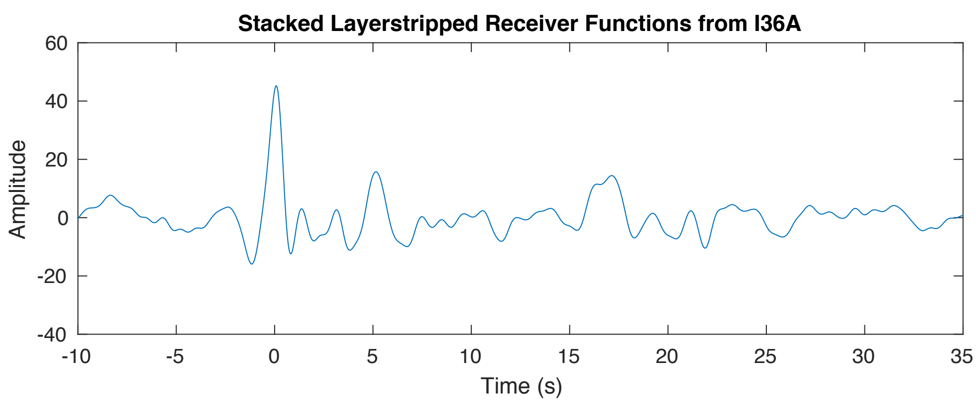

C. Frequency content of receiver functions

Figure C.1. Frequency content of RFs from A25A, non-layer-stripped (top) and layer-stripped data. Filtered using a layer-strip model TA-1 from Crust1.0 (centre) and TA-2 partially derived from Frederiksen and Delaney (2015) (bottom).

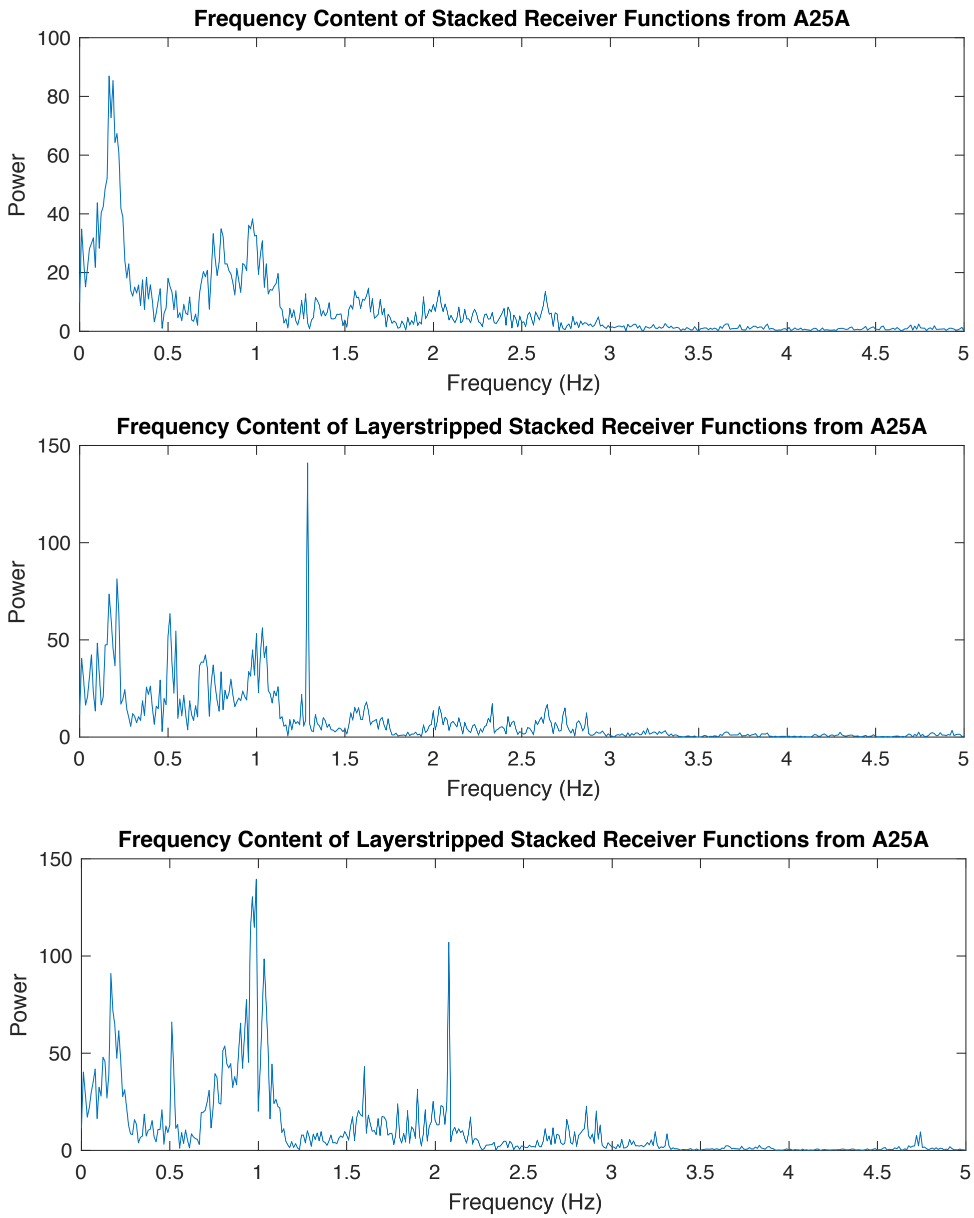

Figure C.2. Frequency content of RFs from B26AA, non-layer-stripped (top) and layer-stripped data. Filtered using a layer-strip model TA-1 from Crust1.0 (centre) and TA-2 partially derived from Frederiksen and Delaney (2015) (bottom).

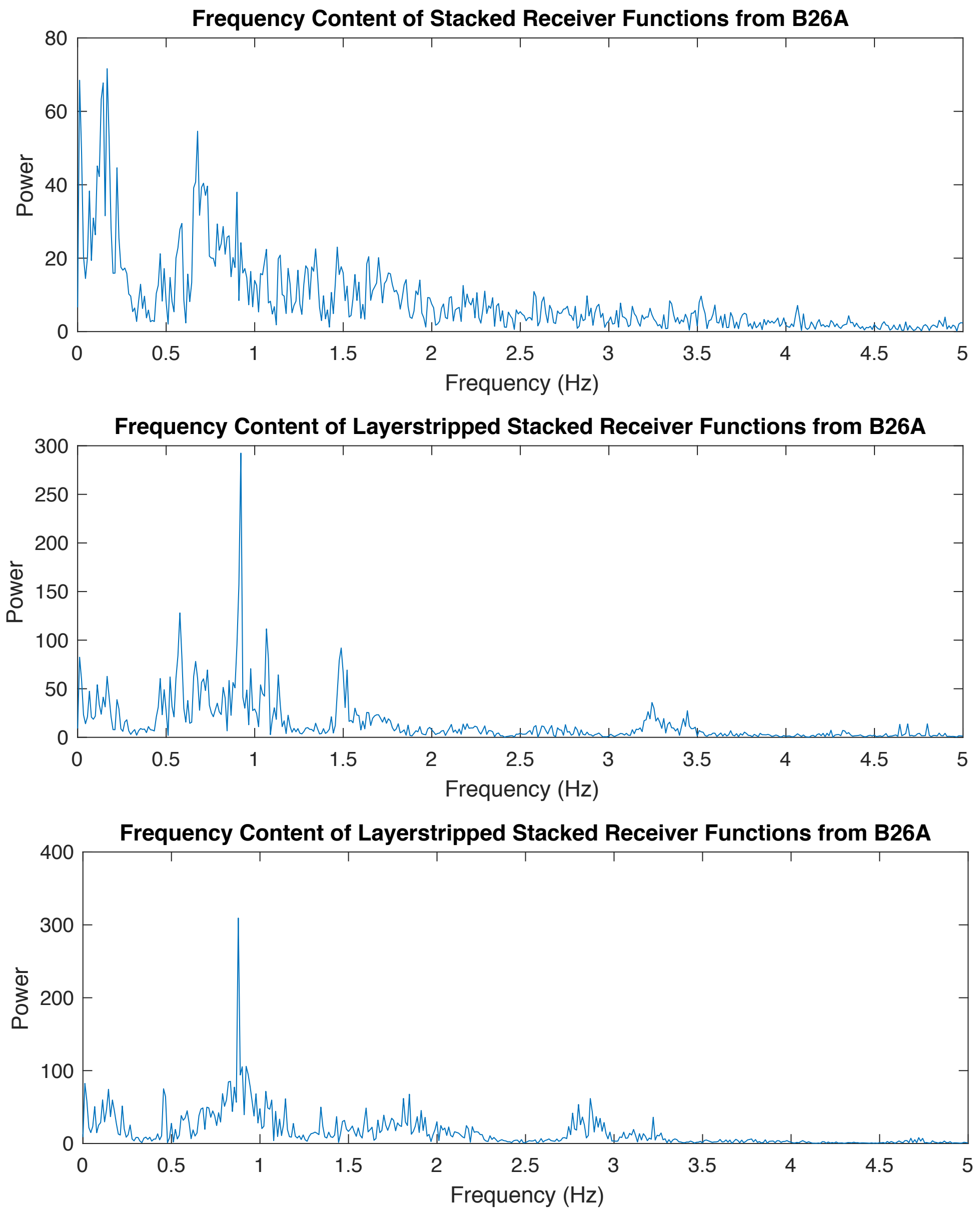

Figure C.3. Frequency content of RFs from D28A, non-layer-stripped (top) and layer-stripped data. Filtered using a layer-strip model TA-1 from Crust1.0 (centre) and TA-2 partially derived from Frederiksen and Delaney (2015) (bottom).

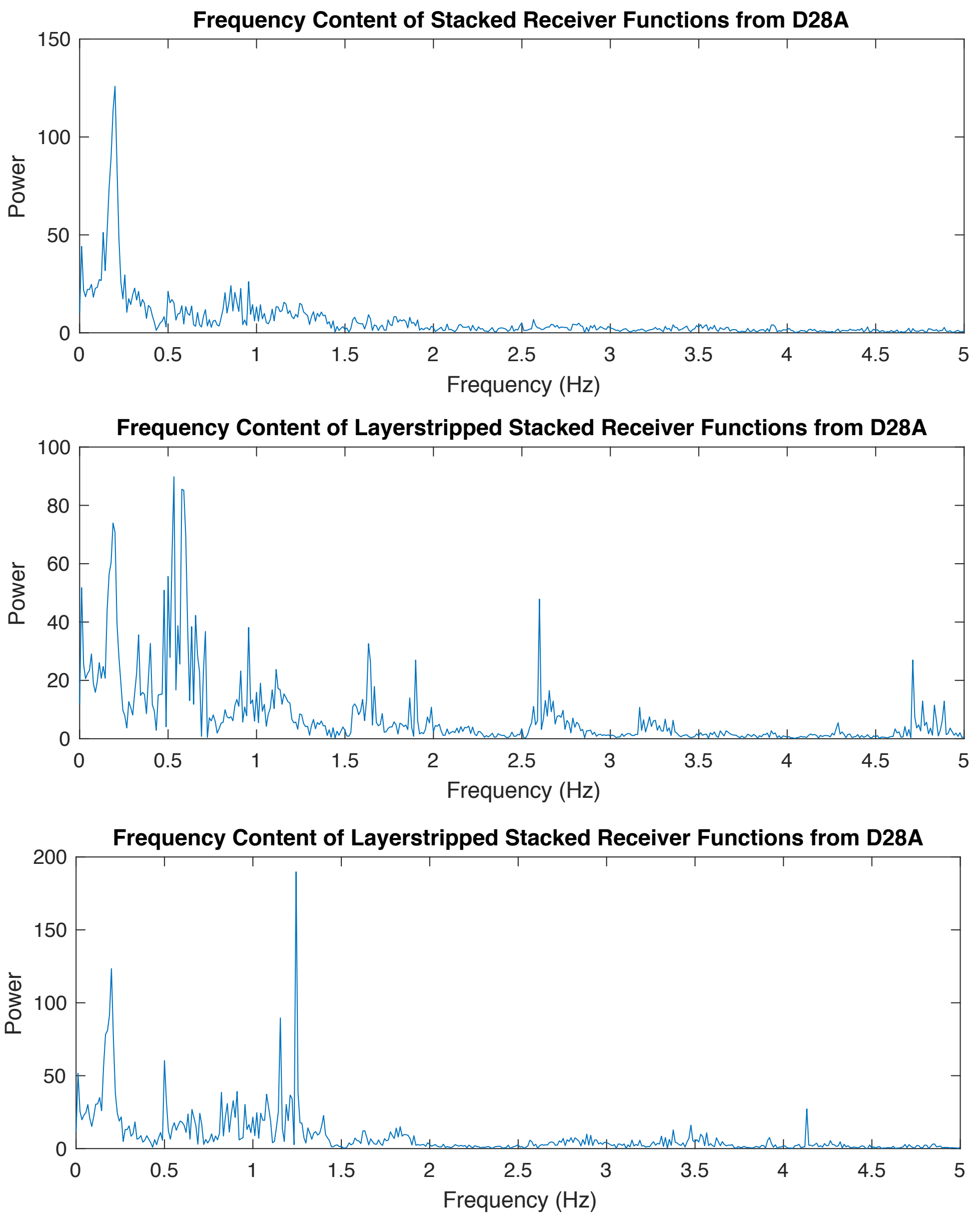

Figure C.4. Frequency content of RFs from F32A, non-layer-stripped (top) and layer-stripped data. Filtered using a layer-strip model TA-1 from Crust1.0 (centre) and TA-2 partially derived from Frederiksen and Delaney (2015) (bottom).

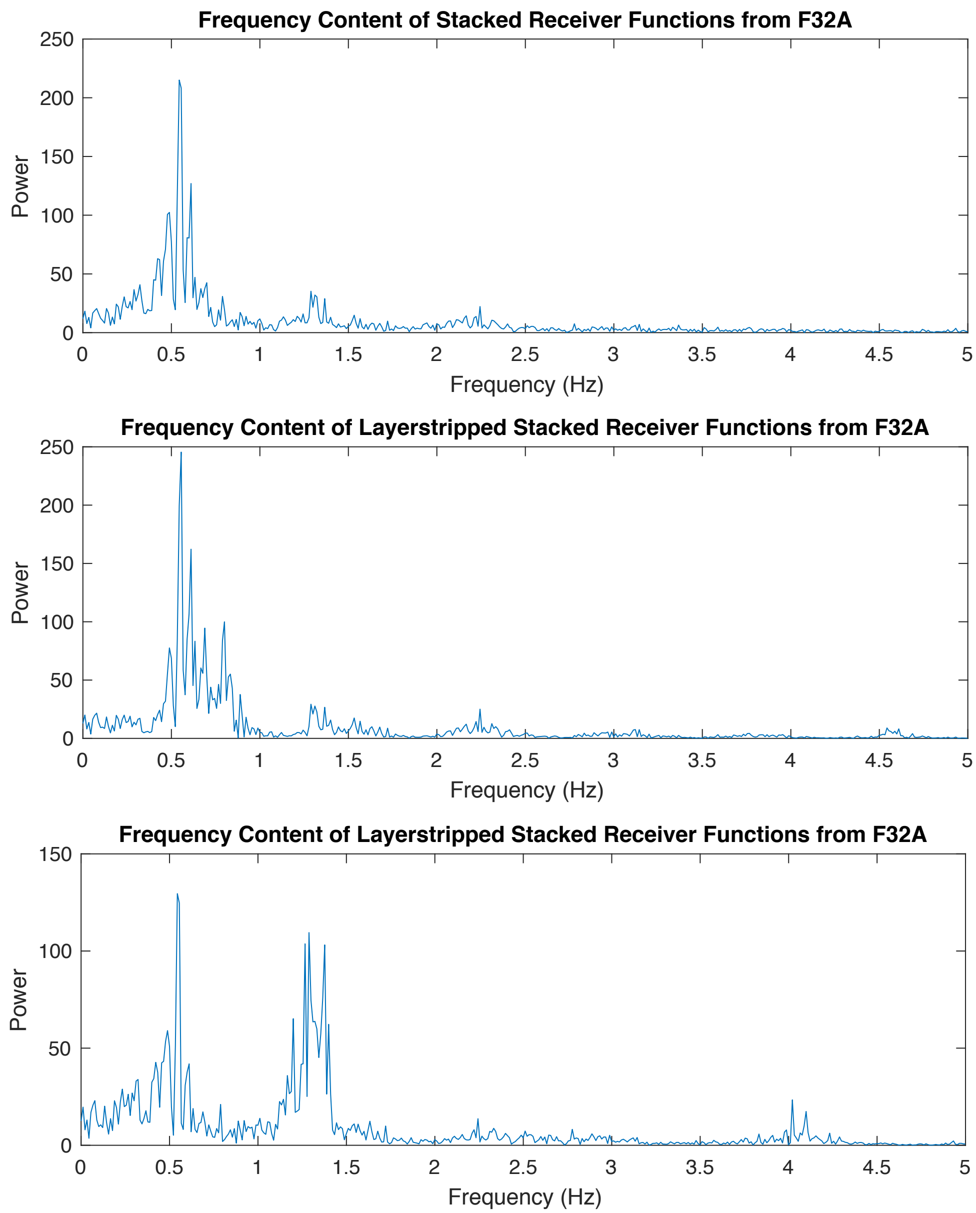

Figure C.5. Frequency content from layer-stripped and non-layer-stripped G34A. Filtered using a layer-strip model partially derived with data from Frederiksen and Delaney (2015) (bottom). No model layer-strip was completed with crust1.0 as no sediment exists in the model at this location.

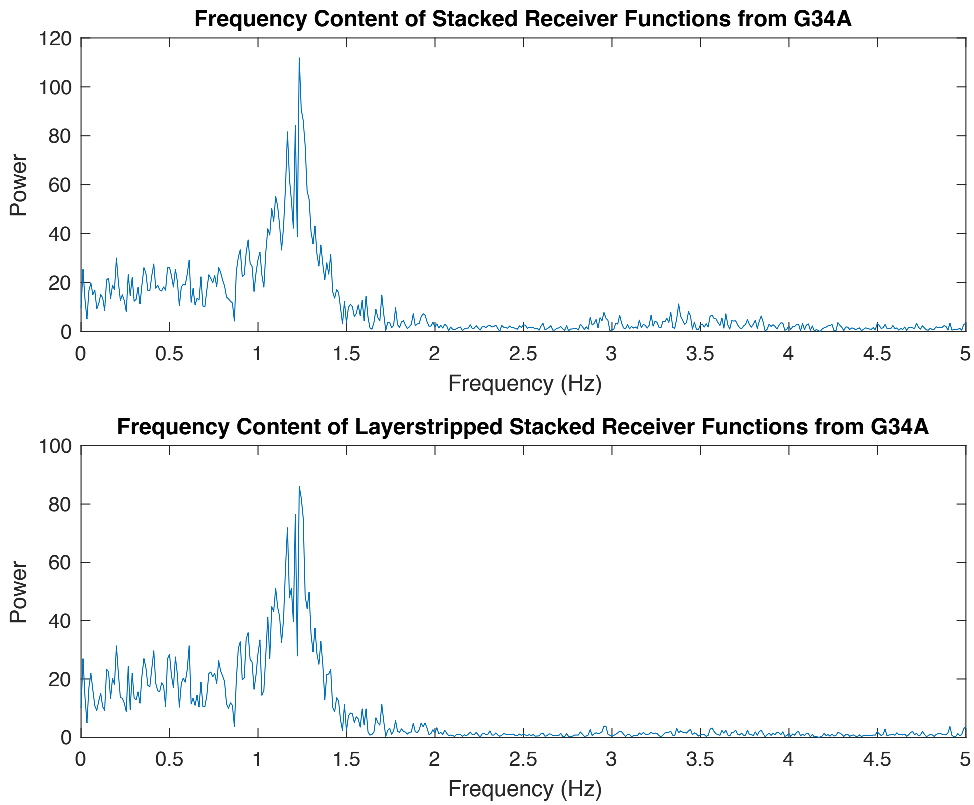

Figure C.6. Frequency content of RFs from H35A, non-layer-stripped (top) and layer-stripped data. Filtered using a layer-strip model TA-1 from Crust1.0 (centre) and TA-2 partially derived from Frederiksen and Delaney (2015) (bottom).

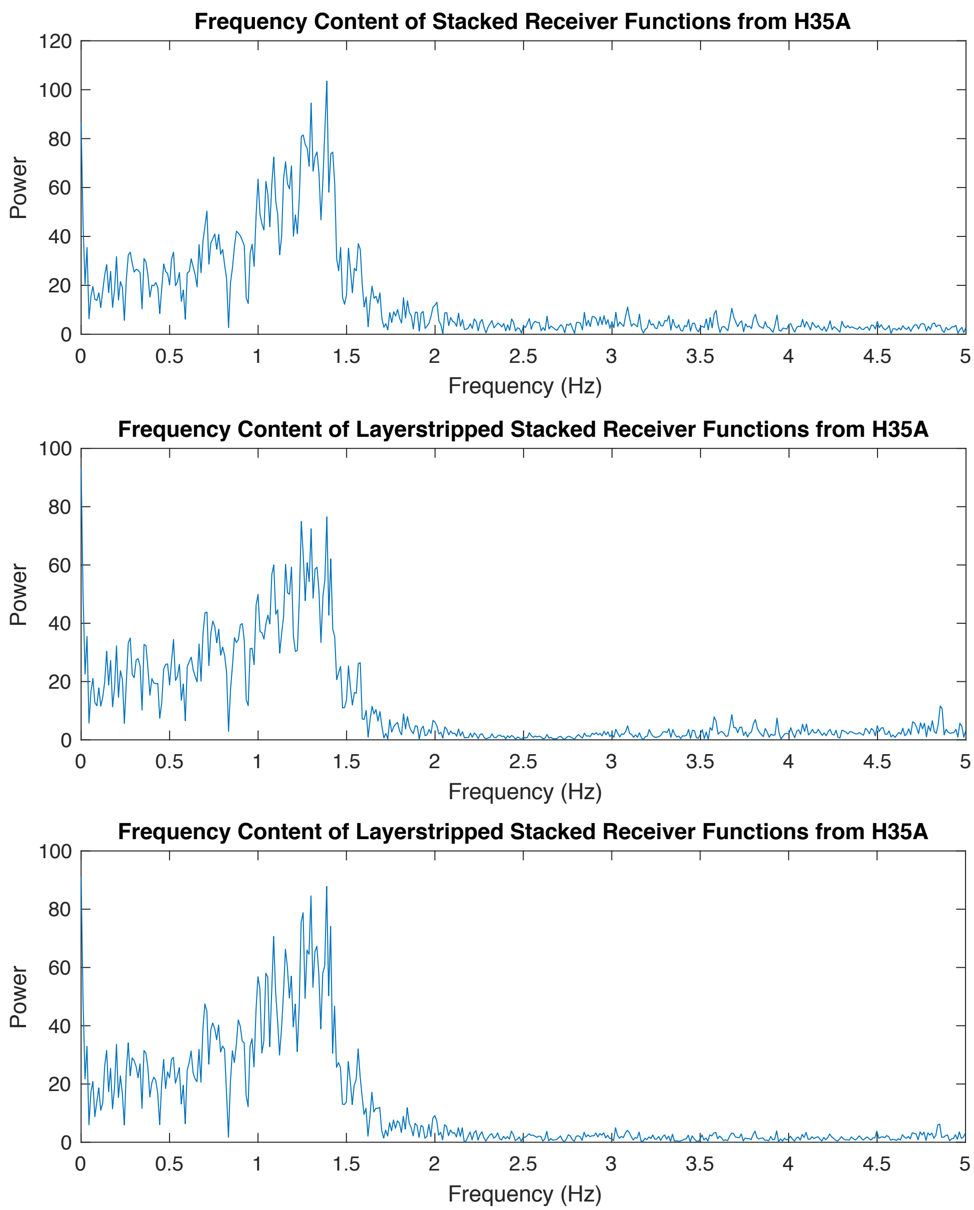

Figure C.7. Frequency content of RFs from I36A, non-layer-stripped (top) and layer-stripped data. Filtered using a layer-strip model TA-1 from Crust1.0 (centre) and TA-2 partially derived from Frederiksen and Delaney (2015) (bottom).

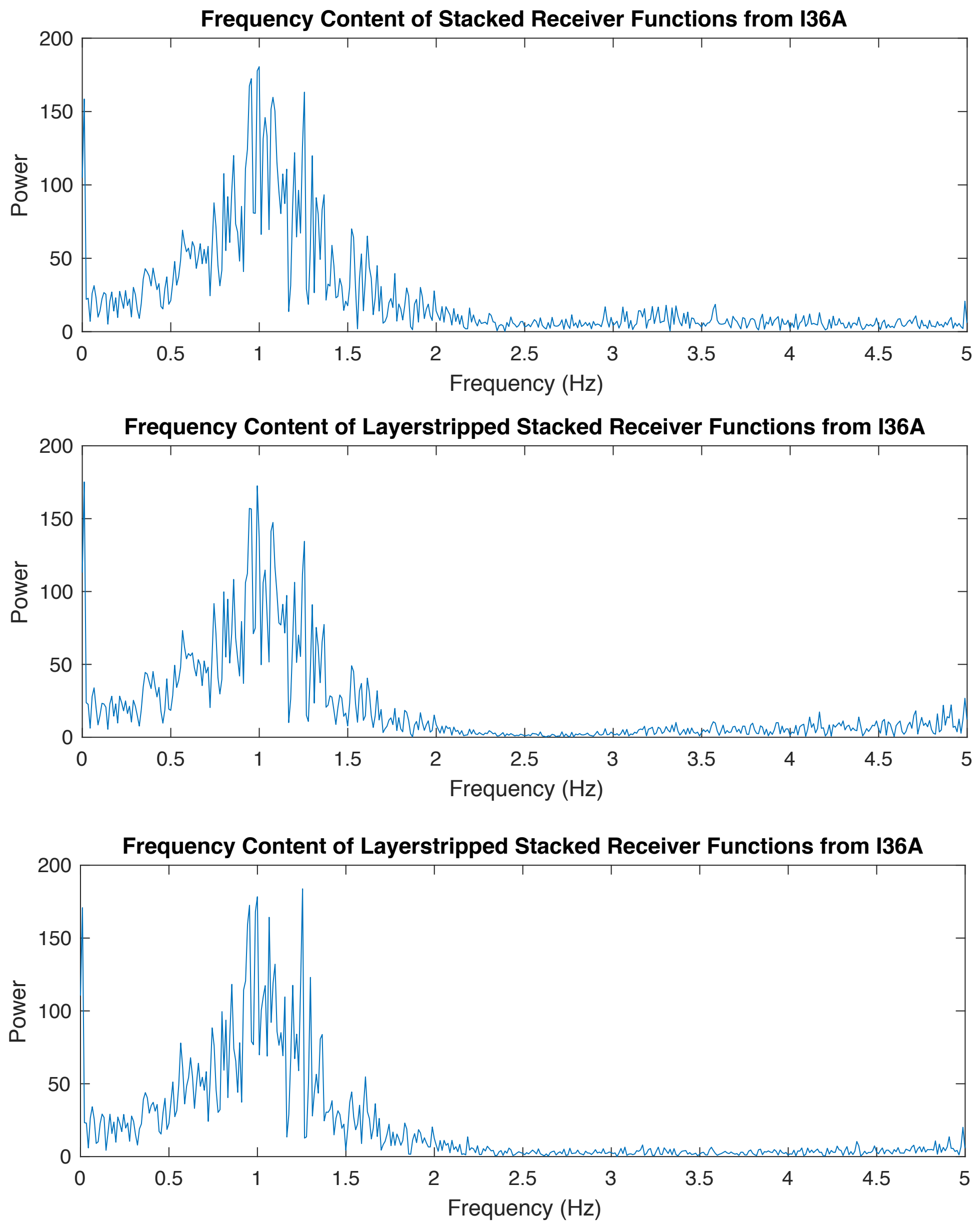

D. H-K search results

Figure D.1. Result from 4th root H-K stack performed on non-layer-stripped data from A25A. Areas of lighter color show a higher stacked amplitude. The asterisk indicates highest amplitude. Resulting crustal thickness is 43.2 km.

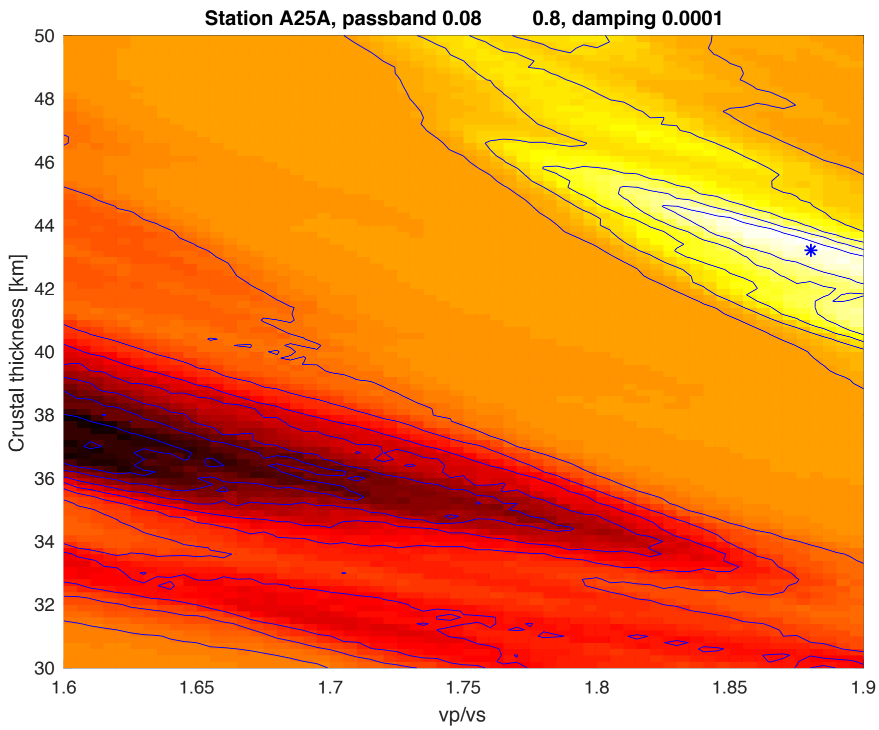

Figure D.2. Result from 4th root H-K stack performed on layer-stripped data from A25A using TA-1 from Crust1.0. Areas of lighter color show a higher stacked amplitude. The asterisk indicates highest amplitude. Resulting crustal thickness after correction is 53.3 km (corrected second local solution at 42.8 km).

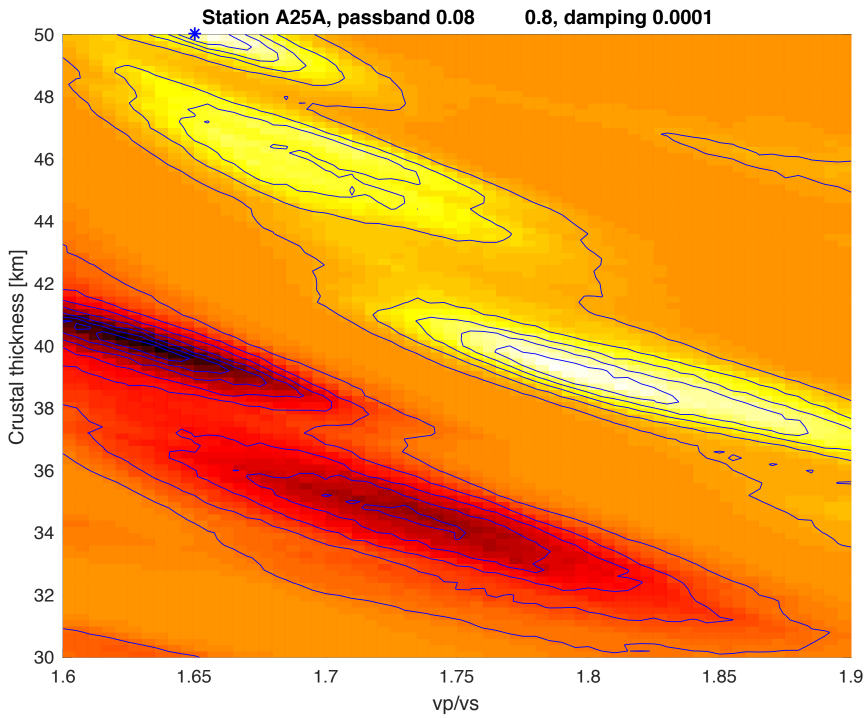

Figure D.3. Result from 4th root H-K stack performed on layer-stripped data from A25A using model TA-2. Areas of lighter color show a higher stacked amplitude. The asterisk indicates highest amplitude. Resulting crustal thickness after correction is 42.9 km.

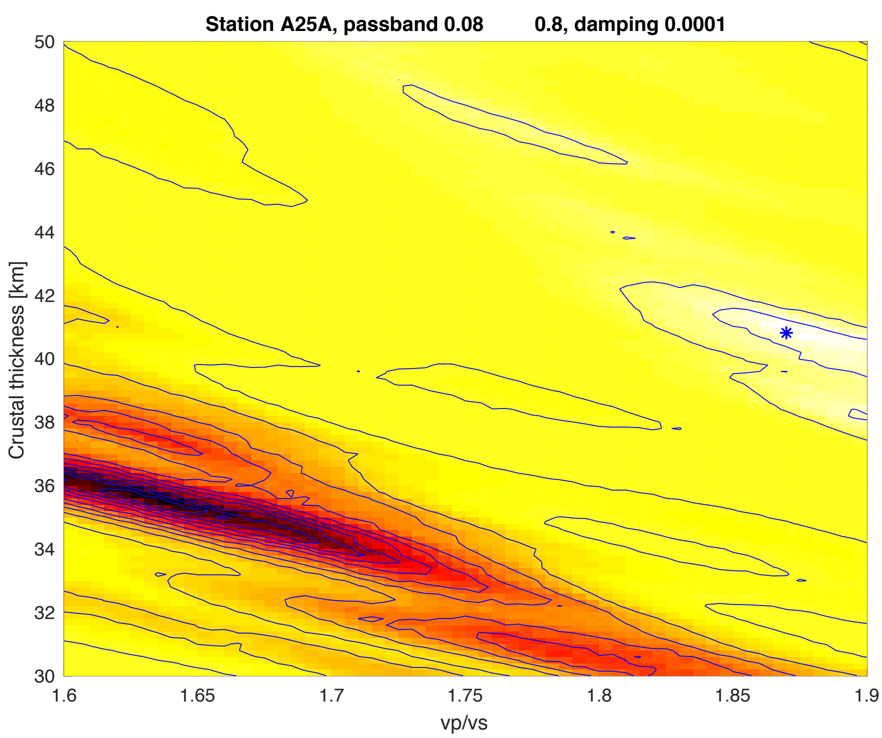

Figure D.4. Result from 4th root H-K stack performed on non-layer-stripped data from B26A. Areas of lighter color show a higher stacked amplitude. The asterisk indicates highest amplitude. Resulting crustal thickness is 47.6km.

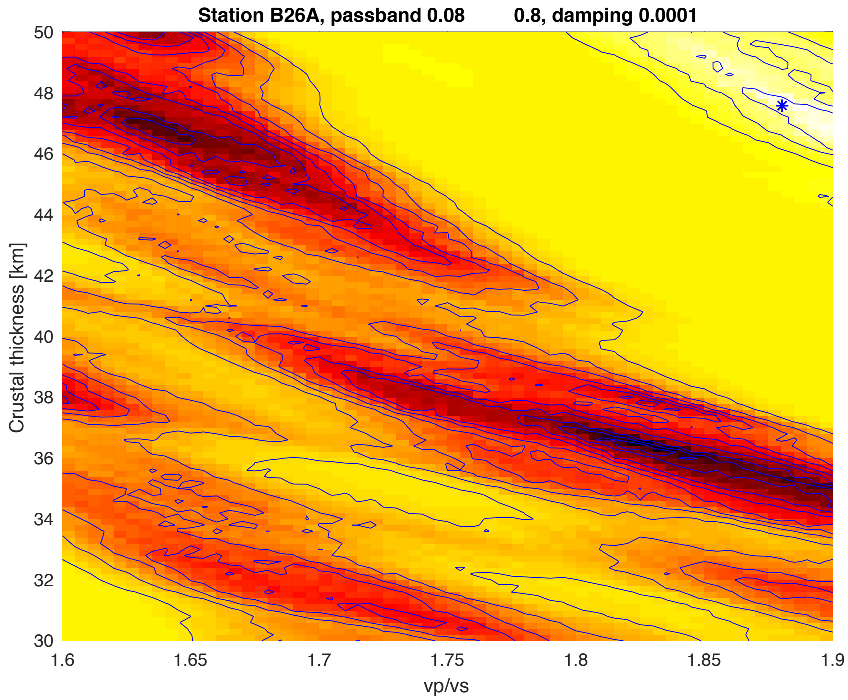

Figure D.5. Result from 4th root H-K stack performed on layer-stripped data from B26A using TA-1 from Crust1.0. Areas of lighter color show a higher stacked amplitude. The asterisk indicates highest amplitude. Resulting crustal thickness after correction is 45.2 km.

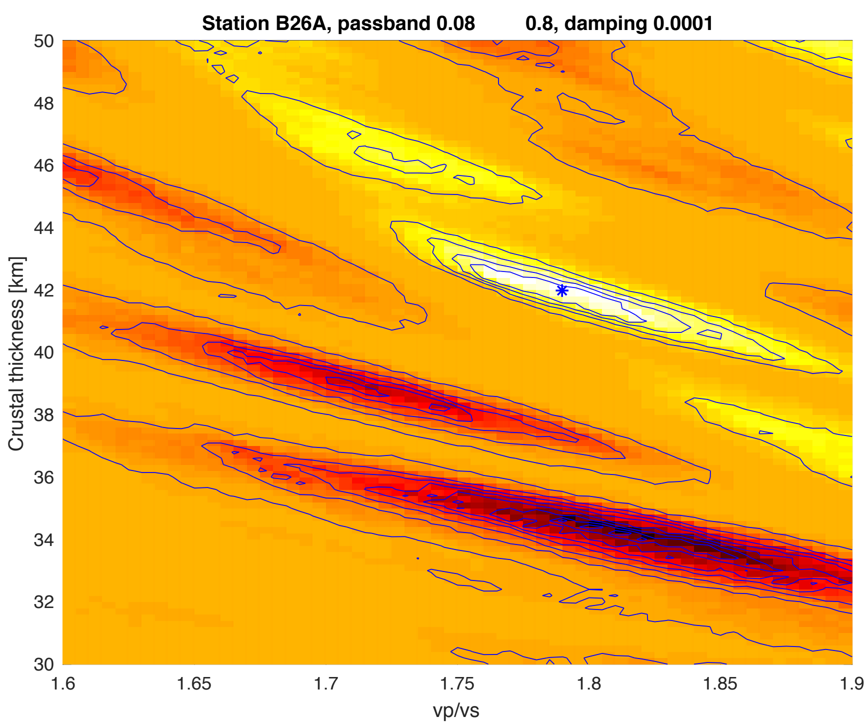

Figure D.6. Result from 4th root H-K stack performed on layer-stripped data from B26A using model TA-2. Areas of lighter color show a higher stacked amplitude. The asterisk indicates highest amplitude. Resulting crustal thickness after correction is 47.9 km.

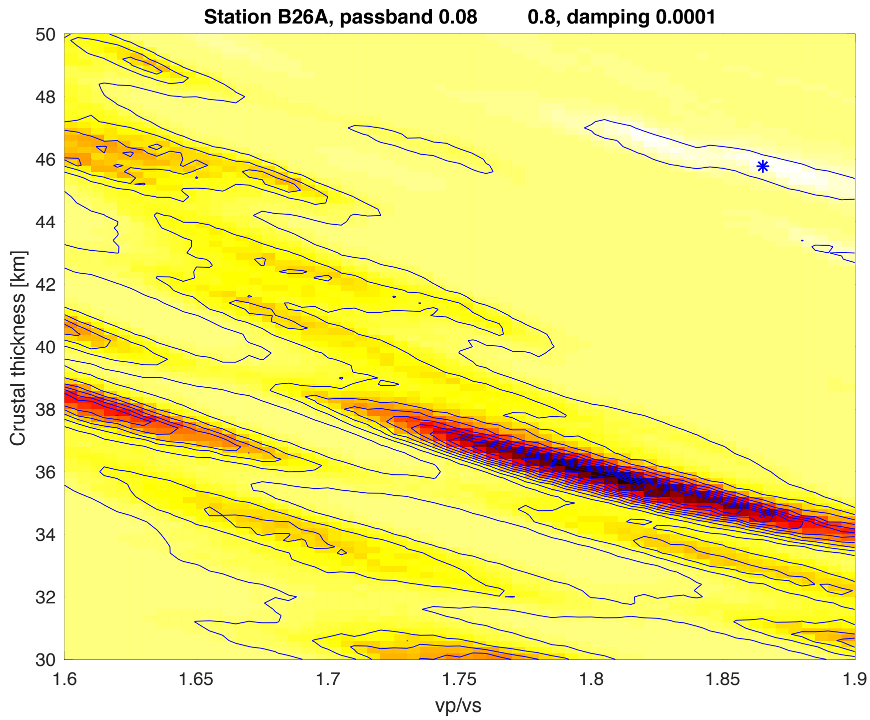

Figure D.7. Result from 4th root H-K stack performed on non-layer-stripped data from D28A. Areas of lighter color show a higher stacked amplitude. The asterisk indicates highest amplitude. Resulting crustal thickness is 50 km.

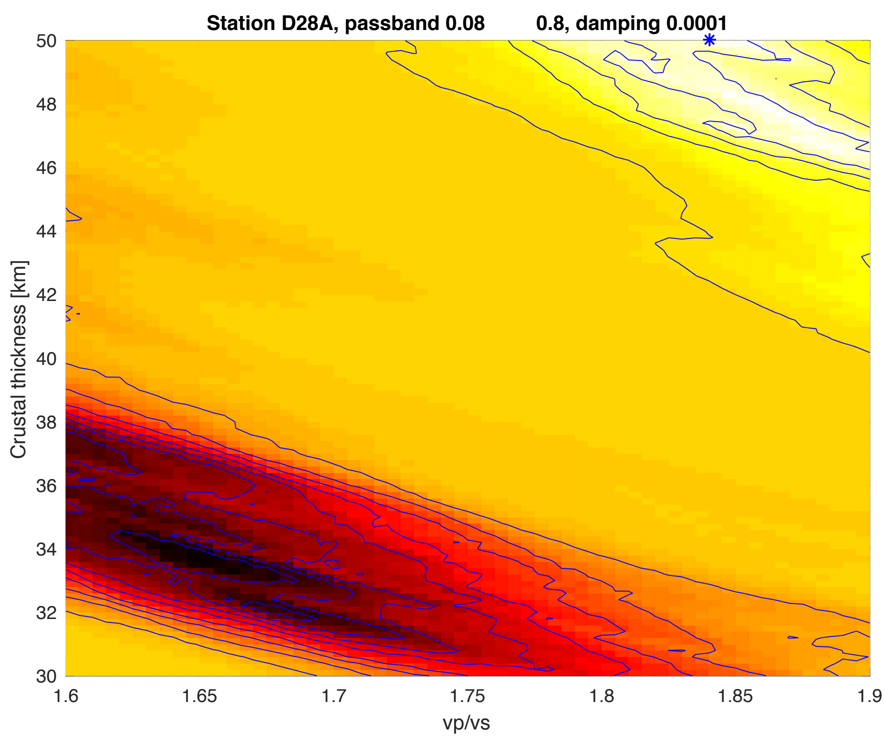

Figure D.8. Result from 4th root H-K stack performed on layer-stripped data from D28A using TA-1 from Crust1.0. Areas of lighter color show a higher stacked amplitude. The asterisk indicates highest amplitude. Resulting crustal thickness after correction is 43.6 km.

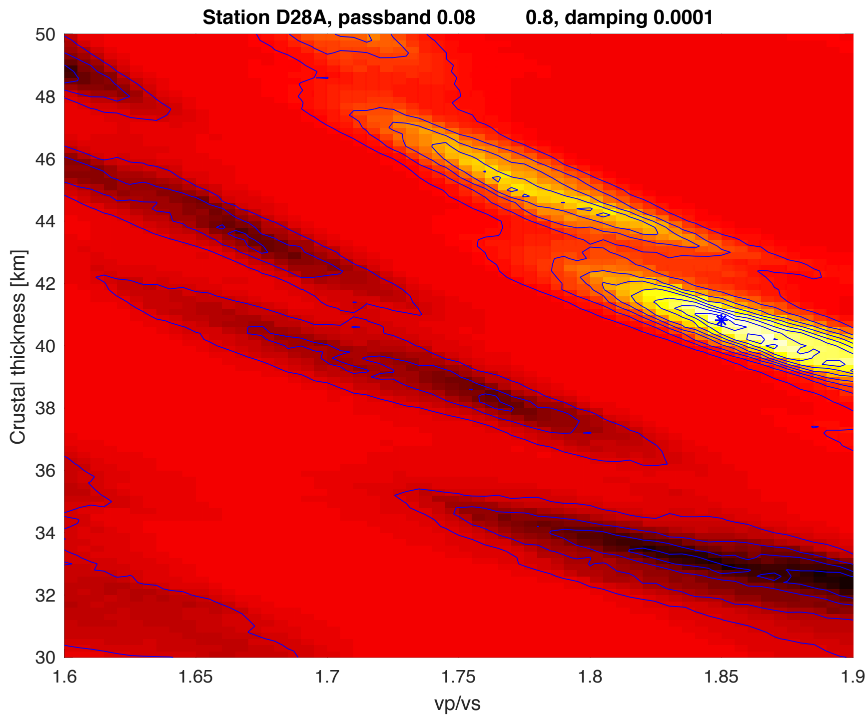

Figure D.9. Result from 4th root H-K stack performed on layer-stripped data from D28A using model TA-2. Areas of lighter color show a higher stacked amplitude. The asterisk indicates highest amplitude. Resulting crustal thickness after correction is 49.5 km.

Figure D.10. Result from 4th root H-K stack performed on non-layer-stripped data from F32A. Areas of lighter color show a higher stacked amplitude. The asterisk indicates highest amplitude. Resulting crustal thickness is 30.2 km.

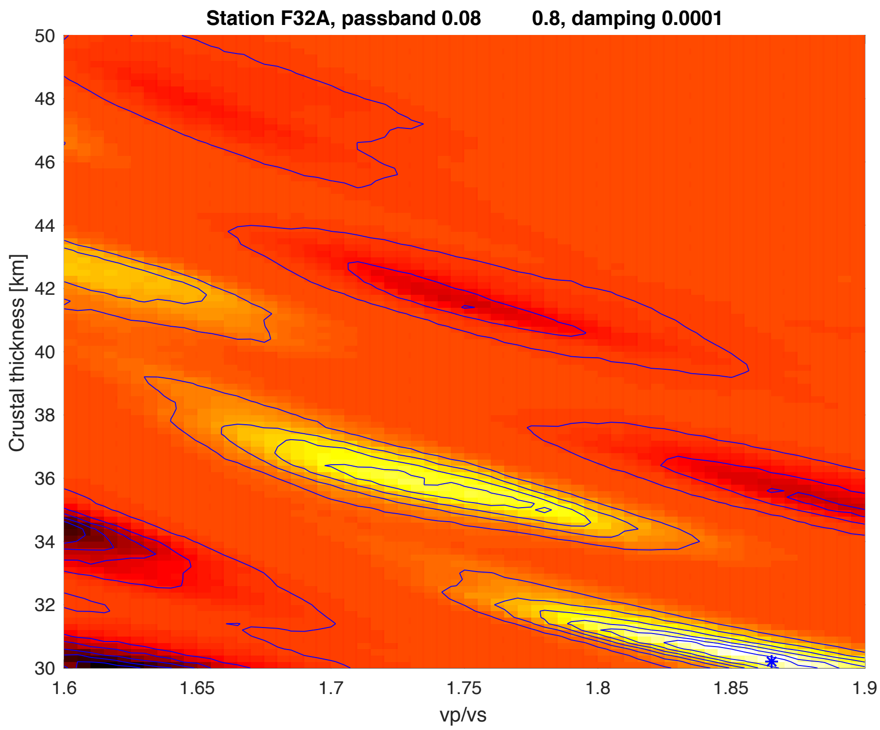

Figure D.11. Result from 4th root H-K stack performed on layer-stripped data from F32A using TA-1 from Crust1.0. Areas of lighter color show a higher stacked amplitude. The asterisk indicates highest amplitude. Resulting crustal thickness after correction is 36.2 km.

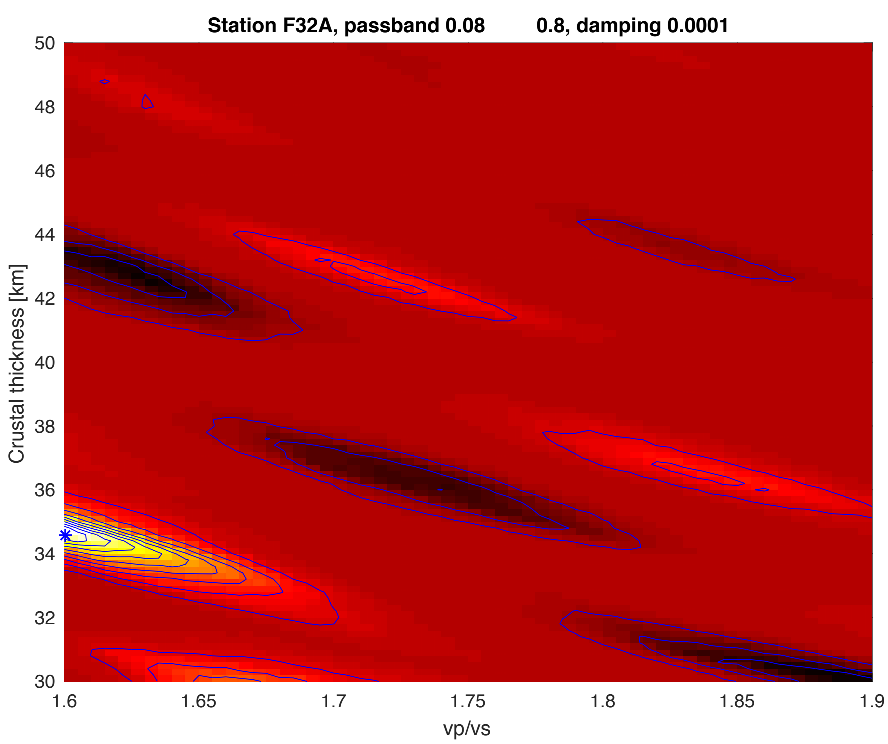

Figure D.12. Result from 4th root H-K stack performed on layer-stripped data from F32A using model TA-2. Areas of lighter color show a higher stacked amplitude. The asterisk indicates highest amplitude. Resulting crustal thickness after correction is 30.9 km.

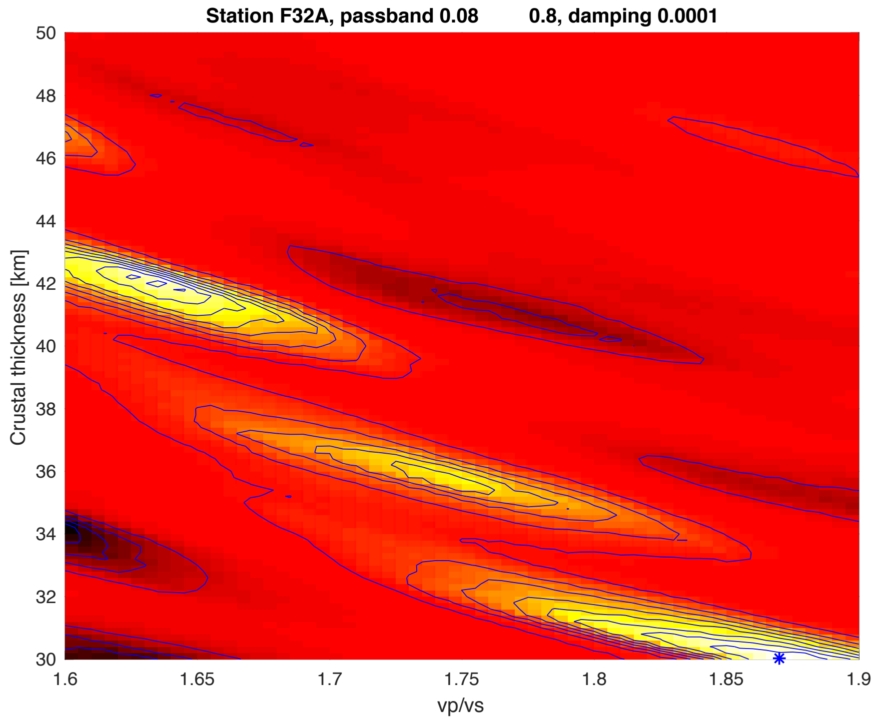

Figure D.13. Result from 4th root H-K stack performed on non-layer-stripped data from G34A. Areas of lighter color show a higher stacked amplitude. The asterisk indicates highest amplitude. Resulting crustal thickness is 42.3 km.

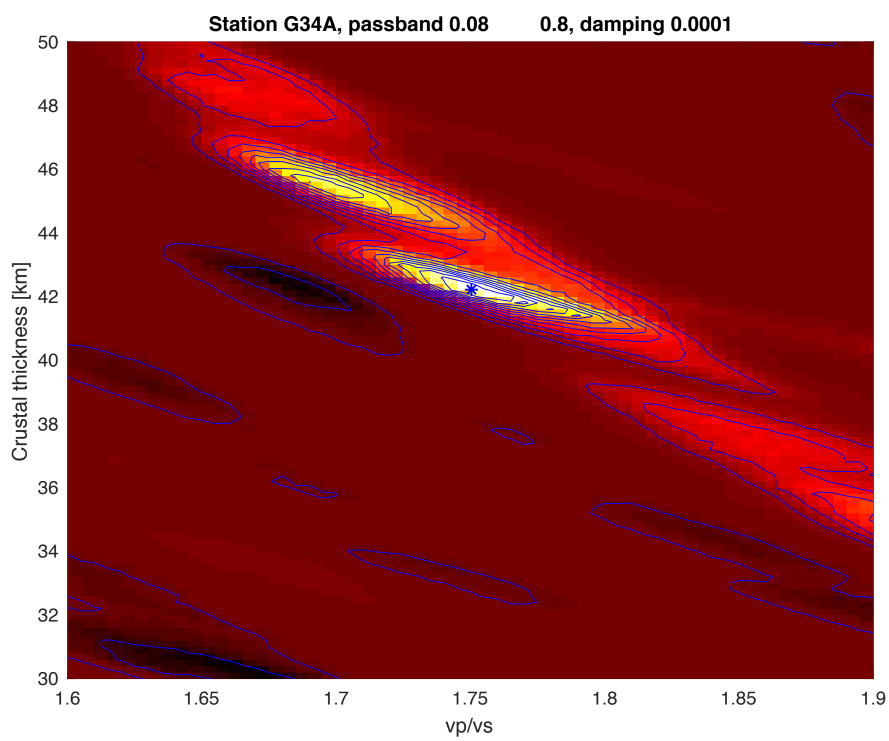

Figure D.14. Result from 4th root H-K stack performed on layer-stripped data from G34A using model TA-2. Areas of lighter color show a higher stacked amplitude. The asterisk indicates highest amplitude. Resulting crustal thickness after correction is 42.5 km.

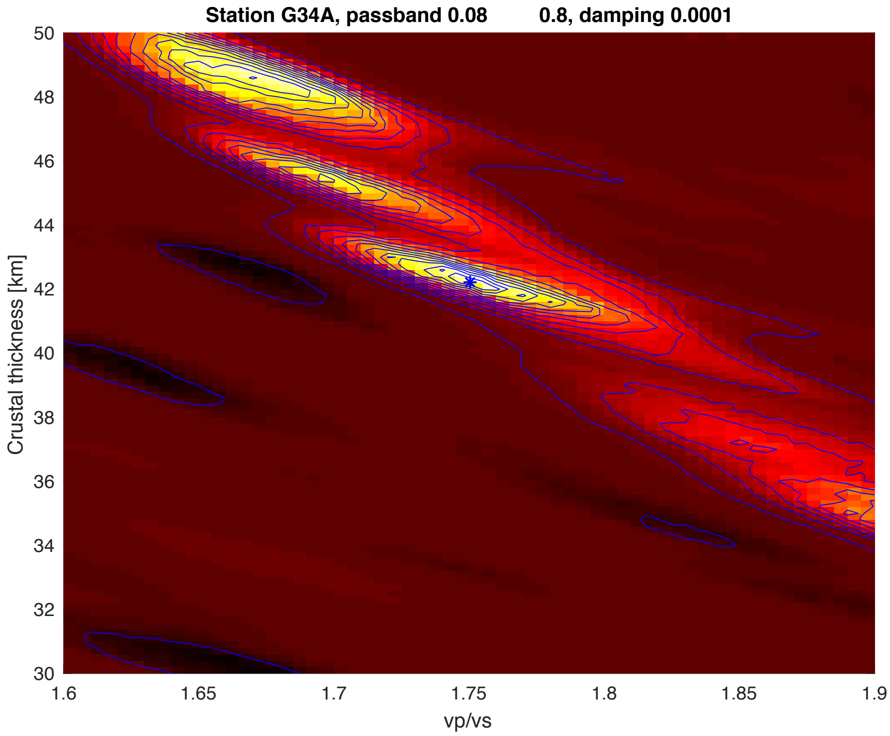

Figure D.15. Result from 4th root H-K stack performed on non-layer-stripped data from H35A. Areas of lighter color show a higher stacked amplitude. The asterisk indicates highest amplitude. Resulting crustal thickness is 42.8 km.

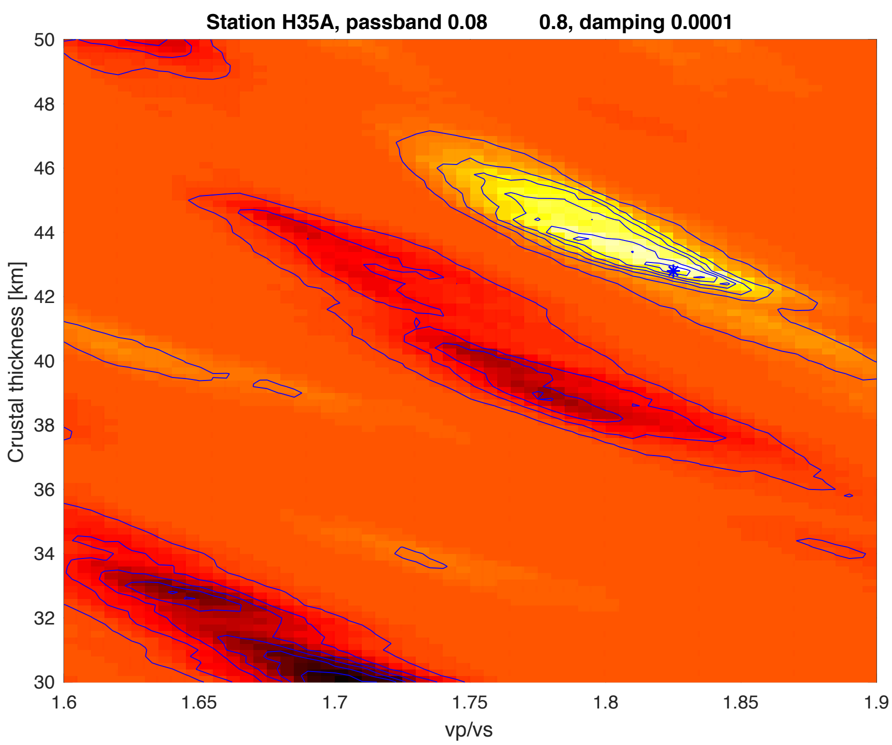

Figure D.16. Result from 4th root H-K stack performed on layer-stripped data from H35A using TA-1 from Crust1.0. Areas of lighter color show a higher stacked amplitude. The asterisk indicates highest amplitude. Resulting crustal thickness after correction is 43.6 km.

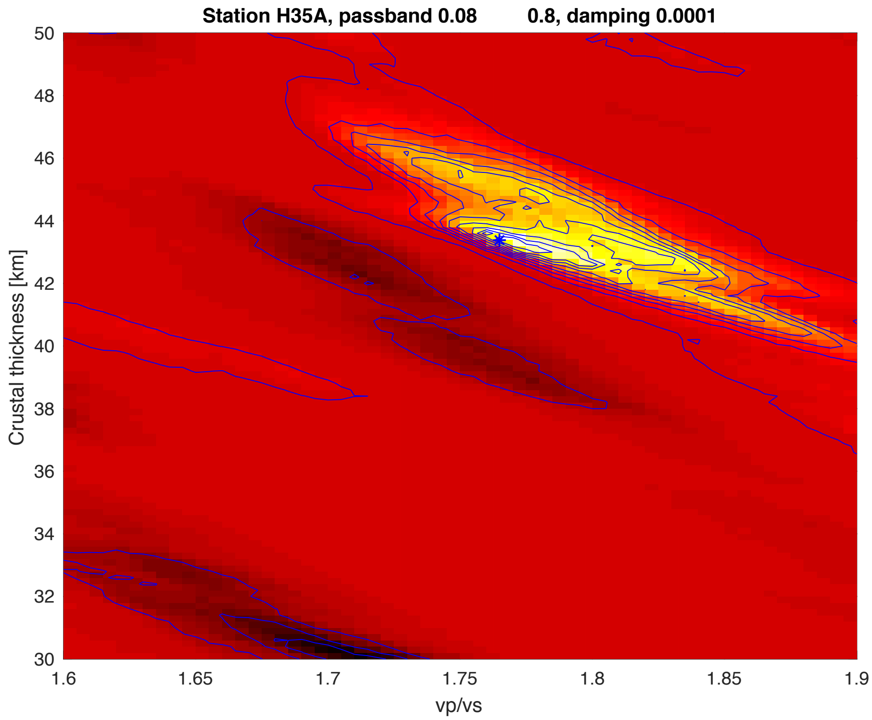

Figure D.17. Result from 4th root H-K stack performed on layer-stripped data from H35A using model TA-2. Areas of lighter color show a higher stacked amplitude. The asterisk indicates highest amplitude. Resulting crustal thickness after correction is 47.0 km.

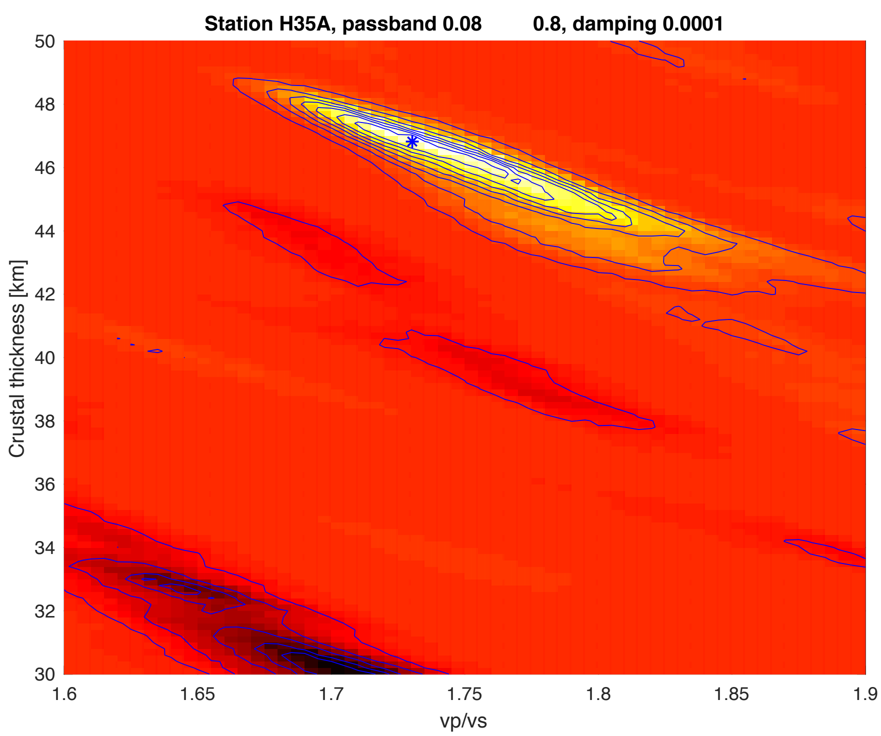

Figure D.18. Result from 4th root H-K stack performed on non-layer-stripped data from I36A. Areas of lighter color show a higher stacked amplitude. The asterisk indicates highest amplitude. Resulting crustal thickness is 39.6 km.

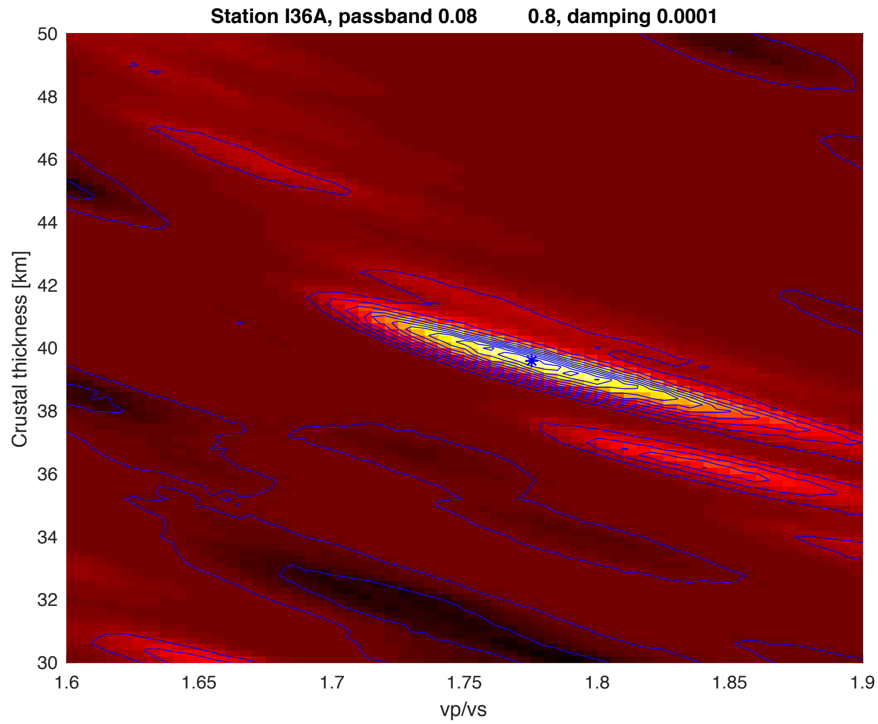

Figure D.19. Result from 4th root H-K stack performed on layer-stripped data from I36A using TA-1 from Crust1.0. Areas of lighter color show a higher stacked amplitude. The asterisk indicates highest amplitude. Resulting crustal thickness after correction is 39.2 km.

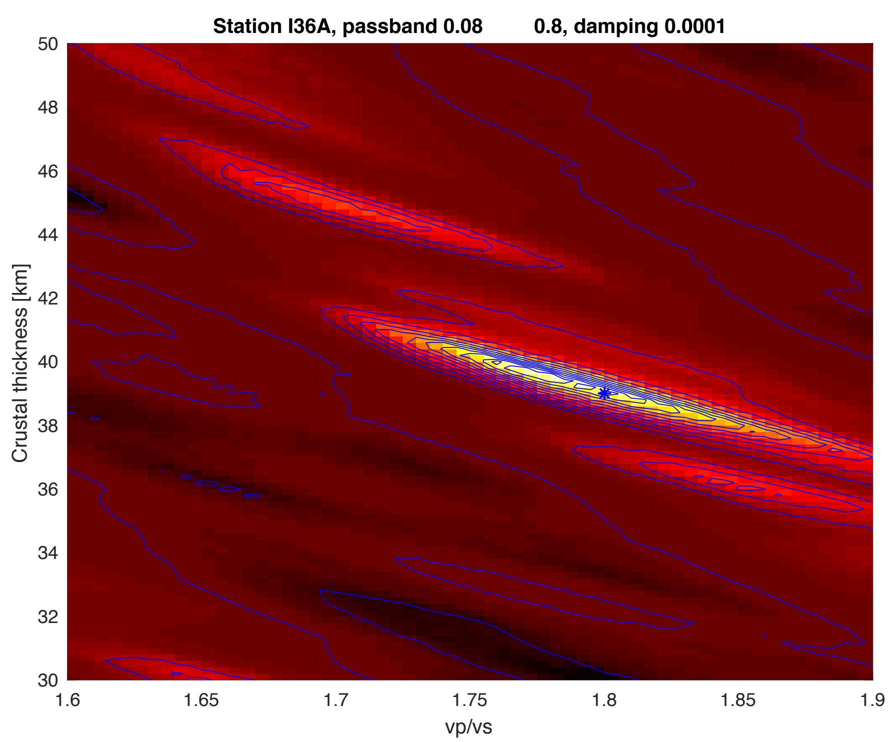

Figure D.20. Result from 4th root H-K stack performed on layer-stripped data from I36A using model TA-2. Areas of lighter color show a higher stacked amplitude. The asterisk indicates highest amplitude. Resulting crustal thickness after correction is 39.6 km.